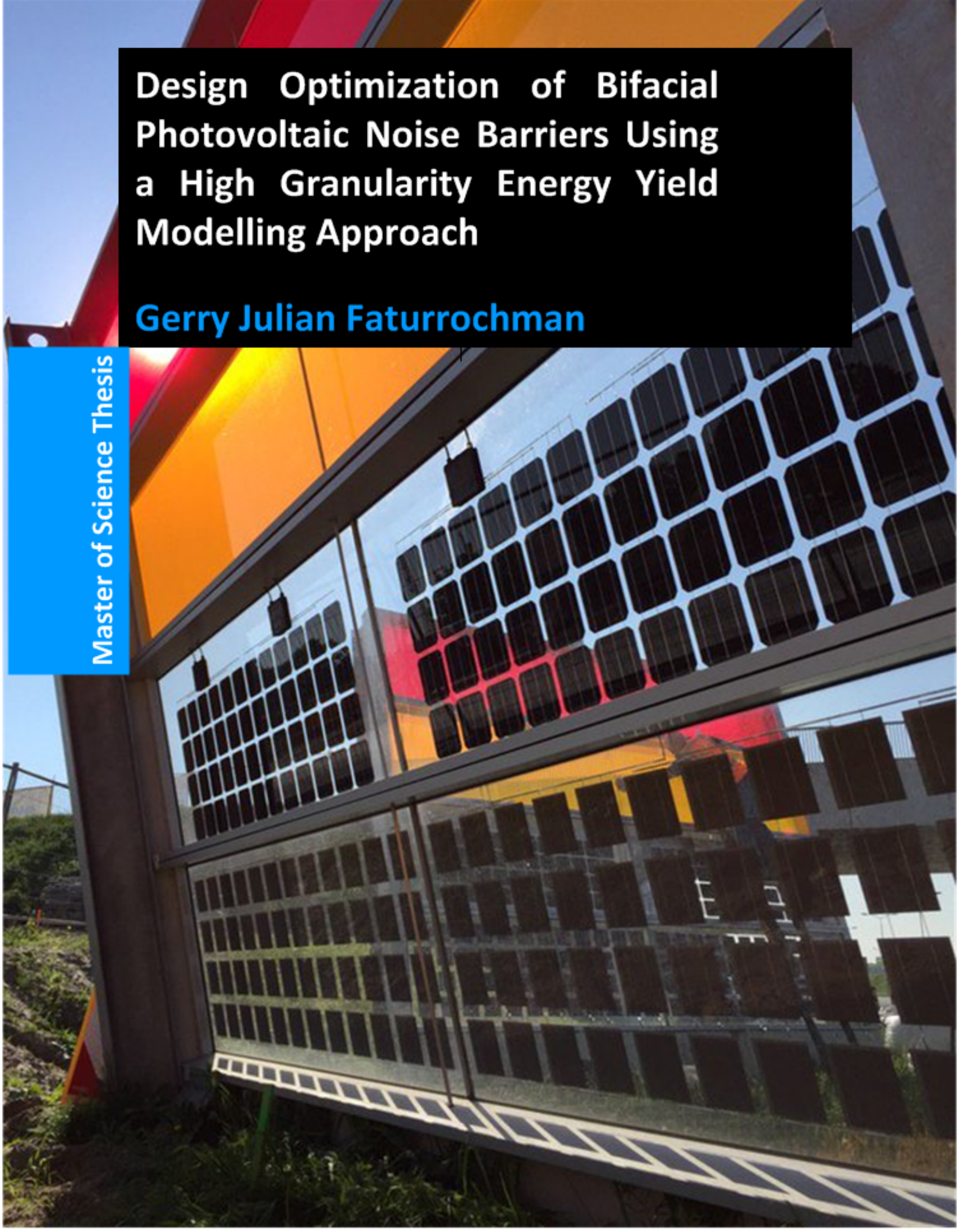

Design Optimization of Bifacial Photovoltaic Noise Barriers Using a High Granularity Energy Yield Modelling Approach

Gerry Julian Faturrochman

Master of Science Thesis

TU Delft Delft University of Technology

seac

Photovoltaic Materials and Device

Design Optimization of Bifacial Photovoltaic Noise Barriers Using a High Granularity Energy Yield Modelling Approach

Gerry Julian Faturrochman

In partial fulfillment of the requirements for the degree of

Master of Science

in Sustainable Energy Technology

July 6, 2017

Supervisor:	Prof. dr. A. A. H. M. Smets (TU Delft)
Daily Supervisor(s):	Dr. M. M. De Jong (SEAC)
	Dr. R. Santbergen (TU Delft)
Readers(s):	Dr. ir. O. Isabella
	Dr. ir. M. Ghaffarian Niasar

Abstract

Integration of bifacial photovoltaic module with a noise barrier (PVNB) has emerged as one of the promising innovation in the building integrated PV (BIPV) system application. By having the advantage to absorb both the light incident from the front and the rear side of the cell, bifacial PV module is suitable for a vertical installation especially when the module is configured to facing west and east direction. However, by nature, PVNB has some limitations that prevent the system to operate in its optimal condition. First, the azimuth of the module cannot be chosen freely, as it has to follow the orientation of the road. Furthermore, the carrying support structures induce an unavoidable self-shading to the rear surface of the bifacial module itself and substantially reduce the power generation of the bifacial PV module.

This project aims to provide a guideline in optimizing bifacial PVNB design to overcome the aforementioned limitations of PVNB application. This study employs a versatile energy yield model that was fully developed in a Python environment. The modeling framework couples a cell-level shading calculation based on vector algebra approach with a high-resolution electrical model that consider bypass diodes configurations in the module. To model the electrical characteristics of bifacial solar cells, two diodes equivalent circuit was modified to have two current sources that represent the contribution of the front and the rear side illuminations. Furthermore, the reliability of the model was proven by the good validation result between the model and long-term experimental data.

The results of this work show that the south-facing bifacial PVNB, in the case of the Netherlands, has the best yield performance when being inclined 15^o from vertical. In contrast, the north oriented bifacial PVNB yield more energy when being installed strictly vertical. Whereas, a consistent performance was shown by the east and west facing module when the tilt angle was varied. Furthermore, the result of the annual energy loss caused by shading is in the range of 1% to 12% for different orientations. Six different bypass diodes layout scenarios were considered in the study. It was demonstrated that the energy yield loss induced by the shading can be mitigated significantly by applying a proper bypass diodes configuration in the module. Another efficient alternative to mitigate the shading that was investigated is by placing the cells away from the structures. Though the analysis focus on one specific PVNB design, the insights derived from this study are generally applicable for any future bifacial PVNB projects.

Acknowledgements

First of all, I would like to express my heartfelt gratitude and sincere appreciation to Dr. Minne de Jong with the opportunity to perform my graduation project in SEAC. I would like to thank Minne for his expert advice and extraordinary support, technically and morally, throughout this project. His positive outlook and continuous enthusiasm for every progress that I have made has inspired me and boost my confidence. It was such an enjoyable experience for me to work under his super-friendly supervision. Also, thanks to Chris and Tom from SEAC who introduced and helped me to adapt with the Python programming in the initial stage of this project.

This thesis would also never be accomplished without the help from all the PVMD group members. First, I wish to convey my gratitude to Professor Arno Smets, for his generous advice and consistent encouragement through the process of this project. This thesis would not have been possible without his valuable input and fruitful discussions in between his busy schedule. My special thank also goes to Dr. Rudi Santbergen, as my university daily supervisor. His extensive and high-quality feedbacks in every aspect of my research helped me to achieve ths result. Every discussion with him have also sharpened my way of thinking to be more systematic and efficient. I am beyond grateful for the time and effort you put into me, thank you Rudi. Furthermore, I would also like to thank all members in PVMD research group for the stimulating feedbacks and discussions.

The life in the Netherlands, both in Delft and in Eindhoven would never be that comfortable without friends around. Thank you for my SET friends, my intern colleagues in SEAC and Solliance for the moments and joy we shared. Special mention to Nga, Tyas, Rithwick, Ebrar, Sundeep, Dito, Sukma, and Wahyu, thank you for being my great companions through all this time. Also, I will not forget to say "Terima kasih" to my all Indonesian fellows who always made me feel like home. "Sukses terus untuk kita semua!"

Finally, I would also take this chance to thank my family, especially to my wife, Irsa, who always there encouraged me in this last two years. I do not have enough words to say my gratitude for her unconditional support to keep me motivated getting through my difficult times. Lastly, for my parents and my brothers, thank you for your support and your prayer during this time.

Delft, June 2017.
Gerry Julian Faturrochman

Contents

List of Figures

List of Tables

CHAPTER 1

Introduction

1.1 Research background

Renewables are a major source of power and our best allies for fighting climate change. Due to the fact that energy and transport contribute to 80% of European Union (EU) emission, the EU leaders has put renewable energy at the heart of its future energy system to overcome the emission problem [1]. Up to this moment, the renewables power over 27% [2] of the EU's electricity production and account for about 15% [3] of the overall energy share.

Solar energy is the source of vast majority of energy on earth. A solar cell converts sunlight directly into electricity which is known as the photovoltaic (PV) effect. In the last recent years photovoltaic technology has emerged to play a substantial role in electricity generation in some countries in the European continent. According to European Commission report, solar PV capacity in EU countries has reached 81.8 GW in 2013 and forecasted to increase steadily by 10% on annual basis [4].

To achieve this ambitious target, it is not enough to solely look at roofs PV application. Therefore, it becomes crucial to find the available land surface area where the huge amount of PV can be installed. Unfortunately, in a densely populated country like the Netherlands, the available space has been already intensively used mostly for residential, agriculture, and industrial purposes. This situation leads to innovate integration of PV into an existing building, which has already occupied space. For instance, by disseminating PV with a noise barrier on motorways [5].

1.1.1 Photovoltaic in Noise Barriers (PVNB)

According to a technical feasibility study of a photovoltaic noise barrier (PVNB) by Nordmann et al. [6], approximately 805 MWp of electricity can be generated by PVNB in six different countries in Europe, including the Netherlands. The study further mentioned that 74% of the potential capacity is dominated by Germany and the Netherlands due to the establishment of a national noise barrier policy in the respective countries.

The first ever PVNB was constructed in 1989 in Switzerland [7]. The capacity of the system was 100 kWp and has been extended for 6 other similar prototypes in Germany and Switzerland in the next 2 years by TNC [7]. In this early period, various configuration concepts from a vertical to a zig-zag configuration were tested. This method is using a building applied photovoltaics (BAPV) concept which directly adds PV Panel on to the noise barrier. This type of application

is represented by pictures shown in figure 1.1.

Figure 1.1: Example of PV installed in highway (BAPV type). (a) solar barrier in Freiburg, Germany (b) solar barrier in Italy (c) solar barrier in Swindon [8].

As time progressed, the application to fully integrate the PV module with the noise barrier structure attracted more attention since it can shorten the construction time, multiple use of the materials, and increase its aesthetic value. Consequently, it forces the photo-active surface to be vertically installed which might not be an optimal position for a conventional monofacial solar cell when facing east or west orientation. Bifacial solar cell is found more suitable for this specific type of installation. Where light incident from both sides, from the front and the rear side, of the cell can be absorbed in the absorber layer.

The world's first fully integrated bifacial PV noise barrier plant on a railway was installed by the end of 2008 in Munsingen, Switzerland [9]. In this project, it was found that the daily output of this vertically installed east-west bifacial module leveled the output performance of a monofacial PV module in optimal orientation. This result is very encouraging and illustrates a good viability of a bifacial PVNB even when installed in unusual orientation.

Figure 1.2: Example of a full noise barrier integration with PV in Switzerland [10].

1.1.2 Solar Noise Barrier (SONOB) living lab

In the Netherlands, integrating solar modules into noise barriers is an interesting option for dual use of space. There are about 1250 km of existing noise barriers and dozens of kilometers are added yearly with a potential area of 5 million m^2 [11]. In 2015, a living lab of Solar Noise Barriers (SONOB) had been installed in Den Bosch by SEAC, ECN, Heijmans, Van Campen industries, Airbus Defence and Space, Scheuten, and other related parties [11]. This living lab was built in order to analyse the performance of different PV technologies. Two different PVNB

(a) (b)

Figure 1.3: Impression of SONOB panel in Den Bosch, The Netherlands. (a) Top view (b) front view [11].

configurations were installed facing west [1] (right barrier) and south (left barrier) as depicted in figure 1.3b. Both PVNB have 15^o backward inclinations from vertical.

Two luminescence solar concentrator (LSC) modules were placed in the top two rows of the module which are represented by the red and yellow panel in figure 1.3. Whereas, the third and fourth row from the top are bifacial and monofacial mono-crystalline silicon PV module respectively. The final result reported by SEAC concludes that the bifacial PV module in both orientation outperforms three other PV technologies. This result confirms the versatility of bifacial PV module to be installed in any tilted and orientation. However, it was found that the bifacial PV module in the noise barrier suffer losses from a so-called self-shading condition caused by the panel-carrying metal structure. This condition will be elaborated in Section 2.3.1

1.2 Motivation of the thesis

In recent years, the integration of solar PV with noise barrier has become an attractive solution in BIPV (building integrated photovoltaics) application. By nature, an integrated PV in the built environment certainly has some limitations that prevent the system from operating in its optimal condition. In this noise barrier integration case, first, the orientation cannot be freely chosen, as it has to follow the orientation of the road. Then to maintain its functionality in reflecting the noise, the panel should be inclined vertically. The existence of the thick structures for this particular construction might also induce a shading problem to the rear side of bifacial module.

This work aims to provide a guideline in designing a bifacial photovoltaics noise barrier system by considering the aforementioned limitations. This includes addressing a general problem with a solution that can be applied for the future PVNB design projects. One way to accomplish this goal is by performing a proper simulation study whose accuracy is supported by good validation with a real experiment data.

Nevertheless, at the moment modeling the bifacial energy yield is not available in commercial software yet. Hence, to develop the yield model of bifacial solar cell is part of the task of this thesis. To begin with, some works that has already been done will be discussed in the next section. This will be followed by the evaluation of the current research as the starting point in the model development.

[1] Front side facing west and rear side facing east. This also the case for south orientation

1.3 Literature review

The purpose of this chapter is to review the literature related to bifacial solar simulation. It begins by presenting a current state of research in this field. It will be followed by evaluation and summary of the current research which can be a valuable input for this thesis.

1.3.1 Existing Research

Model Development

In recent years, the development of bifacial PV model has significantly increased. The complete model generally includes three main sub-models; optical model, thermal model, and electrical model.

Optical model From an optical point of view, the essential part of the model is to estimate the total incident irradiance received by the front side and back side of the module. While the amount of radiation reaching the front side can be similarly estimated like a conventional mono-facial module, the irradiance received by the rear side of the module is much more complex to model because the significant influence of the ground albedo surface and other nearby blocking objects. The unique characteristic of the rear side illumination has been identified in the early stage of bifacial solar cell development. As mentioned in different experimental studies, the higher contribution from rear side illumination was achieved by increasing the height of the bi-facial module from the ground. Up till now, the energy yield gain by installing a bifacial module in higher position from the ground is generally accepted and even become a recommendation by several bifacial module manufacturers in their manual data sheet [12].

A study by Johnson et al. [13] performed irradiance calculation of a bifacial module. In his model, the rear side irradiance is calculated in similar fashion with the front side of the module. The result showed a deviation which was believed to be due to the influence of the shading on the ground nearby the rear side of the module. This effect was confirmed in a study [14] who found a non-uniformity of the irradiance distribution at the rear side of a south facing bifacial module.

The first numerical method to quantify the losses due to the losses of ground reflective irradiance from the ground self-shading is shown in [15]. This paper explained an approach to estimate the reflective irradiance by the used of view factor principle. This phenomena will be elaborated in section 2.3.2. This approach was adopted in several bifacial modeling studies presented in [16, 17, 18]. This view factor concept was also reaffirmed by an experimental validation study in [17] which claimed a good alignment of the model in estimating the non-uniformity of irradiance at the rear side of the bifacial module.

Janssen et al. conducted a vertically installed bifacial performance analysis by comparing the result of field measurement and modeling in MATLAB [16]. For the sake of simplicity, the effects of partial shading caused by surroundings has been taken out from the calculation consideration. The shading on ground reflection approach by Yusufoglu [15] was adopted in this research but only assuming a uniform shading on the rear module side rather than using the cell view factor method.

An alternative method to accurately calculate the non-uniform irradiance distribution is by using a ray-tracing software simulation [17, 19, 20, 21]. Radiance ray-tracing software was deployed to simulate the influence of reflector at the back side of the module in Chin et al

[19]. Whereas, Clifford et al. from Sandia National Laboratories, [17] performed a comparison of two optical modeling methods for back surface of rack-mounted bifacial PV modules: View factor models in Matlab and ray-tracing simulations in two different softwares, Radiance and Comsol. The view factor model was built based on the aforementioned study in [15]. The result from the first validation shows that all three methods followed the trends of the measured irradiance. The error of estimated irradiance was not greater than 5% which is typical for simulation performance model.

Thermal model Thermal model for bifacial PV module is the model component that has been researched least so far. NOCT temperature model [22] is used in various studies [18, 23]. The temperature of the module was calculated by assuming Nominal operating cell temperature (NOCT) formula where 47°C is used for bifacial module instead of the usual 45°C value for the standard module.

Electrical Model Finally, in the electrical model, the standard tools for monofacial PV cannot be used to predict the yield of bifacial PV modules. It was shown by a research done in [24] which has tried to combine two monofacial modules back-to-back as a bifacial module representation in the calculation. The simulation result showed the huge difference between the model and actual measured data for about 35%. Technically, a bifacial solar cell is able to generate current from both sides illumination. Hence, an equivalent circuit representation of monofacial solar cell can be modified to have another current source in parallel to represent the rear cell. The theory behind this relation will be explained further in section 2.1.2.

Singh et al. developed an electrical model of bifacial PV module by first calculating the fill factor of the PV module at a certain module temperature and total irradiance received by both sides of the panel [25]. It was claimed that the deviation between the model and measured data was about 10%. Another way to model the IV response of the solar cell is by using a physical approach based on two-diodes model. Two-diodes model is claimed to be more accurate than a one-diode model, particularly in low irradiance condition [26]. This model was adopted by most of bifacial PV simulation studies [13, 16, 19, 18, 23].

Janssen et al. conducted a performance analysis of a vertically installed bifacial PV module by comparing the result of field measurement and simulation [16]. The two-diodes model was deployed to approximate the I-V curve of the front and rear side of the module which was eventually used to estimate the DC power generated by the module. In the validation step, the I_{sc} results showed by simulation were close to the measurement which leads to the expected result of efficiency values for front and rear side compared to the measurement. Chin et al. conducted a study of an integrated simulation tool for estimating the energy yield of the bifacial solar panel with a reflector on a specific site [19]. PC1D software [27] was used to predict the yield based on irradiance received by both sides.

On top of that, an accurate module IV characterization is required to assure a reliable input for either one-diode or two-diodes electrical model and hence a good prediction of energy yield can be achieved. However, the standard procedure to perform a characterization of bifacial PV module is not yet established. A common way to measure the characteristic of bifacial PV is by covering the backside of the panel with a black sheet, measuring the electrical parameters when illuminating the front side, then doing the same for the other side as shown in [25, 28]. By doing this separate measurement, two IV curves for respective front and rear side of the module can be produced. Another method to measure the characteristic of bifacial solar cell by simultaneous front and rear illumination was introduced in [29]. Front side is flashed by 1 sun while the rear side is flashed 25-30% of the front side illumination. However, it is stated that it would be difficult to carry out this study for STC measurement of a bifacial cell.

Yield optimization of bifacial module

Few simulation and experimental studies that have been described earlier generate simulation results that can be used to optimize the energy yield of bifacial PV modules. Several methods to enhance the performance of bifacial module and the conclusions issued from these various studies are presented below.

Kreinen et al. conducted simulation and experimental study in a rooftop bifacial PV system in Jerusalem [14]. It shows that the irradiance uniformity is improved by increasing the height of the module. Moreover, for this particular roof configuration, it is found that the energy yield gain by increasing the elevation relative to the ground is higher during summer than winter time. This is due to higher direct sunlight hitting the ground in the summer and therefore reflected back to rear side of the module. While during winter the diffused sunlight is dominant, so the shading on the ground is less important.

A study by Yusufoglu et al. focuses on finding an optimum configuration of south facing bifacial PV module by assigning several reflective materials that have different albedo in certain areas behind the module [23]. Two different locations, and albedo values were used to obtain the best bifacial module configuration which can yield the highest annual energy. The result of this simulation study is depicted in figure 1.4. An interesting result was obtained from the simulation which showed that the optimum tilt angle is higher for a lower PV module elevation compared to the module that is installed in higher position.The yield improvement is due to the reduction of the self-shading on the ground.

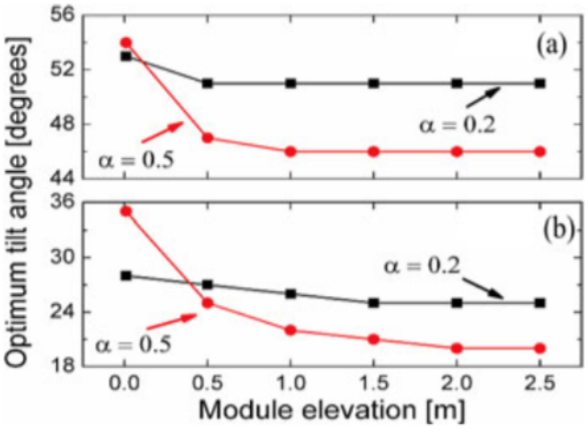

Figure 1.4: Optimum tilt angle of south facing bifacial PV module in Oslo (a) and Cairo (b) by [23]. Note that higher tilt angle in Oslo is preferable.

Influence of albedo on bifacial module yield study was studied by Jansen et al. The model that was initially created is used to predict the annual yield of the bifacial module in two different locations and different ground albedo value [16]. As expected, the result shows that the AEY (Annual Energy Yield) increases strongly with albedo. With a 10% gain at 0.2 and 30% at albedo 0.5.

Another solution to increase the bifacial PV yield by obtaining the most optimal cell placement distance in the module was proposed in [19]. In this experiment, a mirror is installed on the ground behind the module. By gradually increase the distance between the cells, the highest reflective irradiance can be achieved. This is due to the amount of the reflected irradiance from the mirror that comes through the glass between cells. It was found by the placing the cells in optimum spacing and distance to the mirror on the ground, the system can produce 26% higher yield compared to the experiment design.

1.3.2 Literature gap

Research up to this stage indicate that there are on-going development of the electrical, optical, and thermal model to estimate energy yield of bifacial PV module being carried out by many institutions. From an optical model point of view, most of the studies focused on modeling the derating of reflected irradiance caused by the ground shade effect. None of the studies accounted the partial shading condition in the model. The NOCT thermal model were widely used by most researchers. This NOCT model, however, was less accurate because the wind influence is not incorporated in the model. Although the two diodes model has been used in several studies, a detailed model that consider bypass diode configuration in the module is barely considered.

Various optimizations to enhance the energy yield from bifacial PV modules also have been investigated by some studies, both through simulation and real field experiments. It was observed that tilt angle, module orientation, module distance from the ground, and the use of reflector material on the back side are some variables that can influence bifacial module performance. However, most of the works and simulations only focused on the tilt module optimization for south-facing bifacial module by investigating the influence of shading on the ground [17, 23, 18]. Based on these thorough investigations, how sensitive the tilt angle is in affecting yield performance of bifacial PV module in different orientations is one of the questions that current research has yet to reveal.

Furthermore, most of the work found on bifacial PV system modeling used a typical commercial solar panel design configuration. A specific issue that occurred in bifacial PV integration in the built environment has not been addressed yet. In the case of fully integrated bifacial PVNB, the rear surface of the bifacial module is vulnerable to shading losses caused by the embedded structure as reported in [11]. Consequently, another particular concern in this thesis is to quantify the shading losses and analyze the potential performance improvement by implementing different shading mitigation strategies. One way to do this is by improving the inter-module circuitry that includes the bypass diode interconnection in the module.

1.4 Objectives and research questions

Based on the motivations (section 1.2) and the literature gap (section 1.3.2), there are two research objectives in this thesis. The first objective is to develop a detailed energy yield model of bifacial solar cell that has ability to simulate the electrical performance under inhomogeneous irradiance condition. This model is used to help in addressing the second objective in this thesis; to study the yield performance of bifacial PV module under various parameters when being fully integrated in noise barrier system. Self-shading problem, that was found as one of the factor that limits the yield performance, is one of particular problem that will be addressed in this study. This leads to the main research question of this thesis as follows:

"How do bifacial PV modules perform when they are being integrated with noise barrier systems?"

The following sub-questions will be answered to assist in answering the central question:

1. What are the electrical characteristics of the photovoltaic noise barriers in the case of the Netherlands?
    - Which inclination provides the best performance in terms of energy yield for different PVNB orientations?

- How big is the shading loss caused by the noise barriers structures on affecting the yield performance of PVNB?
- What is the effect of increasing the bifacial module height relative to the ground on the yield performance of PVNB?

2. What are the possible improvements in PV module and system architecture design to enhance the annual energy yield?
   - How effective are the different bypass diode configurations in the module in mitigating a partial shading condition?
   - How does a different cell positioning affect the DC yield performance?
3. What is the yield performance of bifacial PVNB in different geographical locations compared to the Netherlands?

1.5 Thesis Outline

Chapter 2 starts by the explanation of some theoretical background of bifacial solar cell and its integration in noise barriers, as the complexity of the bifacial solar cell output requires greater understanding. Next, the development and validation of three main sub-models : (i) optical, (ii) thermal, and (iii) electrical are explained separately. Chapter 3 outlines the methodology of irradiance calculation on both side of bifacial PV module including the shading model used in this work. Chapter 4 explains the developed thermal model based on the energy balance of the system. Chapter 5 introduces the proposed concept of yield calculation based on physical approach. Afterwards, the developed models are used to perform simulation study of PVNB performance under different scenarios. The results of the study are presented in chapter 6. Finally, chapter 7 concludes this thesis by summarizing model development and results obtained in chapter 6. It is followed by outlining future research directions and recommendations. The work flow of each step in this thesis is illustrated by the flowchart in figure 1.5.

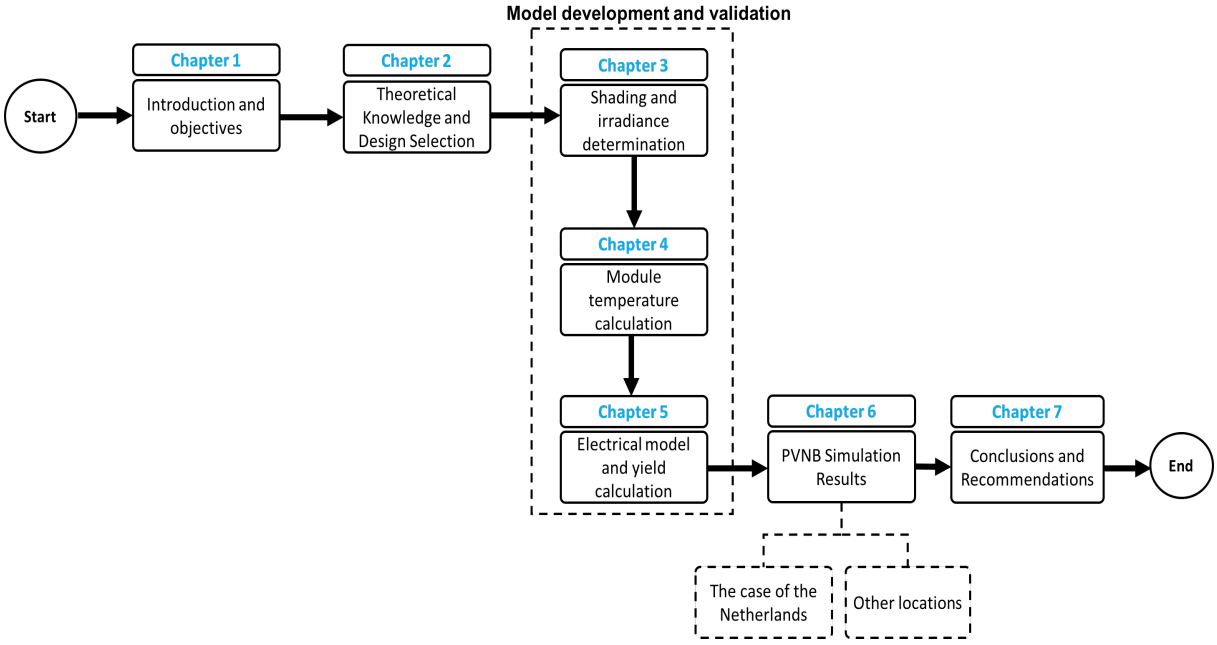

Figure 1.5: Outlines of the reports.

CHAPTER 2

Bifacial solar cell in the built environment

In this chapter, the theoretical backgrounds affiliated to bifacial solar cells and photovoltaic noise barriers are explained. The information in the following sub-chapters is required to provide a know-how in addressing several issues of this thesis topic. First, a brief physical theory of bifacial solar cells and its difference with the standard monofacial solar cell along with the concept of electrical characterization of bifacial solar cell are presented in section 2.1. Next, section 2.2 describes the underlying guidelines for photovoltaic noise barrier design selection used for simulation study in chapter 6. Lastly, section 2.3 elaborates the parameters and its impact on the irradiance distribution in bifacial PVNB.

2.1 Bifacial solar cells

The early evolution of bifacial solar cell was firstly introduced by a Japanese researcher H. Mori in 1960 [30] as a novel concept for enhancing the energy output of PV system. Principally, a bifacial technology is a continuation of a standard monofacial module by replacing the fully back metallic contact with a selective area contact, which is commonly very similar with the front side metalization, to allow additional illumination through the rear side of the module. It is possible to manufacture bifacial cells out of p-type and n-type silicon wafers. However, in this project, n-type monocrystalline silicon (mc-si) bifacial cell technology is selected for the modeling work and therefore will be explained in the following section.

2.1.1 Cell Structure

As previously mentioned, the standard monofacial solar cell fundamentally consists of a thin silicon wafer having a PN junction that can only utilized the light that coming from front side of the solar cell. Bifacial solar cell, however, is not having the rear contact over the entire rear side, consequently the cell will have two photo-active sides which can allow simultaneous illumination on both surfaces of the cell. The enhancement of electrical power generation can be observed due to the utilization of rear side in absorbing the light. The cell cross section comparison between the standard monofacial solar cell and bifacial solar cell are illustrated in figure 2.1.

Figure 2.1 shows that the absence of a full rear contact in the bifacial solar cells is the main physical difference compared to the standard monofacial one. Moreover, the anti-reflection coating (ARC) layer is added to reduce the light reflection on the outer surface. Whereas, the structure of front side remains the same compared to the standard monofacial solar cell.

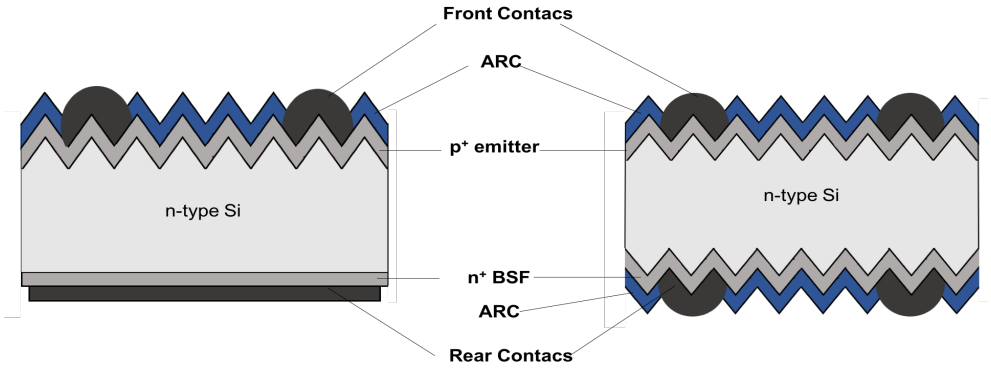

Figure 2.1: Comparison of monofacial vs bifacial cell structure from cross-section view. This represents a n-type silicon technology.

2.1.2 Electrical circuit equivalent bifacial solar cell

This section explains a fundamental theory of electrical characteristic in bifacial solar cells that contains valuable information in electrical model development. To illustrate the electronic behavior of a solar cell, an equivalent circuit which comprises of several electronic components such as diode and resistor can be used.

The first method to model the I-V characteristic of a solar cell is a simple single-diode model which assumes the absence of recombination loss in the depletion region. This single-diode model can be represented by a single current source with a diode connected in parallel. Whereas, two resistors connected in series and parallel represents the series resistant and shunt resistant respectively. Compared with the single-diode model, the two-diode model offers better accuracy in solar characterization, particularly in maximum power point region of Si- solar cells as validated and shown in [26, 31, 32, 33].

In recent research of bifacial solar cell characterization, the total photo current I_{ph} under bifacial illumination is found to be equal to the addition of both currents generated by the front side and rear side solar cell [14, 25, 29, 34]. It is based on the assumption of the linear superposition of the front side short circuit current ($I_{ph,f}$) and rear side short circuit current ($I_{ph,r}$) and assumes nothing else changes. This condition has been confirmed and validated with outdoor experiment by NREL [20].

Based on the aforementioned assumption, the two-diode model for a standard monofacial solar cell can be modified into an electrical circuit that has two parallel current sources as can be illustrated in figure 2.2. The additional current source represents the current generated by the rear side illumination ($I_{ph,r}$).

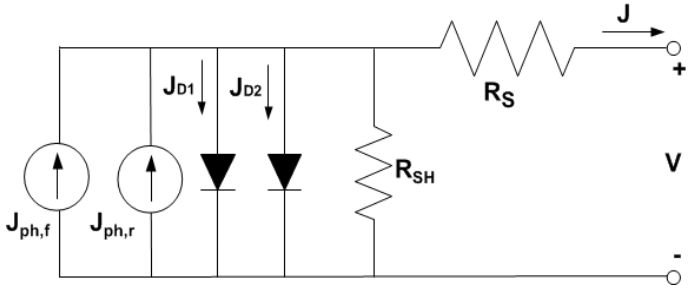

Figure 2.2: Two-diodes equivalent circuit of bifacial solar cell.

By looking at equation 2.1, the total output current(I) then can be solved mathematically with expression in equation 2.1. Where $I_{ph,f}$ and $I_{ph,r}$ represents the light generated current from front and rear illumination respectively. I_{D1} and I_{D2} are the representative current flowing through two diodes in the circuit and the equivalent series and parallel resistances are denoted as R_s and R_{sh} respectively.

$$I = I_{ph,f} + I_{ph,r} - I_{D1} - I_{D2} - \left(\frac{V + IR_s}{R_{sh}}\right) \tag{2.1}$$

Bifaciality factor

In most cases, the front side of bifacial solar cell always determined by the side that has better electrical parameters compared to the other side which then defines as the rear side (normally by comparing the efficiency values). The parameters are obtained from independent measurement of front and rear side IV curve under standard test condition (STC). The reason of smaller efficiency of the rear side of bifacial cell is caused by the longer distance of generated electron pairs to travel to the p-n junction at the front side. Consequently, this condition increases the probability of recombination and the efficiency slightly decreases. This explains why the front side illumination gives higher efficiency compared to rear side illumination.

A term to show the rating ratio between the front side and rear side of bifacial solar cells is widely known as "bifaciality factor" (f_B). The concept was first introduced in [29] who investigated this relation by varying a light intensity to rear side of bifacial module while the light intensity on front side was kept in one sun condition. The bifaciality factor (f_B) can be defined as the ratio between the rear ($I_{sc,rear}$) and the front short-circuit current ($I_{sc,front}$) measured at STC which is given in the equation 2.2. Where a typical bifaciality factor of bifacial module in the market has values between 85% - 95% [12].

$$f_B = \frac{I_{sc,rear}}{I_{sc,front}} \tag{2.2}$$

Recalling the current linearity contribution that was previously mentioned, the bifaciality factor became an important parameter to scale the photo generated current of the rear side $J_{ph,r}$ of the bifacial solar cell under simultaneous front and rear illumination. It can be used to weight the contribution from rear junction to total output current by their absorption fraction. This approach will be used to unravel the two-diodes model in equation 2.1. A full solution and explanation will be fully treated in chapter 5.

2.2 Selection of Photovoltaic Noise Barrier Design

This section describes the fundamental design of the PV module and its noise barrier integration component used for simulation study in chapter 6. Generally speaking, a noise barrier has a main function to prevent noise pollution from a motorway or railway reaching civilian habitants. It is constructed from a tall solid material with sufficient supporting structures to overcome the mechanical load from the wind and weight of the barrier itself. However, the interpretation to design this barrier can be normative and yield too many different designs in practical condition.

To overcome this situation, in 2006, Rijkswaterstaat (RWS)[1] published a standard design of a sound barrier in the Netherlands. This type is named as modular noise barrier or in Dutch

[1]part of the Dutch Ministry who is responsible for the design, construction, management and maintenance of the main infrastructure facilities in the Netherlands

as *modulaire geluidsschermen* (MGS). This guideline provides various sound barrier templates with a wide range of height, inclination, and absorber material selections [35]. According to the establishment of the standard, the design of PVNB used in this thesis is following the said MGS design. The overall design follows the PVNB design in SONOB project, that has four glass barrier sections in one barrier. Each section has two bifacial modules, left and right. Thus, there are eight bifacial modules in one barrier as depicted in figure 2.3a.

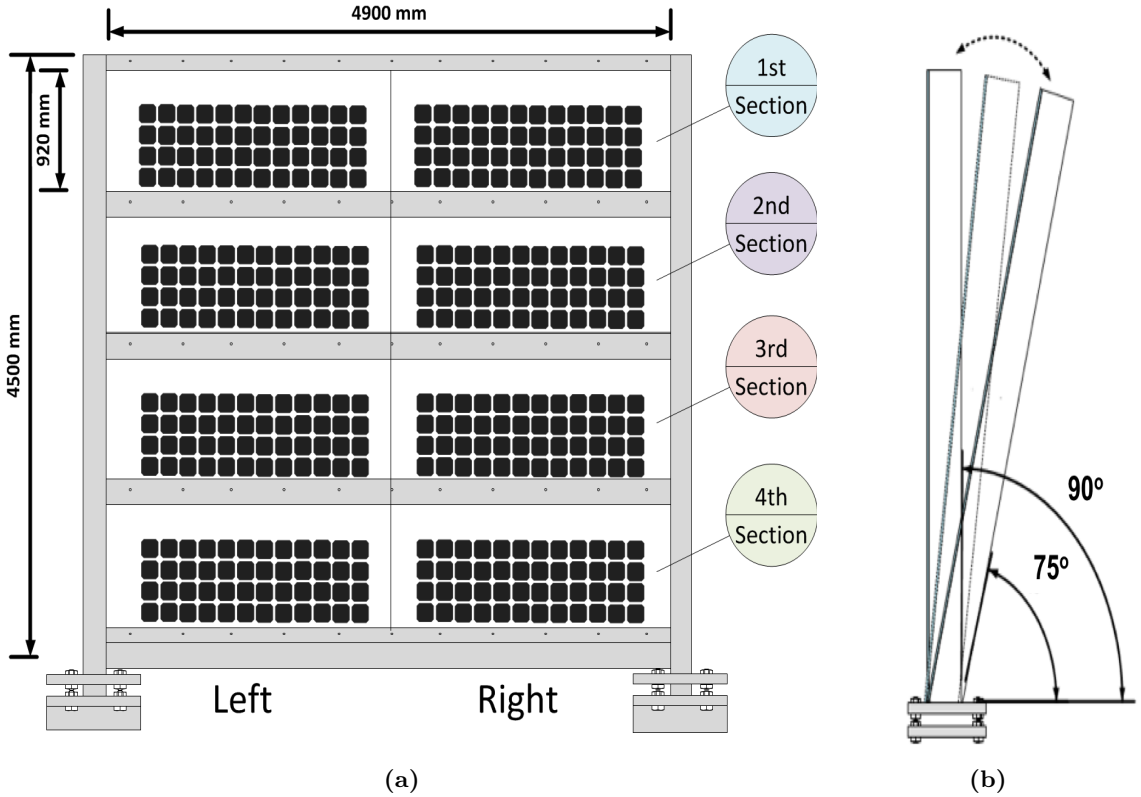

Figure 2.3: Design of PVNB defined as a study case in this study (a) front section of the PVNB. 8 modules are distributed evenly in 2 columns x 4 rows (b) View from the side of the barrier. 75° is set as the reference inclination with possibility to set the barrier exactly vertical.

Some of the technical background to support the selection of noise barrier design in figure 2.3b can be pointed out as follows:

Dimension Insertion loss is a term used to represent the difference between the sound level at a receiver point without the barrier and the receiver point with the barrier. According to Federal Highway Association [36], 10-15 dB is a desirable number of overall insertion loss considered in noise barrier design. In compliance with this target, a certain height of a noise barrier can be determine based on the study from May et al [37]. From the same document it was found that a 4.5 m as presented in SONOB panel scheme is allowed to achieve 10 dB insertion loss. This noise reduction is complied to the Dutch regulation mentioned in [35, 38]. The detail dimension information is given in figure 2.3a.

Tilt Angle A noise barrier can be installed vertically or slightly tilted. Practically, an inclined wall is a good solution to improve the noise reduction by reflecting the sound away from the receiver. According to Slutsky and Bertoni 3° is the optimum angle to overcome the effect of multiple reflections of the sound from a parallel installed noise barrier[38]. However, according to MGS standard, the barrier is still allowed to have maximum 15° backward inclination [35] (see figure 2.3b).

Glass panel section Tempered glasses are considered for this noise barrier system due to the needs of aesthetics and safety at the same time. A certain glass thickness is needed to enable the sound absorption functionality. Also, the glass structure is required to allow the illumination of the rear side of the module. The whole panel then is divided into four sections of glass. Where each section consists of two bifacial modules (see figure 2.3a).

PV modules The bifacial PV module used in this work comprises of 48 n-type monocrystalline silicon bifacial silicon solar cell connected in series. By having the validation of IV curve in place (will be explained in section 5.2.2), the same bifacial solar module used in SONOB project is selected to maintain the level of modeling accuracy. Solar cell with 156 mm x 156 mm square area can be freely distributed in the entire glass section. Lastly, the reference spacing between the cell is assigned to be 16 mm for the most of simulation study except in design optimization part in section 6.3. In section 6.3, various combinations of the module distance from the side structure and cell spacing are observed to see the effectiveness in avoiding the self-shading condition.

2.3 Parameters affecting the incident irradiance of bifacial PVNB

The estimation of the amount of irradiance that falls on the front surface of bifacial solar cell is very similar to the calculation of incident irradiance on the monofacial module. On the other hand, the irradiance distribution on the rear surface of bifacial solar cell is more complex to model. It is even more difficult to predict when being integrated with such noise barrier structure. Two main phenomena that mainly influence the irradiance on the rear side are:

- Self-shading due to noise barrier structure
- Ground reflected irradiance reduction

These two phenomena will be explained in the following sub-sections.

2.3.1 Self-shading

Self-shading is a term used to illustrate the condition when the metal structures of noise barriers, in which the bifacial PV module is installed, cast a shadow to the rear side of the surface. Such condition is particularly found in the east-west facing PVNB panel in SONOB living lab test as reported in [11]. The illustration of the partial shading condition on the panel above is depicted in figure 2.4.

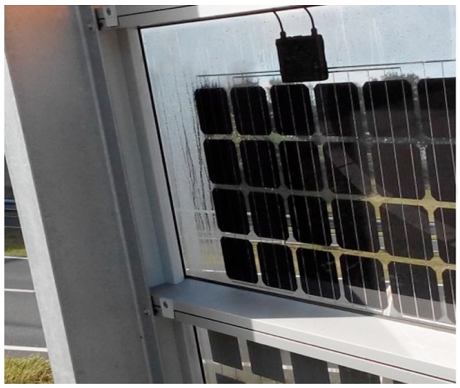

Figure 2.4: Rear surface (facing east) of bifacial panel affected by the shadow casted by the side structure in the morning. The picture is taken on a sunny day 30th June 2015. [11]

It was reported by de Jong et al. that the electrical output of the bifacial solar module installed in SONOB test field was heavily suffered from the self-shading in the morning on June 30th, 2015 [11]. The effect of this self-shading is presented in figure 2.5. Where blue scatter dots indicate the non-linearity of power output in the morning. Furthermore, this effect is also observed in terms of annual average performance ratio (PR)[2] for east-west[3] facing barrier during the morning and the afternoon were in the average of 72.9% and 86.3% respectively. [11].

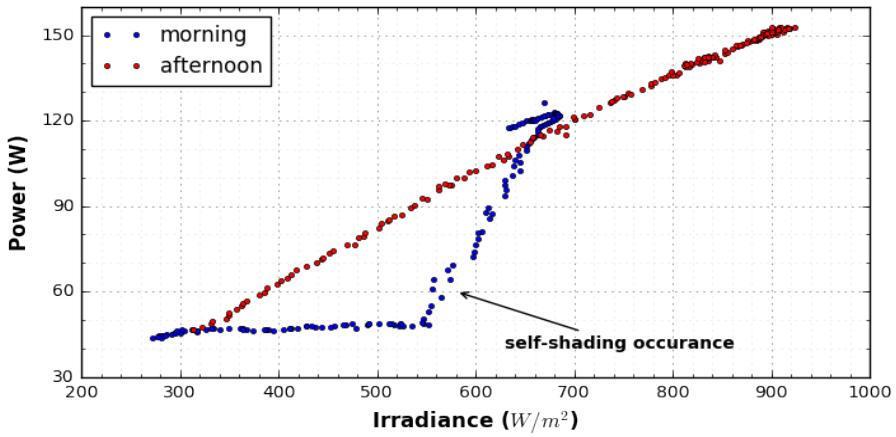

Figure 2.5: Scatter plot of power measurement against irradiance measurement on a sunny day. The shading impact can be easily observed from the non-linearity relation between power and irradiance. Data is adapted from [11].

2.3.2 Influence of ground shadow

Besides partial shade caused by the embedded structure, the shadow on the ground casted by the solar panel is an extra parameter that affects the non-uniformity of irradiance distribution at rear side of bifacial solar cell. The presence of the panel blocks some amounts of the irradiance reaching the ground which has potential to be reflected back into the rear surface of the module. This phenomenon was initially found by Kreinen et al [14] who performed an experiment on analyzing irradiance distribution of south facing bifacial solar cell. Later, this condition is also confirmed by experiments and simulation studies mentioned in [17, 23, 39, 25, 18, 21]. The illustration of the shadow on the ground is depicted in 2.6. Note the different area of shaded ground due to the difference of module configuration in both figures.

The inhomogeneity of irradiance distribution by shaded ground effect is rather difficult to calculate since the influence of the shadow depends on the distance of the surface from the shaded ground. This condition can be explained by using the view factor (VF) concept from fundamental radiative heat transfer term as firstly introduced by Yusufoglu [40]. At the moment, this concept has been widely used in bifacial solar cell optical simulation which has been documented and standardized in PV Performance modeling collaborative website by Sandia National Laboratories [41].

View Factor (VF)

Borrowing the radiative heat transfer terms, a view factor ($VF_{i\rightarrow j}$) defines a proportion radiation leaving one surface (i) that strikes another surface (j). In the context of bifacial PV module, the surface i accounts for the shaded ground and surface j represents the rear side of bifacial PV module. View factor value can be numerically calculated by double surface integration as expressed below [42].

[2] PR is defined as the ratio of measured power and rated power of the module

[3] Front side facing east, and rear side facing west.

(a) (b)

Figure 2.6: Ground shade condition in real experiment (a) a south facing and tilted module installation by Franhoufer [21] (b) and east-west vertical installation [13]. Note that he shaded ground area is larger in a tilted module (figure a).

$$VF_{i\to j} = \frac{1}{A_i}\int_{A_i}\int_{A_j}\frac{\cos\theta_i \cdot \cos\theta_j}{\pi \cdot r^2} dA_i dA_j \tag{2.3}$$

The graphical illustration of the fundamental view factor in equation 2.3 is shown in figure 2.7. As can be seen in figure 2.7, r is a length of a vector which connecting the center of differential area i (dA_i) area j (dA_j). In other words, it represents the distance between dAi and dAj. Where, θ_i and θ_j are the angle between vector r and the normal vector of surface dAi and dAj respectively.

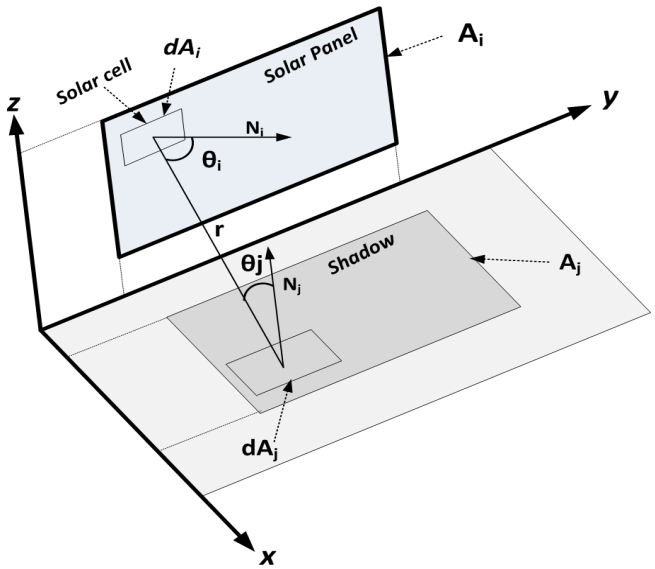

Figure 2.7: View factor approach. Surface i and j represent the cross section of shadow on the solar panel and shaded ground respectively.

Since the distance of the ground from each cell is different, every cell will receive unequal reflected irradiance. Therefore, view factor of each cell to the ground has to be calculated in cell level to be able to capture the mismatch of irradiance distribution on the rear surface. This cell level view factor is implemented in this model and will be elaborated further in section 3.2.3.

CHAPTER 3

Modelling Irradiance on bifacial PV module

The aim of this chapter is to develop a comprehensive and flexible irradiance model of the front and rear side bifacial PV module. According to the insight from section 2.3, the model should be able to calculate the complex irradiance distribution on the rear side of the bifacial PVNB in which affected by the partial shading caused by the structure. The reflected irradiance reaching the rear surface due to the shaded ground has to be incorporated as well. To correctly capture electrical mismatch conditions, a high-resolution model that accounts partial shade condition in cell level is deployed in this work.

Section 3.1 starts with the description of meteorological data and the fundamental of solar position algorithm used in this simulation. The numerical approach of solar irradiance and shading calculation model is extensively elaborated in section 3.2. An alternative ray tracing approach, that eventually utilized as comparison tool, is briefly explained in section 3.3. Finally, the verification of the numerical model with other tools and outdoor experiment is reported in 3.4

3.1 Meteorological Data and Sun Position

Meteorological Data

The meteorological database from Meteonorm 7.0 [43] is utilized as the main source of the weather data input of the model simulation. The data provided by this software is based on the historical data and hence suitable to represent a typical meteorological yearly (TMY) data for any given location in the world. This includes the irradiance data, wind speed, and ambient temperature data in minutely resolution[1]. These data are used throughout this thesis in modeling explanation and simulation part.

Sun Position Algorithm

The incident power received by the surface of the PV module does not only depend on the available irradiance but also from the position of the sun. The sun position will determine the angle incident of the module which can be used for direct normal irradiance transposition factor. Moreover, it is also an essential condition for determining shading projection from surrounding object. Principally, altitude angle (θ_{alti}) and azimuth angle (θ_{azi}) are two variables that used to indicate the position of the sun in the sky as illustrated in figure 3.1. In this work, Yallop algorithm is used to calculate the azimuth and altitude pair of the sun position in the sky [44].

[1] Minutely data are generated from hourly historical data based on TAG minute model that have been validated by the software creator.

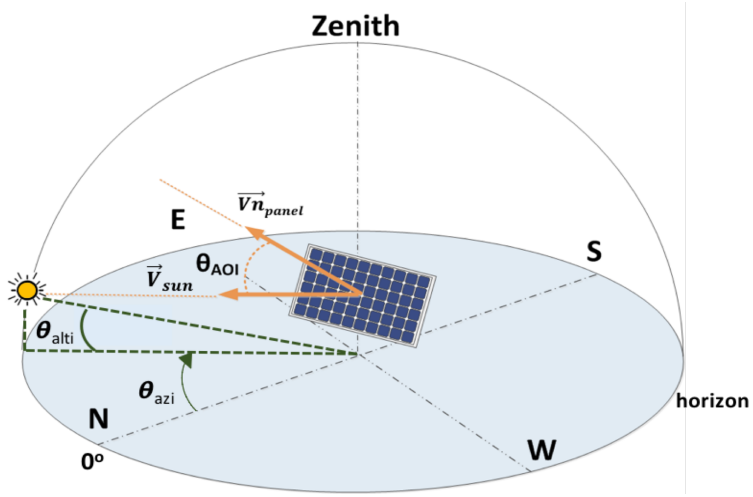

Figure 3.1: Illustration of the Sun position in the sky dome and angle of incidence (AOI) between the Sun and PV Module.

Sun altitude and sun azimuth can be used to determine the vector pointing the sun ($\vec{V}_{sun}$) that can be calculated by using equation 3.1. It should be pointed out that the calculation of incident angle (θ_{AOI}) is also based on vector calculation. Where $\cos\theta_{AOI}$ can be found as a dot product between sun vector and normal vector of the module as expressed in equation 3.2.

$$\vec{V}_{sun} = \begin{bmatrix} S_x \\ S_y \\ S_z \end{bmatrix} = \begin{bmatrix} -\sin(\theta_{azi}) \cdot \cos(\theta_{alti}) \\ -\cos(\theta_{azi}) \cdot \cos(\theta_{alti}) \\ -\sin(\theta_{alti}) \end{bmatrix} \tag{3.1}$$

$$\cos\theta_{AOI} = -\vec{V}_{sun} \bullet \vec{V}n_{panel} \tag{3.2}$$

An illustration of an annual the Sun path or widely known as the Sun analemma is presented in figure 3.2. This figure provides the information of the sun position during summer and winter solstice (top line and bottom line respectively) and the equinox time (turquoise line in the middle) which is very important for irradiance and shading analysis.

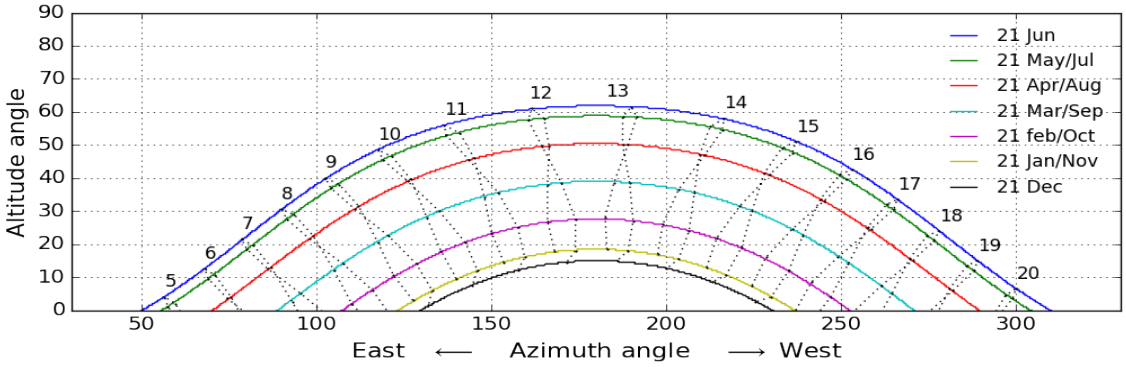

Figure 3.2: Sun position throughout the year of Den Bosch in the function of azimuth and altitude. The number above analemma line (black dotted line) represents the corresponding hour of the sun position.

3.2 Numerical geometry model

The combination of 3D parametric design to calculate shading and incident irradiance calculation is deployed as the backbone of the developed numerical model. First, the overall terms in determining the global incident irradiance and its component is explained in section 3.2.1, followed by the elaboration of shading calculation in section 3.2.2. Finally, section 3.2.3 describes the implementation of view factor approach to calculate the ground shade on reflected irradiance calculation. It should be emphasized that irradiance distribution for the front and rear side is calculated separately in cell-level resolution.

3.2.1 Global Incident Irradiance

Total solar irradiation received by an inclined PV surface is determined by the sum of direct component G_{dir}, diffuse irradiance G_{dir}, and ground diffuse or reflected irradiance G_{ref}. In the case of the bifacial module, the same procedure is applied individually for the front ($G_{tot\,f}$) and rear side ($G_{tot\,r}$).

$$G_{tot\,(f,r)} = G_{dir\,(f,r)} + G_{dif\,(f,r)} + G_{ref\,(f,r)} \tag{3.3}$$

Direct Irradiance

The direct component on a tilted panel can be calculated by correcting the direct normal component (DNI) with the angle of incidence between the normal panel and solar vector (equation 3.2), the losses due to the Fresnel loss (F_{IAM}), and shading (SF) as expressed in the following equation.

$$G_{dir} = DNI \cdot \cos(\theta_{AOI}) \cdot F_{IAM} \cdot (1 - SF) \tag{3.4}$$

The optical losses due to the effect of reflection and absorption is expressed in terms of the incidence angle modifier F_{IAM}. F_{IAM} at a certain θ_{AOI} can be found as the ratio between the transmittance at a certain incidence angle $\tau(\theta_{AOI})$ and the transmittance when the angle is normal to the sun $\tau(0)$ as expressed in equation 3.5. This is based on a physical approach which combines the Snell′s and Bougher′s law [45].

$$F_{IAM} = \tau(\theta_{AOI})/\tau(0) \tag{3.5}$$

General term of transmittance $\tau(\theta)$ can be calculated using equation using equation 3.6. Where $\theta_r = \sin\theta_{AOI}/n$. n is the refraction index of the glass that is assumed to be 1.56, the glazing coefficient K is 4 m^{-1} [45] and the thickness of the glass (L_g) is 8 mm follows the PVNB design in section 2.2. Figure 3.5 shows the said optical losses calculation as the function of AOI. Note that the loss is higher as the AOI is increased.

$$\tau(\theta) = e^{-KL_g/\cos\theta_r} \cdot \left[1 - 0.5\left(\frac{\sin^2(\theta_r - \theta)}{\sin^2(\theta_r + \theta)} - \frac{\tan^2(\theta_r - \theta)}{\tan^2(\theta_r + \theta)}\right)\right] \tag{3.6}$$

Finally, the shading fraction (SF) refers to area of the cells that is covered by shadow, which is 100% for a fully shaded cell and zero for an unshaded cell. The determination of this component is treated separately in section 3.2.2.

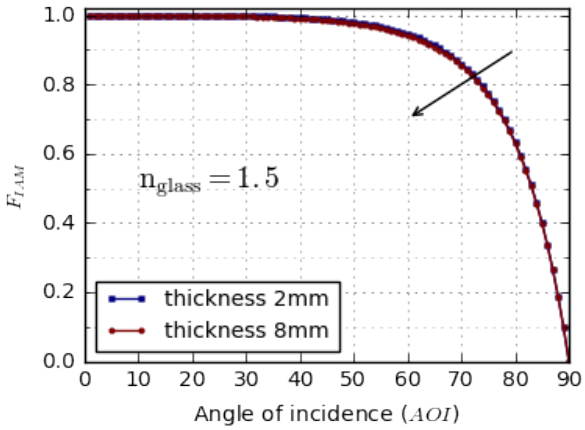

Figure 3.3: Simulated IAM values as a function of AOI. Two different glass thickness are used to represent the losses of commercial solar panel (2 mm) and bifacial module used in this thesis (8 mm). Note that the reflection loss difference between those two different glass thickness is very small.

Diffuse Irradiance

The diffuse component is calculated by the product of diffuse horizontal irradiance (DHI) and the transposition factor (known as sky model). Isotropic sky model, that only accounts the geometry of module, was found to be less accurate than the anisotropic sky model [46][47]. This anisotropic sky model is not solely dependent on the panel configuration, but also accounting the circumsolar and the horizon brightening component in the sky. Here, an empirical approach by Perez [47] is implemented as it was found to perform best among other anisotropic diffuse model[46]. Equation 3.7 shows the diffuse component formula, where the terms after DHI are represented the Perez sky model.

$$G_{dif} = DHI\left[(1 - F_1)SVF + F_1(a/b) + F_2 sin(\theta)\right] \tag{3.7}$$

In equation 3.7, a is referred to $\cos_{AOI}$ while b denotes cosine of the sun zenith (cos_{θ_z}). $F1$ and $F2$ are fitted functions of the circumsolar and horizon brightness respectively, that represent the sky condition and can be determined as follows.

$$F_1 = max\left[0, f_{11} + f_{12}\Delta + \frac{\pi\theta_z}{180^o} f_{13}\right] \;\&\; F_2 = f_{21} + f_{22}\Delta + \frac{\pi\theta_z}{180^o} f_{13} \tag{3.8}$$

Where $f1n$ and $f2n$ are the empirical coefficients that are obtained from the specific bin based on the clearness index condition (kt) [47].

Finally, the SVF (sky view factor) denotes as the ratio of a proportion of the sky seen by the panel plane and the whole sky dome that has value ranging from 0 to 1. This factor is constant over the time and only need to be determined once. For an ordinary PV panel module this SVF can be calculated as the function of the tilt module (θ_m) $SVF = \frac{1+\cos(\theta_m)}{2}$. However, specifically for the rear surface of bifacial solar panel in PVNB, the metal structures are became additional obstructions for the cell to see the sky. To be more precise, the SVF can be calculated by creating hemisphere and cast rays from each mesh in the hemisphere. Finally, SVF can be obtained by the ratio of the integral of the ray that intersects obstructions and the surface module to the total surface of the hemisphere. Figure 3.4 shows the illustration of the specific SVF calculated for bifacial PVNB in this thesis.

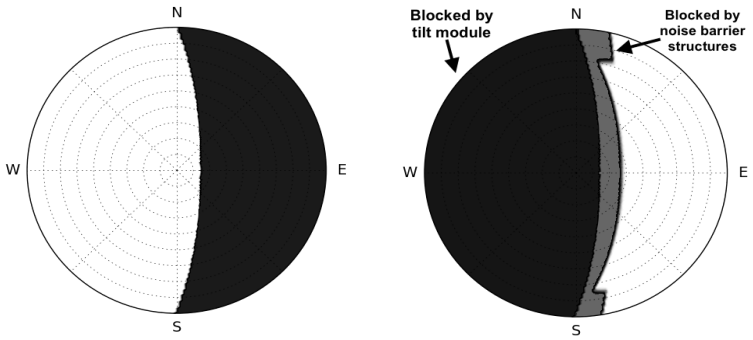

(a) Front side **(b)** Rear side

Figure 3.4: Sky view factor of a west-facing bifacial PV module that 15^o inclined backwards from vertical in noise barrier. (a) Front side and (b) rear side. The effect of additional obstructions on the rear side is visualized by a brighter color area in figure (b). Sky view factor is simply represented by the white area in the polar plot.

Reflected Irradiance

Reflected irradiance is the amount of global irradiance that reflected back toward the module surface. For the front side, the reflected irradiance component can be calculated using equation 3.9. Where α is an albedo value of the ground surface that has value between 0 and 1. In this work, 0.2 albedo value was selected (unless stated otherwise) as fairly represents the average value between asphalt and grass [48].

$$G_{ref\,front} = \alpha \cdot GHI \cdot (1 - SVF) \tag{3.9}$$

For the rear surface of bifacial module, it was explained in section 2.3.2 that the amount of ground reflected irradiance received by this surface is influenced by the shadow on the ground. This approach assumes that only the direct irradiance is reduced by the proportion of the view factor of the cell into the shadow on the ground. Whereas, the diffuse component is not affected by the shadow[2]. By applying this condition to equation 3.9, the amount of reflected irradiance on rear surface can be calculated using equation 3.10.

$$G_{ref\,rear} = \alpha \cdot GHI \cdot VF_{cell \rightarrow non-shaded\,ground} + \alpha \cdot DHI \cdot VF_{cell \rightarrow shaded\,ground} \tag{3.10}$$

3.2.2 Shading model : Vector algebra approach

Partial shade condition caused by object surroundings leads to reduction of the amount of irradiance reaching the solar panel. Several tools such as Horicatcher (fish eye camera) or shadow plugin in Sketch Up are able to capture the shading condition through the day and year [49]. However, these tools have a limitation in level of detail since it can only capture the shade for panel level or only for one location. These methods are found to be insufficient for a partial shade study in capturing a small area of shadows that affects electrical mismatch in PV module.

Therefore, in this work a 3D modeling framework based on vector algebra concept is adopted [50, 31, 51]. The framework offers a high-granularity, flexibility, and good accuracy in determining arbitrary shading pattern on cell-level. Technically, this method utilizes the XYZ coordinates of PV module and shade objects that is obtained from 3D model in any CAD software. In this work, the combination of Sketch Up as the CAD software and Python programming language

[2]Note that Global irradiance is a decomposition of diffuse and direct component

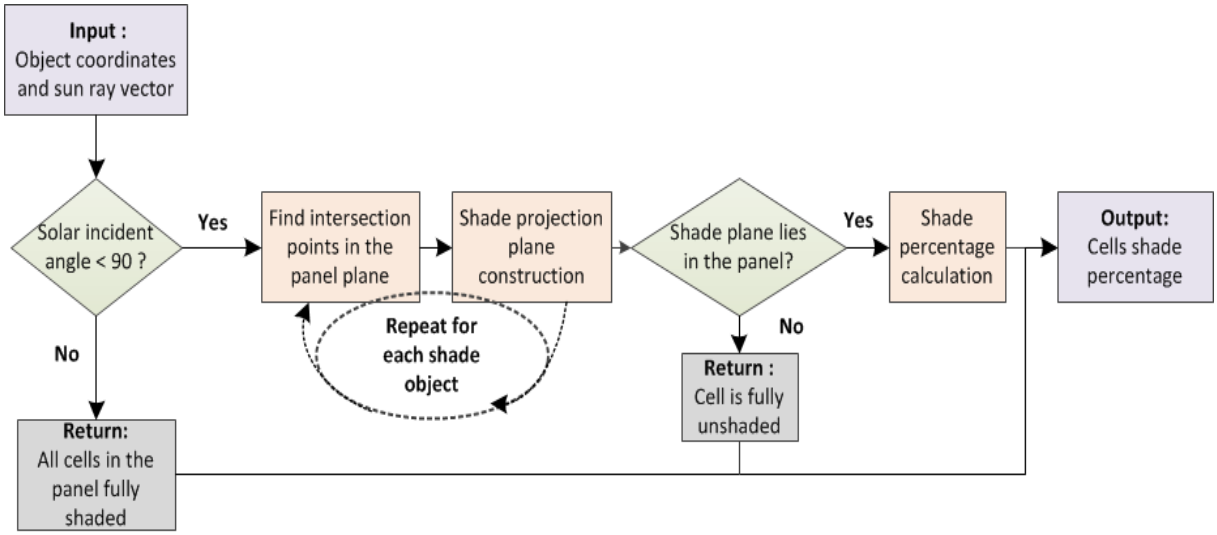

Figure 3.5: The algorithm of shade projection model to calculate the cell shade percentage for a single sun position.

environment to compute the shade calculation is opted. The algorithm used to calculate the shading fraction is explained in figure 3.5. The mathematical and modeling framework of each block inside the flowchart will be explained in subsequent sections.

It should be emphasized that the shading calculation is dependent on the geometry of the module and shade objects as the function of position of the sun in the sky. It means, the shading fraction can be calculated for a full sky hemisphere prior to the irradiance calculation. These values can be stored in a form of lookup-table. This lookup-table is versatile since it can be used to calculate a specific geometry panel for any location in the world. To ensure the level of accuracy, the shading fraction of each cell is calculated by one degree interval of azimuth and altitude pair (32400 sun positions) without any interpolation.

Panel and object Cartesian coordinates determination

The very first step in shading calculation is the creation of 3D geometrical object in CAD software environment. In this particular work, the 3D design follows the PVNB design reference that has been elaborated in section 2.2 which is visually represented in figure 3.6. Starting from this 3D model, the X,Y, and Z coordinates of each point of interest in the object can be extracted. These coordinates can be retrieved by using Point Gadget plugin in SketchUp [52].

Solar panel can be regarded as a rectangular flat surface which has four edge points. Apart from determining the position of the panel in Cartesian coordinate, these corner points can be used to calculate the length and the width of the panel (by calculating the length of the vector). In addition, rather than extracting the coordinates of each cell in the panel manually, the segmentation of each cell in the panel can be derived by proportionally dividing the length and width of the panel by the amount of horizontal cells and vertical cells in the panel. The distance between the cells in the PV module is also included as one of parameter input in the python scripts. The product of this cells segmentation, as well as cell numbering, are illustrated in figure 3.7.

Likewise, the same procedure in extracting the X,Y, and Z coordinates is applied for the shade objects in the model. In this PVNB example, the shade objects are comprised of top, bottom, and side metal structures in noise barrier that formed as cuboid shape model. The detail of object shape can be modeled by separating each structure into a small cuboid objects.

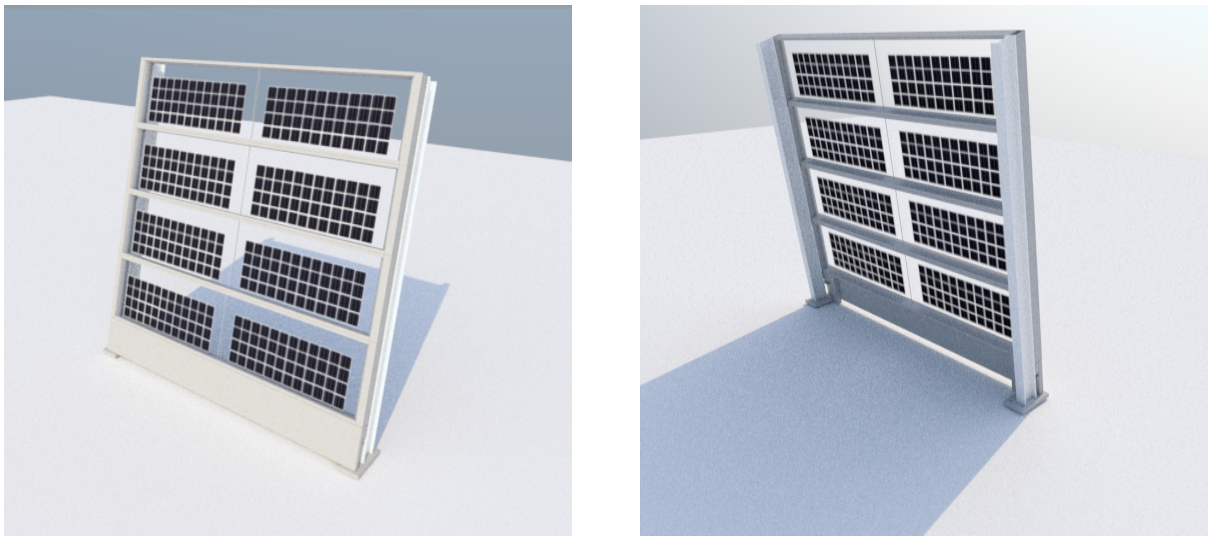

(a) (b)

Figure 3.6: 3D Realistic rendering view of studied PVNB Design created in Sketchup (a) Front view (b) Rear view. The design is derived from the concept explained in section 2.2.

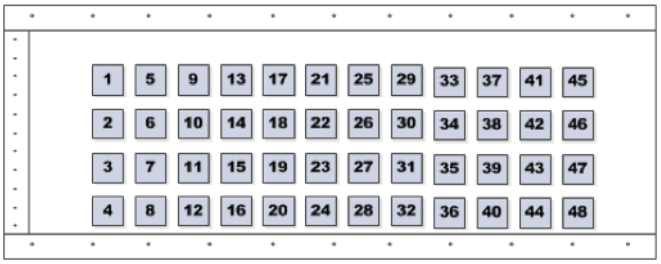

Figure 3.7: Illustration of the cell division and numbering of the panel. The PV panel pictured in the figure is the representation of left side panel in each section. The same numbering order is applied to the other PV modules in the model. Whereas, the numbering of the rear surface follows the front side arrangement.

To reduce the unnecessary calculation, the simulation starts with evaluating the angle of incidence (AOI) to check the condition whether the sunlight could reach the panel. If it is not the case or $AOI > 90^o$, the sun is located behind the surface panel and the panel is in fully shaded condition. On the contrary, if $AOI < 90^o$, the shadow projection from each obstacle need to be evaluated and the following procedures need to be performed (see the step in figure 3.5).

Intersect points calculation

The shadow shape that is generated by the surrounding obstacles can be obtained by projecting a shade object point (Po_x, Po_y, Po_z) along vector $\vec{V}_{sun}$ until this vector is intersected on the interested surface plane (Pm_x, Pm_y, Pm_z). Refer to figure 3.8 for the illustration. In vector algebra, this procedure is defined as a line parameterization that can be found by using equation 3.11 [53].

$$\begin{bmatrix} Pm_x \\ Pm_y \\ Pm_z \end{bmatrix} = \begin{bmatrix} Po_x \\ Po_y \\ Po_z \end{bmatrix} + t \cdot \vec{V}_{sun} = \begin{bmatrix} (Po_x + t \cdot S_x) \\ (Po_y + t \cdot S_y) \\ (Po_z + t \cdot S_z) \end{bmatrix} \tag{3.11}$$

Where t is the constant of its line parametrization that is very important to evaluate the location of the shade object in a given sun position.

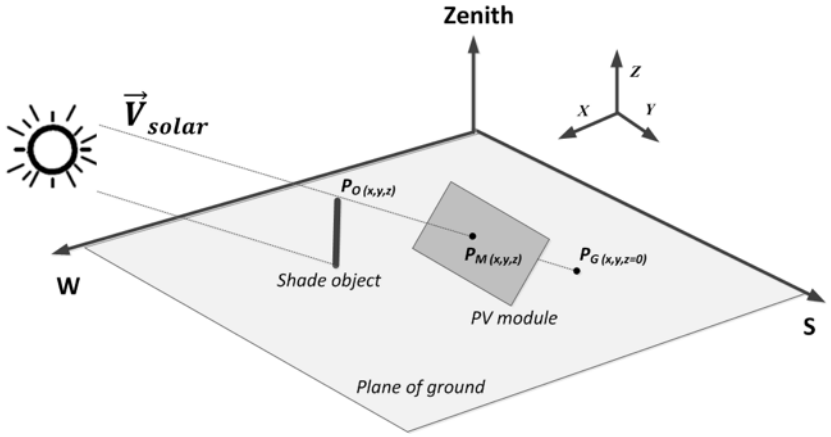

Figure 3.8: Illustration of sun ray vector cast the object shape into the model.

This line parameterization constant (t) can be calculated by letting the intersection point (Pm_x, Pm_y, Pm_z) into the PV module equation plane $ax + by + cz = d$.

$$d = a(Pm_x) + b(Pm_y) + c(Pm_z) = \begin{bmatrix} a(Po_x + t \cdot S_x) \\ b(Po_y + t \cdot S_y) \\ c(Po_z + t \cdot S_z) \end{bmatrix} \tag{3.12}$$

Hence,

$$t = \frac{d - (a(Po_x) + b(Po_y) + c(Po_z))}{a(S_x) + b(S_y) + c(S_z)} \tag{3.13}$$

Then, for any n shade object point(Pn_x, Pn_y, Pn_z) that generates n intersect points (n_x, n_y, n_z) in the same PV module plane, the previous formulation can be redefined as:

$$t_n = \frac{d - (a(Pn_x) + b(Pn_y) + c(Pn_z))}{a(S_x) + b(S_y) + c(S_z)} \tag{3.14}$$

To evaluate whether the point projection was crossing through the panel plane or not, a line parameterization constant (t) value has to be greater than zero (t>0). This condition represents the situation when the object is located between the sun and PV panel and hence shadow may be casted into the PV panel. Contrary, the shadow point projection is never passed through the panel plane when t has a negative value (t<0). This situation represents the condition when the panel is located between the sun and the shade object.

Shading projection and shade percentage calculation

After the determination of intersect point procedure is repeated for all points of the shade object in the model, the shape of the shading polygon projection in panel plane can be assembled by connecting the vertex [3] found on the PV module plane. To connect these outward points, the so-called convex hull algorithm by Graham Scan [54] is used. Figure 3.9 shows the graphical illustration of convex hull procedure in forming the polygon-shape of the shadow from the intersect points. Note that the total shadow polygon lies in the PV panel plane does not necessarily have to intersect the solar PV itself (see figure 3.9a).

[3] The most outwards points

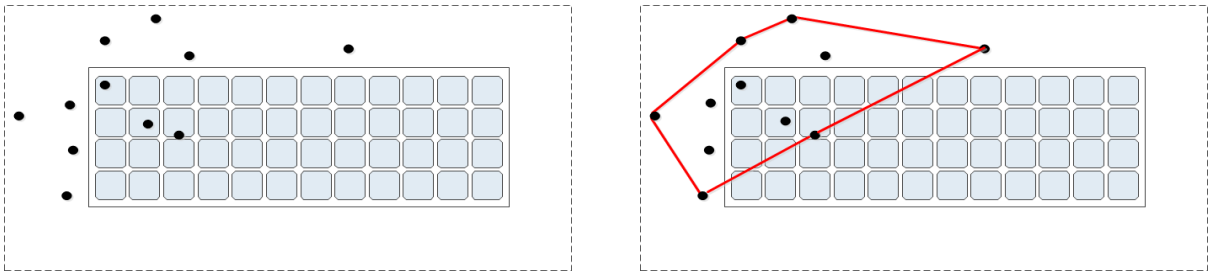

(a) Intersect points at PV module plane **(b)** Convex Hull Procedure

Figure 3.9: The interconnection of the shadow points on the PV module plane. The convex hull method is used to connecting the most outwards points to be a convex polygon (right). Dashed point represents the expansion of panel plane where the shadow projection points might intersect.

If there are multiple shade objects, the previous procedure then is repeated for all shading objects that has been determined in the model (see the step in figure 3.5). The total shadows that fall on the plane then can be obtained by overlapping the individual shadow projection from the shade objects. These overlap shadow projection are subtracted to get the final shadow projection in the panel plane.

Finally, the final evaluation is done by checking whether the shade projection plane lies in the PV module plane. If the shade plane fully or partially lies in the panel then the shade calculation is performed. Shade percentages of the cell can be determined by the ratio of cell area covered by shadow polygon to the total cell area. Alternatively, the aforementioned definition can be found by evaluating the amount of 10 by 10 grid points in cell polygon that lay inside the shadow polygon (See illustration of the cells in figure 3.10).

To give an example the shading fraction calculation, a panel under partial shade condition is illustrated in figure 3.10. It can be observed from the figure that the cells can be classified into three category condition, fully shaded, partial shaded, and unshaded condition. In partial shaded cell, there are 62 points lay inside the shadow polygon, meaning that the cell shade percentage of the corresponding cell is 62% (Refer to the middle cell representation in figure 3.10).

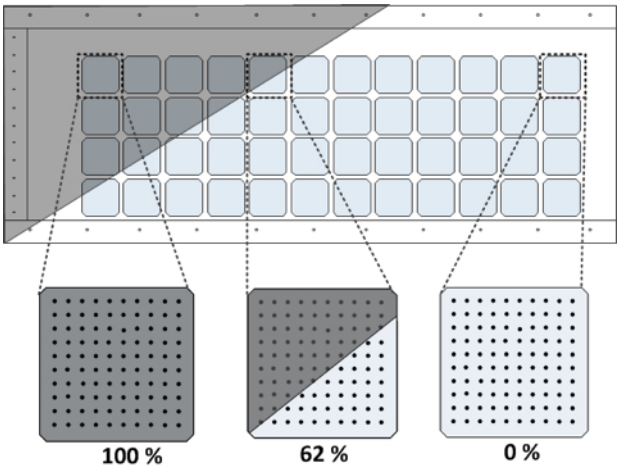

Figure 3.10: Demonstration of shade fraction calculation of cells in a PV module under partial shade condition. The first cell (left) represents the condition when the cell get fully shaded that has 100% shading fraction. Whilst the partial shade condition is demonstrated by the cell in the middle.

3.2.3 View factor for ground irradiance correction

Recalling the explanation in section 2.3.2, the view factor is denoted as a double surface integral over two surfaces j as the shadow on the ground and i as the cell in the PV module (Refer to equation 2.3). The value of this view factor is ranging from 0 to 1. This complex mathematical expression generally can be solved by Monte Carlo method or other complex mathematical solver.

However, in this work, a procedure to solve the complex double surface integration was invented. As an alternative to the complex numerical solver, the view factor from cell to the shaded ground can be solved by initially discretizing both surfaces into small finite subsurfaces. Then the view factor between these differential elements dA_i and dA_j are calculated and finally the double integral of Riemann approximation is used to get the final product of view factor of the cell to the ground shade. Hence, equation 2.3 can be rewritten as expressed in equation 3.4.3.

$$VF_{i\to j} = \frac{1}{A_i}\sum_{i=1}^{n}\sum_{j=1}^{m}\frac{\cos\theta_i \cdot \cos\theta_j}{\pi \cdot r^2} dA_i dA_j \tag{3.15}$$

Thankfully, the 3D geometrical approach used in this model align with this method which requires Euclidian vector calculation. The same procedure of shadow projection is used to determine the coordinates and shadow polygon of the ground. It can be done by replacing the PV panel plane by the (X ,Y ,0) equation plane (Ground is lying on X-Y plane, also see P_G in figure 3.8). After the ground shade polygon is obtained, this shadow area can be discretized into small triangles by using the Delaunay triangular mesh. This meshing procedure follows the algorithm created by Shewchuk. T [55]. The mesh quality is controlled in the python script by restricting the area of each triangle to be not greater than 50 cm^2. Figure 3.11 visualizes the meshing procedure for a shadow on the ground. Furthermore, the solar cell is divided into four equal regions which has 60 cm^2 surface area.

By having two surfaces discretized, the view factor then can be obtained by first integrating the differential view factor of cell mesh to each shadow ground mesh $VF_{d_i\to j}$ $(i = j \dots m)$ and iterates through each small element of the cell mesh $(i = 1 \dots n)$. Where m and n are the number of mesh in the ground shadow and cell respectively. To calculate each component in equation 3.4.3, vertices[4] of the triangles dA_i and dA_i are used to determine the baricenter of

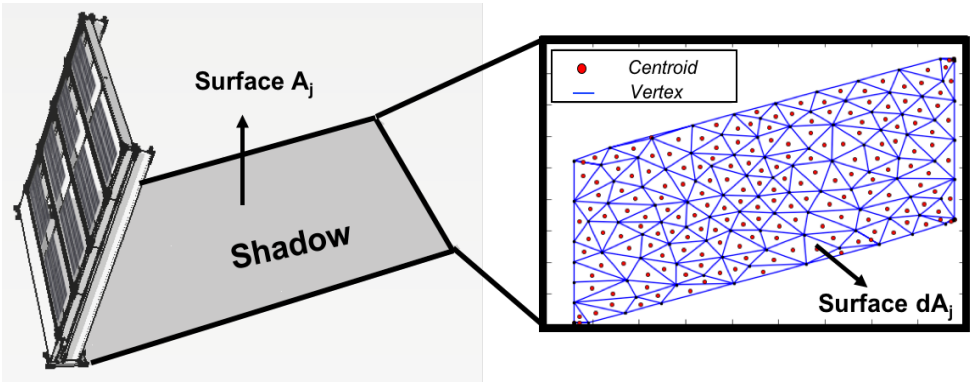

Figure 3.11: Illustration of meshing procedure of the ground shadow where the blue lines represent the vertices of triangulation mesh. The quality of mesh here is 100 cm^2 (coarse mesh). The centroid of each triangular mesh is important for r calculation.

[4]Line that connecting two vertex in triangle

the triangle. Center points C_i and C_j used to determine $\vec{V_r}$ where length r can also be found simply by calculating the magnitude of $\vec{V_r}$. The normal angle between corresponding surface and vector r can be found by $\cos\theta_i = \vec{V_r} \cdot \vec{Vn}_{d_i}$ and $\cos\theta_j = \vec{V_r} \cdot \vec{Vn}_{d_j}$. Lastly, the area of triangle element has to be calculated individually due to irregular size of the mesh (refer to figure figure 2.7).

3.3 Ray tracing model

Ray tracing method offers an optically realistic simulation for irradiance calculation of solar PV application. This method is powerful to model the irradiance distribution on PV with a complex geometry. In this study, we perform the ray tracing simulation using the advanced ray tracing software LightTools. Santbergen introduced this new irradiance calculation method by applying this method to a zig-zag solar PV configuration [56].

Ray tracing method can be an alternative solution to substitute the numerical model for the bifacial module under partial shading simulation. Figure 3.12 shows the general overview of the optical model using Ray Tracing method.

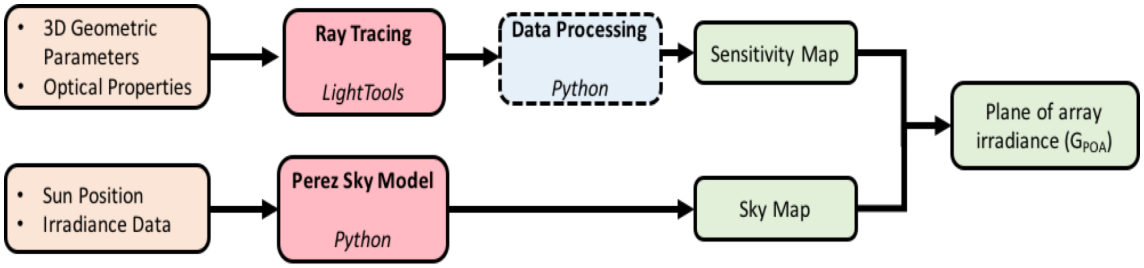

Figure 3.12: overview of irradiance model of ray tracing method

As depicted in figure 3.12, the optical model to calculate incident irradiance using the developed ray tracing model consist of two main sub-model. The first sub-model calculates a so-called sensitivity map value for each respective cell in the module. This first sub-model is mainly used a 3D model created in LightTools software. Secondly, the distribution of sky radiance for a particular site location is calculated by using Perez sky model [57]. Finally, these two sub-models are integrated to yield the incident irradiance of the cell.

$$Irradiance = \int_{sky} skymap \cdot sensitivity\,map\, d\Omega \tag{3.16}$$

3.3.1 Sensitivity Map

The first step of ray tracing simulation is the creation of a 3D geometrical object in LightTools optical software. For this work, the 3D model of PVNB follows the design as illustrated above in section 2.2, that is also implemented in 3D SketchUp design (Figure 3.6). The design includes the dimension of the objects, the number of panels, and the number of cells in the panel. Figure 3.13 depicts the illustrations of a 3D model built in LightTools.

Several aspects were improved from the previous model. First, to realistically mimic the glass-glass PVNB configuration, the solar cells in the panel were immersed into the glass. This can be done by first trimming a rectangular shape inside the glass which has the same dimension as a single solar cell. Then the cell can be created inside this area and later set to be immersed into the glass. In addition, reflected irradiance was not incorporated in the previous model. In

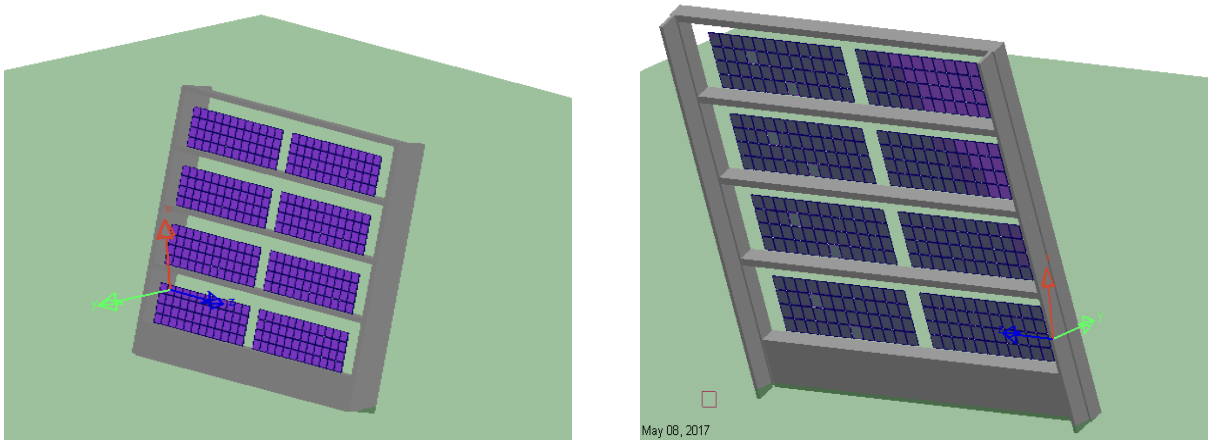

(a) (b)

Figure 3.13: 3D PVNB Design created in LightTools (a) Front view (b) Rear view. Green surface represents the ground surface that has certain albedo value.

this work, the dummy ground with a certain albedo coefficient (assumed as perfect lambertian surface) is created in the model to accounts the reflected irradiance component.

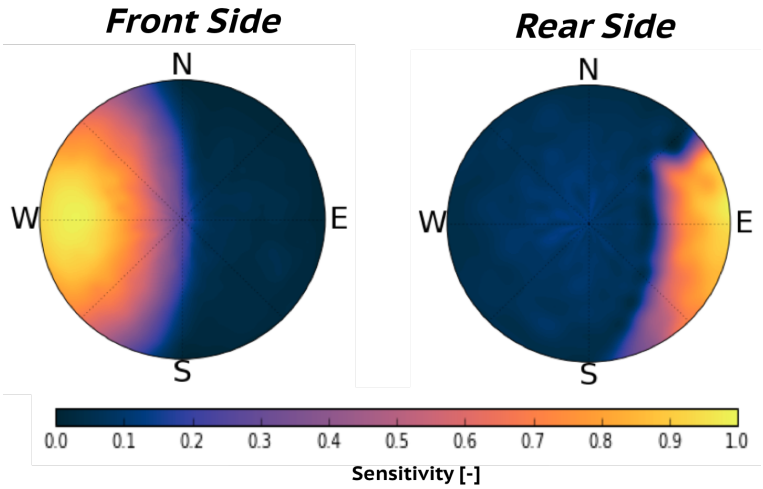

Figure 3.14: Sensitivity map of front side and rear side of bifacial solar cell number 1. Refer to figure **??** for the cell numbering legend.

A simulation step takes place by tracing 2.5 million rays from the light source created in the simulation, for every single position in the sky. Figure 3.14 gives the example of the sensitivity map of a single bifacial solar cell produced from the simulation. Note that for a bifacial solar cell, two sensitivity maps are created to represent the front and rear side of the cell.

3.3.2 Sky map

Sky model is able to generate a continuous sky luminance pattern for a specific location on the earth. Perez All-weather model is that has a key feature to generate various sky conditions, from overcast through the clear sky is used [57]. Unlike the Perez diffuse irradiance model that has been explained in section 3.2.1, this Perez model incorporates the penetration of direct sunlight angular distribution. The sky dome was first meshed into regular grid in similar fashion to the creation of sensitivity map.

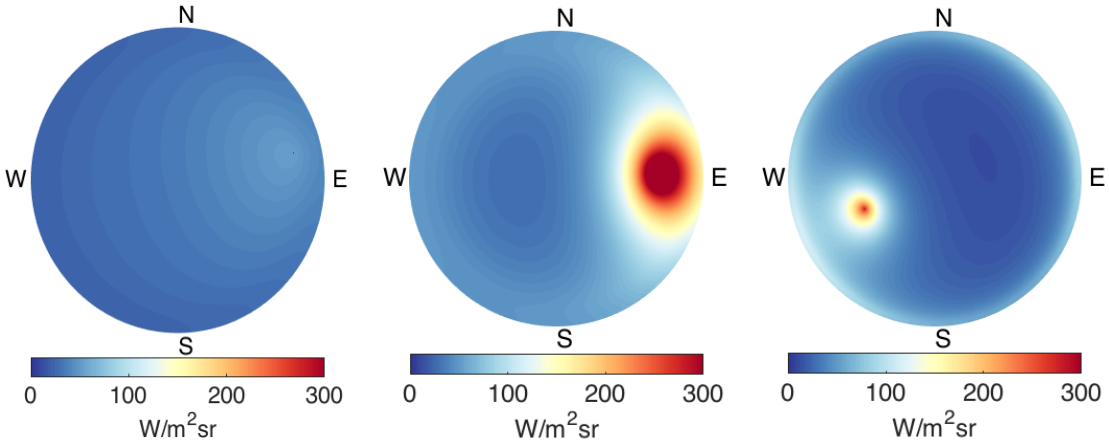

(a) Overcast **(b)** Intermediate **(c)** Clear

Figure 3.15: Examples of Sky Map generated by the Perez Model in three different weather conditions. Figure (a) represents the cloudy condition when the Sun is not appeared. The bright spot in figure (b) and (c) depicts the sun position in the sky. While the broader bright area in figure (b) indicates the influence of a cloud to the circumsolar distribution.

The real sky luminance (Lv)at any considered grid in the sky dome (ς_{sky}) can be obtained from lv via normalization to diffuse illumination (DHI) over the entire grid in the sky dome which expressed in equation 3.17. Where lv defines the radiance distribution at the considered grid in the sky dome and can be calculated using several empirical coefficients based on clearness index and sky brightness explained in the author paper [57].

$$Lv = \frac{lv \cdot DHI}{\int_{sky}(lv \cdot \cos(\varsigma_{sky}))d\Omega} \tag{3.17}$$

Finally, the visualization of the sky map is plotted in spherical/polar coordinate as depicted in figure 3.15. It must be pointed out that this sky map calculation continuously changing for every different sun position and sky condition.

3.4 Validation of the numerical geometry model

The validation of numerical geometry model is evaluated by comparing simulation results with other developed tools, ray tracing model, and outdoor experiment. First the simulated shading patterns from the shading model in section 3.4 are compared with the shadow animation from Sketch Up. After this verification, the implementation of shading model to irradiance distribution calculation is compared to the simulation from ray tracing approach. Finally, the view factor model in is validated by outdoor experiment data to see the influence of the shadow on the ground to the back side irradiance.

3.4.1 Comparison between the proposed shading model and SketchUp

SketchUp is a well-established tool that can provide shadow projection of 3D model for any given time. However, the shadow projection does not contain any shading fraction data that is needed for irradiance calculation in this work. This is why a shading model that has been developed in this thesis is required.

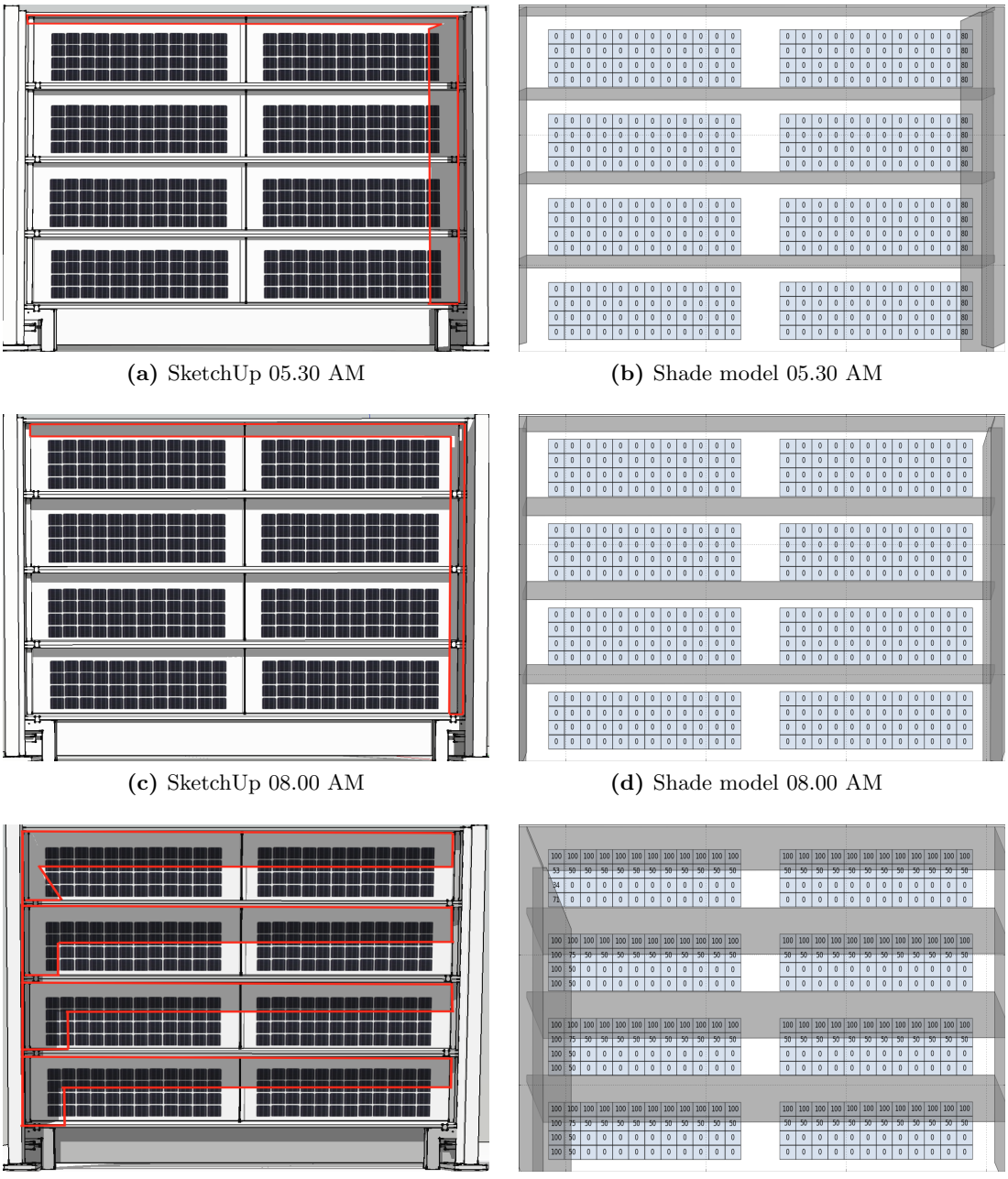

(a) SketchUp 05.30 AM

(b) Shade model 05.30 AM

(c) SketchUp 08.00 AM

(d) Shade model 08.00 AM

(e) SketchUp 10.00 AM

(f) Shade model 10.00 AM

Figure 3.16: Pictures on the left side (a,c,e) generated from sketchUp while pictures on the right side (b,d,f) are the result from numerical model that plotted in Y-Z plane. The pictures show the transition of shading conditions on rear surface of west-facing PVNB.

Figure 3.16 gives the validation of the simulated shading projection with the result from SketchUp. The figures on the left sides are the screenshots of condition that are produced by Sketch Up. The figures on the right side represent the plot of simulated shading projection (gray polygons) on rear side the bifacial solar cells (blue rectangular) along with the shading fraction of each cell in Y-Z Cartesian coordinates.

Three instances 5.30 AM, 08.00 AM, and 10.00 AM are selected to show the transition of shading pattern of a clear sunny day in June. These comparisons are reported in figure 3.16. The shading patterns for this type of PVNB typically are rather formed in rectangular shape, in horizontal and vertical orientation. This is strongly influenced by the shape of the structure

itself. Furthermore, it can also be observed that left and right bifacial panel suffer different shading pattern in a very short time period. The figure shows that, in early morning when the sun located in north east and very low altitude angle, the module on the right sides experience a partial shading condition caused by the right structure (located more to the East). As the time goes by, the vertical shading is gone and then the top structures starts casting a shadow to the 12 cells in the top row due to the high elevation angle of the sun during this period. Since then, the shadow also begins to appear from the left side (the sun starts moving towards south) and the modules are severely suffered from shading conditions.

On top of that, a good agreement between the SketchUp references and model prediction is presented by the similarity of the shading patterns that are generated by both tools in figure 3.16. This shows the model used in this work is reliable. Furthermore, the proposed model offers a greater information detail that is illustrated by the number inside the cell, which represents a shading fraction value at instantaneous time.

3.4.2 Comparison between shading model and Ray tracing

To verify the accuracy of shading model implementation into the irradiance calculation, the ray tracing model was used to validate the accuracy of the proposed numerical model. Here, the 3D geometrical parameters in both model were setup to be identical for west facing bifacial PVNB. The incident irradiance for each cell was calculated for one sunny day in June similar to the day that are selected for shading pattern comparison. The timespan when the self-shading phenomena are occurred, between 8.30 AM and 11.00 AM for every half an hour interval are selected (after 11 AM the rear surface is completely shaded).

It was shown previously that the shading patterns for module in the same column are similar

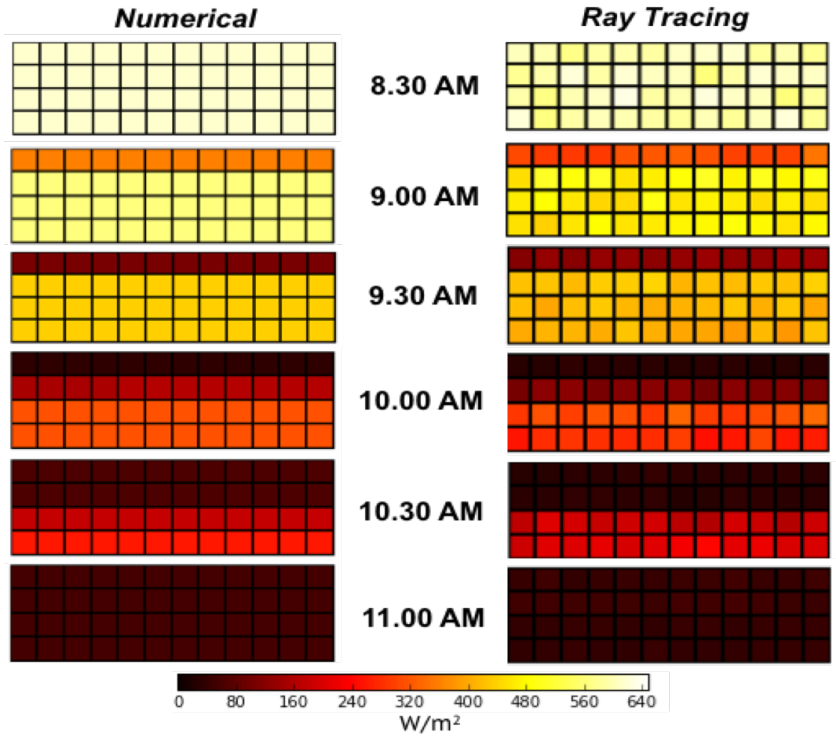

Figure 3.17: Comparison of the numerical geometry model (left) and ray tracing (right) irradiance distribution results on the rear side of bifacial PV module. color bar indicates the irradiance distribution scale of each cell in the module.

(see figure 3.16). Furthermore, the front side of the module is assumed to be free from shading. Hence, to avoid a repetition, only one rear surface of the module was chosen here as a validation example.

The calculated irradiance distributions on each of 48 cells by both approaches are represented in figure 3.17. A good agreement between the numerical model and ray tracing model is shown by the similarity of color gradation throughout the validation time. For example, partial shading conditions on the top row cells appear at 09.00 AM. Next the shadows gradually go down to fully shades the first row and then start reaching the second row and so on until 11.00 AM, when all cells in the module are get shaded. However, the ray tracing model has slightly darker color in overall. The influence of reflected irradiance from surroundings can be a possible reason for this deviation. Despite the same albedo value was applied in both model ($\alpha = 0.2$), the reflected irradiance in ray tracing model might slightly limited by the area of the dummy ground (green area in figure 3.13).

3.4.3 Validation shaded ground effect

To verify the influence of shadow on the irradiance in different height, a straightforward validation experiment was conducted. The experiment was carried out at the Solarbeat facility test, TU Eindhoven (5.45^{o}E, 51.41^{o}N). Two secondary EKO pyranometers are installed at the back side of a dummy house at 1 m (bottom) and 3 m (top) elevation from the facility test ground. As can be seen in figure 3.18, the pyranometers are configured vertically (tilt angle 90^o) and facing north direction. These pyranometers are assumed to represent rear side of two bifacial solar cells in PVNB. A data logger inside the dummy house was connected to those pyranometers and fetching the data in one-minute resolution.

In this facility, the irradiance is measured by a central Solar Measurement Station (SMS). This SMS is comprised of with a first class pyrheliometer for the Direct Normal Irradiance (DNI), a secondary standard pyranometer with shading ball for the Diffuse Horizontal Irradiance (DHI), and an unshaded secondary standard pyranometer for the Global Horizontal Irradiance (GHI). These measured irradiance are used as the input for the model. The reflected irradiance calculation of the rear side of bifacial module in equation was used. The sky view factor was corrected by the amount of sky horizon blocked by the high rise building at the test location. The Cartesian coordinates of object surroundings that used for shading and view factor calculations were retrieved from 3D Sketchup model as depicted in figure 3.18. The view factor calculations followed the procedure explained in 3.2.3.

(a) Real site **(b)** CAD Model

Figure 3.18: Figure (a) Depiction of outdoor experiment setup in Solar beat facility test, Eindhoven. Note that two pyranometers are installed at 1m and 3m from the ground respectively. Figure (b) shows the Sketchup drawing of the site that has been used to retrieve the cartesian coordinates of the shading object and pyranometers for the model inputs.

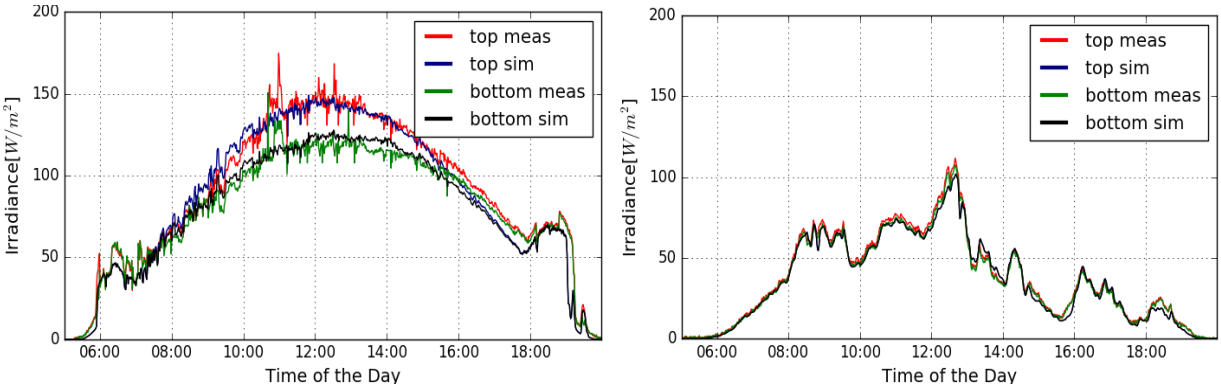

(a) Sunny Day 20^{th} April 2017 **(b)** Cloudy Day 14^{th} April 2017

Figure 3.19: Validation of the influence of shadow on the ground in reducing the amount of reflected irradiance. Note that the influence of the shadow is less pronounced during a cloudy day.

Figure 3.19 demonstrates the irradiance comparison between the measured and simulation for the two pyranometers on a sunny day and a cloudy day. The difference of irradiance received by two pyranometers have been clearly showed by both measurement and simulation. As expected, by looking at figure 3.19a, top pyranometer was experienced a higher irradiance than the one in a lower elevation during a sunny day. With the higher gap was occurred during noon time with approximately 20% difference. During this time, the Sun is located in the south and induces the shadow projection to the ground from the dummy house. On the other hand, the influence of ground shaded is almost negligible during a cloudy day (figure 3.19b) since there is almost no direct component that is available in a overcast day condition. However, during a sunny day, deviation was occurred in the afternoon. It was shown that the measured irradiance (top and bottom) are proportionally higher than the model. A reflection from the tall building in front of the pyranometer is a possible cause that yields this discrepancy.

The result of model validation in figure 3.19 proves the reliability of the view factor approach implementation in the reflected irradiance correction explained in section 3.2.3. This experimental activity also confirmed the theory that has been elaborated in section 2.3.2. Hence, the simulation study to see the yield performance of bifacial PV module under different elevation can be performed.

Model Discussion

The validity and accuracy of the developed numerical geometry model were adequately evaluated in three different steps. First, the shading projection generated by the shading model was validated with a well-recognized 3D-architectural software, Sketchup. Then a good confirmation of irradiance calculation (that incorporated shading fraction) with respect to a realistic ray-tracing approach was reported. The last validation with experiment that was conducted in outdoor environment also proved the irradiance reduction caused by the shadow projection on the ground. Thus, by referring to these validation, the proposed numerical geometry approach was demonstrated as a valid tool to perform incident irradiance calculation on bifacial PV module.

With regards to the comparison between the numerical geometry model and ray tracing model, both concepts are found to be suitable for aiding partial shade simulation at high-granularity level. Several similarities are found in both approaches. Both approaches offer a flexibility irradiance calculation of PV module that surrounding by arbitrary shading object.

Ray tracing approach, on the one hand, is advisable to be used for more realistic optical modeling investigations which are impractical for the numerical geometric approach. For instance, to accounts the amount of light transmitted within the glass-glass construction, internal reflection between the glasses, and reflection from the metal structures. On the other hand, the developed numerical geometric approach is also capable in predicting the non-uniformity irradiance distribution. The developed framework appears to be much more advanced and accurate than the common irradiance model in a text book [22]. Further improvement suggestions for both model will be explained in the recommendation chapter.

CHAPTER 4

Temperature of the glass-glass bifacial PV module

PV module temperature is one of the most critical variables that affects its electrical performance. In regards to the double glass construction of bifacial PV in noise barrier systems, the essential thermal heat transfers in this type of module act differently compared to the conventional PV commercial panel. As was mentioned in the literature review (section 1.3), up to this stage a thermal model for bifacial PV module that considered the energy balance approach was not studied so far. Therefore, the goal of the work described in this chapter is to develop a thermal model that can incorporate the glass-glass structure of the module as well as the influence of the wind speed and both illumination from the front and rear side of the module.

In section 4.1 the NOCT model that mostly used by current research is explained. Next, the proposed thermal model based on finite element and energy balance approach is introduced in section 4.2. The evaluation of the developed model is given in section 4.3.

4.1 Simple NOCT Model

There are currently well-known thermal models available that provide either empirical or an energy balance. The most well-known and widely used is by using the NOCT (Nominal Operating Cell Temperature). This model is regarded as the simplest model but least accurate. This is due to the absence of wind speed and other external parameters which in reality play a major role in determining the module temperature.

$$T_{PV} = T_a + \frac{T_{NOCT} - 20^o}{800} \cdot G \tag{4.1}$$

The model calculation showed in equation 4.1 has been widely used for a commercial module application. However, a linear relation between the cell temperature (T_{PV}) and irradiance (G) deployed in the NOCT model is not suitable for a BIPV area, for instance, a vertical noise barrier application, since the ventilation effect due to the vertical installation is not considered in the model. Therefore, a more comprehensive model is proposed in this study as described in the following section.

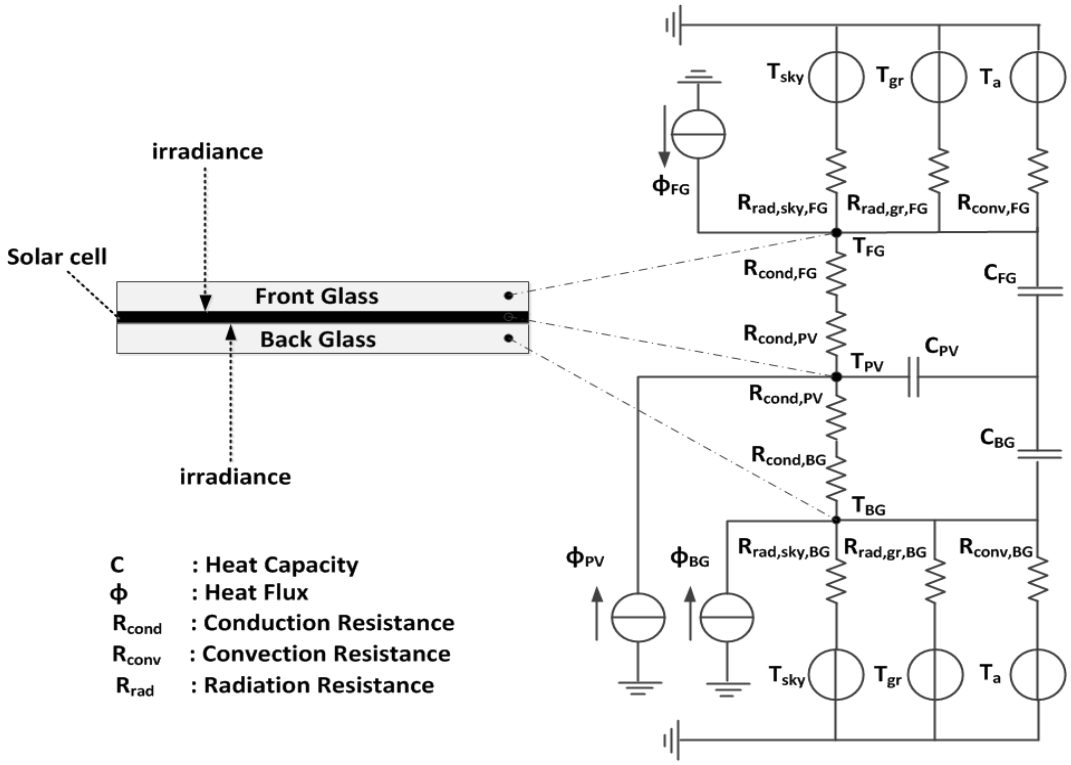

Figure 4.1: Equivalent thermal network resistances of glass-glass bifacial PV module.

4.2 Finite element model

The temperature of a PV module can be more accurately predicted by modeling the energy balance within the system. A thermal model that implements this concept is presented in [58] [22]. However, this model assumes all component of PV module (glass, solar cell, backside module) as a single layer which is might not be the case for a thick glass-glass PV module. Another model using a finite element model is introduced by Notton [59]. This model is built for a glass-glass PV module in which, various hypotheses and expressions are tested and validated with RSME error of 1.3°C. This finite element model is applied in this work.

Nevertheless, since the model is developed for the standard monofacial solar cell, the model then being extended as bifacial solar cell allows irradiance from the rear side which introduces additional heat to the rear side of the module. This is done by incorporating the heat flux of the back side of the module into the energy balance.

The main principle of this model is by discretization of a PV module into three isothermal nodes: the front glass cover (FG), the photovoltaic cells, and the black glass cover (BG) as shown in figure 4.1.

Moreover, the model calculates the temperature for each time step by assuming several conditions.

- Thermal exchange between PV cells and EVA is assumed negligible.
- The ambient temperature is postulated as equal on all side of the module.
- The PV module is only divided into horizontal sections and no thermal exchanges by the PV module sides are incorporated in the model.
- Steady state condition is considered in solving the overall energy balance.

By looking into figure 4.1, radiative, convective, and conductive heat exchange between the nodes (T_{FG}, T_{PV}, T_{BG}) are taken into account in the thermal energy balance calculation. The main thermal balance equations of front glass (T_{FG}) and rear glass (T_{BG}) are given in the equation 4.2 and 4.3 respectively. Whereas, equation 4.4 holds the energy balance expression for cell temperature (T_{PV}). To present the equations in more convenient way, from now on H is used to replace the resistance R ($H = 1/R$).

$$mC_{FG}\frac{dT_{FG}}{dt} = H_{conv,FG,a}(T_a - T_{FG}) + H_{r,sky,FG}(T_{sky} - T_{FG}) + H_{r,gr,FG}(T_{gr} - T_{FG}) + H_{cond,FG,pv}(T_{PV} - T_{FG}) + \phi_{FG}A_{PV} \tag{4.2}$$

$$mC_{BG}\frac{dT_{BG}}{dt} = H_{conv,BG,a}(T_a - T_{BG}) + H_{r,sky,BG}(T_{sky} - T_{BG}) + H_{r,gr,BG}(T_{gr} - T_{BG}) + H_{cond,BG,pv}(T_{PV} - T_{BG}) + \phi_{BG}A_{PV} \tag{4.3}$$

The terms involved in equation 4.2 are the derivation of the heat transfer interconnected in node T_{FG}. This includes the exchange between the front glass and the environment by convection and radiation, exchange with the solar cell, and additional heat flux caused by the light absorption in the glass layer. Likewise, the same phenomena occur in back glass (equation 4.3). In contrast, only conduction exchange is experienced in the solar cell node due to the direct contact between the front glass and back glass without any presence of air gap in between (equation 4.4).

$$mC_{PV}\frac{dT_{PV}}{dt} = H_{cond,PV,FG}(T_{FG} - T_{PV}) + H_{cond,PV,BG}(T_{FG} - T_{PV}) + \phi_{PV}A_{PV} \tag{4.4}$$

Owing to the steady state assumption in the calculation, the effect of the heat capacity of the system is neglected and hence the expression on the left side of equation 4.2,4.3, and 4.4 become zero. Finally, by linearizing all terms in these three equations, the formula in determining T_{PV} can be governed as follow:

$$T_{PV} = \frac{T_{FG}H_{cd,PV,FG} + T_{BG}H_{cd,PV,BG} + \phi_{PV}A_{PV}}{H_{cd,PV,FG} + H_{cd,PV,BG}} \tag{4.5}$$

However, T_{FG} and T_{BG}, are the function of T_{PV}. Hence, the equation 4.5 needs to be solved iteratively. It can be done by initializing the ambient temperature and the glasses temperature values. Inside this iteration loop, all heat transfers phenomena expressed in aforementioned equations need to be calculated individually. The detail of heat exchange expressions are listed in table 4.2. Where notation i or j represents for each respective surface nodes (FG, PV, BG).

Table 4.1: A set of heat transfer equations used to solve the energy balance

Parameters	*Equations*	
Conduction	$H_{cond,i,j} = \lambda_i A/d$	(4.6)
Overall convection	$H_{conv,i} = (h^3_{conv,force,i} + h^3_{conv,free,i})^{1/3}A_i$	(4.7)
Forced convection	$h_{conv,force,i} = 5.67 + 3.86\upsilon$	(4.8)
Free convection	$h_{conv,free} = 1.31(T_g - T_a)^{1/3}$	(4.9)
Sky Radiation	$H_{rad,sky,i} = \varepsilon_g F_{sky,i}\sigma A(T_i + T_{sky})(T_i^2 + T_{sky}^2)$	(4.10)
Ground radiation	$H_{rad,gr,i} = \varepsilon_g F_{gr,i}\sigma A(T_i + T_{gr})(T_i^2 + T_{gr}^2)$	(4.11)

In table 4.2, λ_i represents the conductivity value for each material, where $\lambda_{glass} = 1\,Wm^{-1}K^{-1}$ and $\lambda_{PV} = 149\,Wm^{-1}K^{-1}$. d stands for the thickness of the glass and solar cell. Whereas, in forced convection equation 4.8, the influence of wind speed is denoted by υ. Note that the impact of linear and turbulent regime is already incorporated in the empirical equation 4.8.

In equation 4.10 and 4.11, $\varepsilon_g = 0.85$ is the emissivity value of the glass. ϵ is the Stefan-Boltzman constant. $F_{sky,i} = 0.5(1 + \cos\beta)$ and $F_{gr,i} = 1 - F_{sky,i}$ are the configuration factor for respective tilted surface with angle i β to the sky and ground. Where ground temperature (T_{gr}) is assumed to be equal to ambient temperature (T_a) and sky temperature (T_{sky}) can be calculated by $T_{sky} = 0.0552 \cdot T_a^{3/2}$.

ϕ_{PV} denotes the heat flux from the solar radiation absorbed by the solar cell after being passed through the glass from either side. Typically only less than 15% of the incident irradiance is converted into electricity, with the remaining quantity is being converted into heat which significantly affects the energy balance at the PV module. This parameter is mathematically expressed in 4.12. Where cell coefficient to absorb irradiance (α_{PV}) has a value of 0.9 and transmittance value of the glass (τ_i) has a value of 0.85. For simplification, the power generated from PV (P_{PV}) in equation 4.12 is calculated using the correction of efficiency by the module temperature.

$$\phi_{PV} = \alpha_{PV} \cdot \tau_i \cdot (G_{FG} + G_{BG}) - \frac{P_{PV}}{A} \tag{4.12}$$

The final two expressions ϕ_{FG} and ϕ_{BG} represent the incoming heat flux per unit area due to the absorption of solar irradiance by the front and rear glass respectively. This can be calculated simply by multiplication between coefficient absorption of the glass (α_i) and incoming incident irradiance in the respective side (G_i).

$$\phi_i = \alpha_i \cdot G_i \tag{4.13}$$

4.3 Evaluation of the proposed thermal model

Influence of irradiance and wind speed

Besides the ambient temperature, incoming irradiance and wind speed are the external parameters that influence the temperature of the solar cell. The last parameter is the primary parameter that distinguishes the model calculation proposed in this work with the conventional NOCT model. As depicted in figure 4.2a, the linearity estimation shown by NOCT model despite the variation of wind speed values. The module temperature predicted by finite element model, on the contrary, evolves dynamically as the wind speed value changes.

Figure 4.2b illustrates an example of a numerical calculation of cell temperature using the proposed finite element method in various irradiance and wind speed conditions. Note that the higher the irradiance received by the module, the higher the module temperature will become. Whereas, the impact of wind speed is more pronounced in higher irradiance value as can be seen from the tangent slope of the colored lines in figure 4.2b. The response is getting weaker in lower irradiance and almost negligible when there is no irradiance received by the solar module.

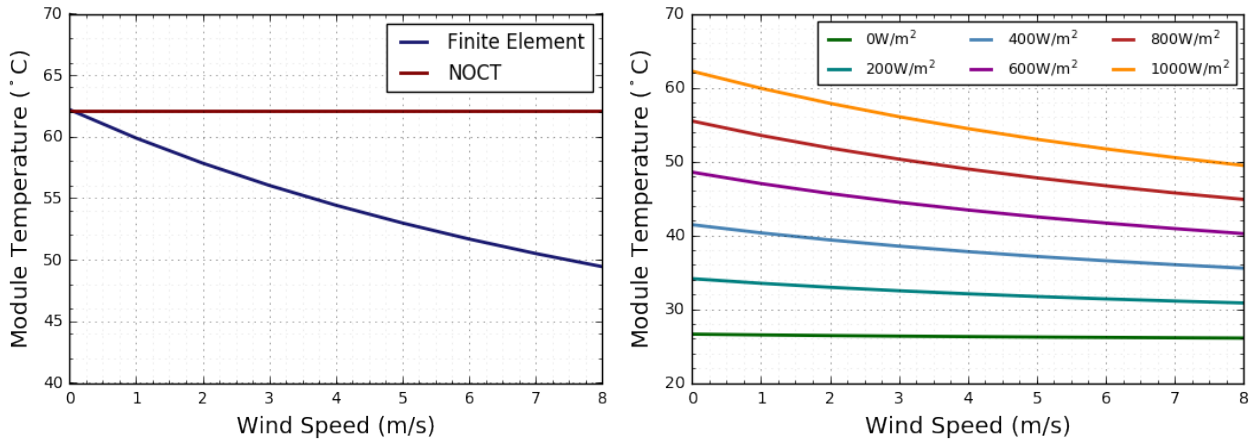

(a) (b)

Figure 4.2: (a) numerical comparisons between NOCT and proposed model at 1000 W/m^2 illumination and (b) module temperature augmentation for different irradiance and wind speed values using the proposed model (finite element method). Both simulations are undertaken at 25 °C ambient temperature condition.

Application for bifacial PVNB

Figure 4.3 illustrate the daily temperature profile calculation using the model when being applied for a bifacial PVNB application. The bifacial PV module is set to face west and tilted 75°. The module used in this simulation is a mono-crystalline bifacial module sandwiched between 8 mm thick glasses. This simulations that shown in figure 4.3 was intended to show the concept of three different nodes of glass-PV-glass module that is used in the thermal model.

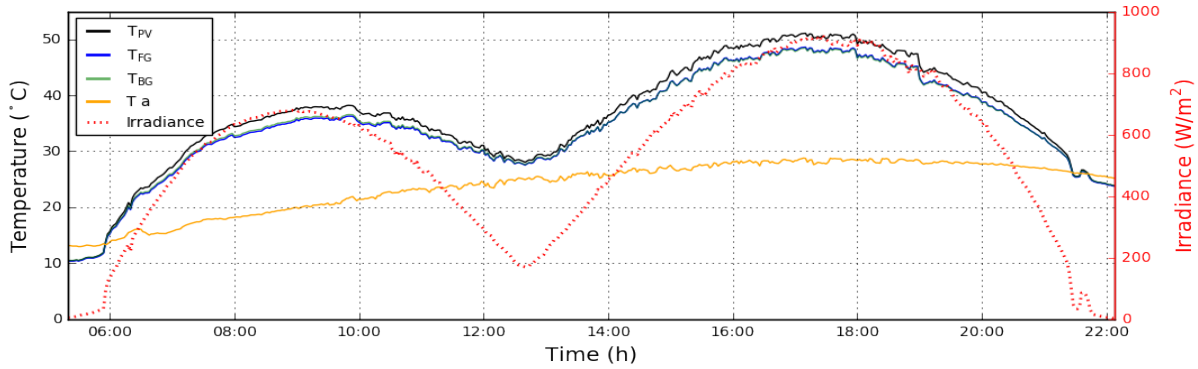

Figure 4.3: Simulated daily temperature profile of bifacial PV module on a sunny day. The right vertical axis shows the incident irradiance values received by the module, as represented by green dotted line. Note the temperature difference between solar cell (black line) and the glasses (blue and green line.)

First of all, it is visible from figure 4.3 that the shape of the temperature profile is strongly influenced by the incident irradiance pattern. Figure 4.3 also reveals that there is a gradual increased of the temperature gap between the solar cell and the front/rear glass when higher solar irradiance is available in the morning and afternoon which can be as high as 3°C. From this, it is clear that PV cell and glass differ in responding the heat exchange due to the difference in physical attributes. However, the temperature between these three elements are almost identical during low irradiance conditions as illustrated during early morning and late afternoon.

Finally, the thermal model that purposely developed for glass-glass bifacial module here is justified to adequately estimate the cell temperature by taking into account numerous aspect

of the system environment. The parameters involved in the model are modifiable and therefore it is possible to be used for any other similar PV configuration. This model, along with the incident irradiance model will be used further in the electrical model explained in the next chapter.

CHAPTER 5

Bifacial PV module energy yield using physically-based model

As was emphasized in research questions (section 1.4), to quantify the shading losses and to provide the mitigation strategies are among the objectives of this thesis. In order to do so, a detailed electrical model that can match the cell-level resolution of irradiance model is required. The goal of this chapter is to develop a detailed yield model that is able to simulate the electrical response of bifacial module under partial shading and inhomogeneous irradiance distribution. The model is based on a physical model that also consider the number of bypass diodes and its connection within the module.

First, the concept of the electrical model together with the simulation technique are explained in section 5.1. It is followed by the validation of the proposed electrical model in section 5.2 with the real measurement data obtained from the SONOB living lab.

5.1 Modelling IV Curve of bifacial solar cell

There are two common approaches to model the electrical output of solar cells: Empirical model that used the efficiency correction and physically-based model that employs circuit equivalent based on physical components. These methods are distinguished by its output. Where the empirical model only generates the maximum power output value and on the other hand, the physical model is able to yield a full I-V curve (parametric continuous).

The empirical model has a limitation to be only used for module level and unworkable to incorporate the cell architecture parameters of a specific module. Whereas, the physically-based electrical model is able to simulate a multilevel I-V curve, from cell to PV module and to PV array level. Due to the necessity to model the electrical mismatch caused by inhomogeneity of irradiance distribution in the PV module, (explained in chapter 2) the second method is employed in this thesis.

There are several circuit simulation software that can be used to compute the full I-V curve based on this physical model, for instance PSpice, PC1D, and QUCS as performed in [19, 31, 60]. These softwares, however, are computationally-expensive and require great effort (in terms of time to learn) to be applied for another specific PV module with different technology and module inter-circuitry design. Due to this reason, full python-based scripts based on numerical iterative algorithms are deployed in this work.

First, the equations and fundamental theory of the physically-based model is explained in

section 5.1.1. Then the section 5.1.2 outlines the implementation of the equations in the PV yield model.

5.1.1 Physical models - Two diodes Equivalent circuit

This section follows up the fundamental theory of two-diodes model explained in section 2.1.2 (please refer to figure 2.2 for the equivalent circuit illustration). The following equation defines the output current of the cell for a given voltage point (V_i). This equation essentially be used to determine the current point along the full I-V curve response.

$$I = f(V_i) = I_{ph,f} + I_{ph,r} - I_{D1} - I_{D2} - \left(\frac{V_i + IR_s}{R_{sh}}\right) \tag{5.1}$$

Next, the list of equations to solve the main equation 5.1 are briefly explained.

Photo-generated current(I_{ph})

Essentially, the photo-generated current (I_{ph}) is a function of irradiance and temperature. This parameter can be calculated by using the following equations

$$I_{ph} = I_{ph.STC} \cdot \frac{G}{G_{STC}} \cdot (1 + K_I \cdot \Delta T) \tag{5.2}$$

Where ($I_{ph.STC}$) is the photo-generated current in short circuit current condition ($I_{sc.STC}$). By considering this condition, equation 5.1 can be rearranged by letting $V_c = 0$ and $I = I_{SC.STC}$ resulting equation 5.3. In equation 5.3, the last two terms are found to be very small and hence negligible so the equation can be simplified as in equation 5.4 [26].

$$I_{ph.STC} = \frac{I_{sc.STC}(R_s + R_{sh})}{R_{sh}} + I_{o1}\left[e^{\left(\frac{I_{SC.STC}\cdot R_s}{n_1 \cdot V_{th}}\right)} - 1\right] + I_{o2}\left[e^{\left(\frac{I_{SC.STC}\cdot R_s}{n_2 \cdot V_{th}}\right)} - 1\right] \tag{5.3}$$

$$I_{ph.STC} \approx \frac{I_{sc.STC}(R_s + R_{sh})}{R_{sh}} \tag{5.4}$$

Term I_{ph} can be either solved by calculating the $I_{ph,f}$ and $I_{ph,r}$ separately or by utilizing the bifaciality factor f_B that was previously explained in section 2.1.2. By reworking equation 5.5 in conjunction with equation 2.2, the total photo-generated current of the bifacial solar cell is given as follows[1]:

$$\begin{cases} I_{ph,total} = I_{ph,f} + I_{ph,r} \\ f_B = \frac{I_{sc,rear}}{I_{sc,front}} \\ I_{ph,total} = \frac{I_{sc,f.STC}(R_s+R_{sh})}{R_{sh}} \frac{G_f + G_r \cdot f_B}{G_{STC}} \cdot (1 + K_I \cdot \Delta T) \end{cases} \tag{5.5}$$

Diode saturation current (I_D) and diode ideality factor (n)

I_{D1} and I_{D2} are the representatives of the current flowing through diodes in the equivalent circuit which can be determined by using equation 5.6. In equation 5.6, the reverse saturation

[1] Note that this solution is under assumption that R_s and R_sh between front and rear side are exactly the same.

currents, and thermal voltages are represented by I_{o1}, I_{o2}, and V_{th} respectively. Where, n_1 and n_2 are the ideality factors of the two corresponding diodes.

$$\begin{cases} I_{D1} = I_{o1}\left[exp\left(\frac{V_i+IR_s}{n_1 \cdot V_{th}}\right) - 1\right] \\ I_{D2} = I_{o2}\left[exp\left(\frac{V_i+IR_s}{n_2 \cdot V_{th}}\right) - 1\right] \end{cases} \tag{5.6}$$

Where the thermal voltage V_{th} can be calculated using following equation:

$$V_{th} = \frac{k \cdot T}{q} \tag{5.7}$$

Then, the general expression of saturation current as the function of the band-gap of semiconductor material and temperature is expressed in equation 5.8.

$$I_o = I_{o.STC} \cdot \left(\frac{T}{T_{STC}}\right)^3 \cdot exp\left[\frac{q \cdot E_g}{k_B}\left(\frac{1}{T_{STC}} - \frac{1}{T}\right)\right] \tag{5.8}$$

Where E_G represents band-gap of the semiconductor material with $E_G = 1.12EV$ for a silicon absorber. This term can be evaluated by using empirical equation 5.9. Saturation current equation at STC can be derived from equation 5.1 by reformulating equation 5.6.

$$E_g = E_{g.STC} \cdot [1 - 0.0002677(T - T_{STC})] \tag{5.9}$$

$$I_{o.STC} = \frac{I_{sc.STC}(R_s + R_{sh}) - V_{oc}}{R_{sh} \cdot \left[exp\left(\frac{V_{oc}}{n_1 \cdot V_{th}}\right) + exp\left(\frac{V_{oc}}{n_2 \cdot V_{th}}\right)\right]} \tag{5.10}$$

To represent the influence of additional recombination happening in the p-n junction that affect the fill factor (FF) of the I-V curve, this non ideal diode behavior is often represented by an ideal diode (D_1) that has ideality factor (n_1) equal to one and non-ideal diode (D_2) which have ideality factor greater than one (n_2) [22]. The second ideality factor (n_2) value can be retrieved by fitting parameter to the actual I-V measurement. In this work, however, the diode ideality factors are assumed as $n_1 = 1$ and $n_2 = 2$ as also used in [26]. Though this assumption may lead to a slight overestimation in the knee of I-V curve, the final I-V curve result is still reasonably accurate as shown in [33].

Series and shunt resistances (R_s & R_{sh})

R_s and R_{sh} values almost never explicitly provided in the PV module datasheet. Hence, fitting I-V curve procedure through iteration is required. One way to do this is by varying R_s and R_{sh} independently until the I-V curve fits the experimental data. However, the result found by this method often failed to match the experimental I-V curve, particularly in the maximum power point region (P_{mp}) [26]. More accurate solution to extract these values is by iteratively incrementing R_s value while simultaneously calculating R_{sh} and set P_{mp} as the boundary condition. This is done by reworking the main equation 5.1 under the maximum power point condition (P_{mp}) and rewritten as in equation 5.11. This equation implies there will be a pair of R_s and R_{sh} that makes the calculated I-V curve cross the experimental maximum power point (V_{mp} I_{mp}).

$$R_{sh} = \frac{V_{mp.STC}(V_{mp.STC} + I_{mp.STC}R_s)}{V_{mp.STC}(I_{ph} - I_{D1} - I_{D2}) - P_{mp}} \tag{5.11}$$

Finally, the analytical solution to solve the iteration in [61] is implemented in this thesis. Full scheme of the algorithm can be found in the reference [61].

5.1.2 Simulation technique

Solving two-diodes equations

The flowchart in Figure 5.1 describes the algorithm to obtain a continuous I-V curve under a given irradiance (G) and temperature (T) condition. Further, the two-diode formula in equation 5.1 need to be solved repetitively by replacing the voltage value from $V_c = 0$ (short circuit current) to $V_c = V_{OC}(G,T)$ (open circuit voltage). The following equation is employed to obtain the $V_{OC}(G,T)$ boundary for a specific G and T condition which need to be determined prior the iteration.

$$V_{OC}(G,T) = V_{th} \cdot log(\frac{I_{ph}}{I_o}) \tag{5.12}$$

Moreover, the set of equations described in section 5.1.1 is rather complex and cannot be rearranged to directly solve I. Also, using an ordinary iterative method can be time-consuming due to a large number of iteration [26]. To boost the computation performance, such as Lambert W function or Newton-Raphson numerical methods are often exploited [26]. In this thesis, an iterative optimization algorithms by Suckow et.al is implemented [33]. This algorithm is based on a combination of Bisection and Newton-Raphson method in root finding routine. Refer to [33] and citation therein for the full algorithms explanation.

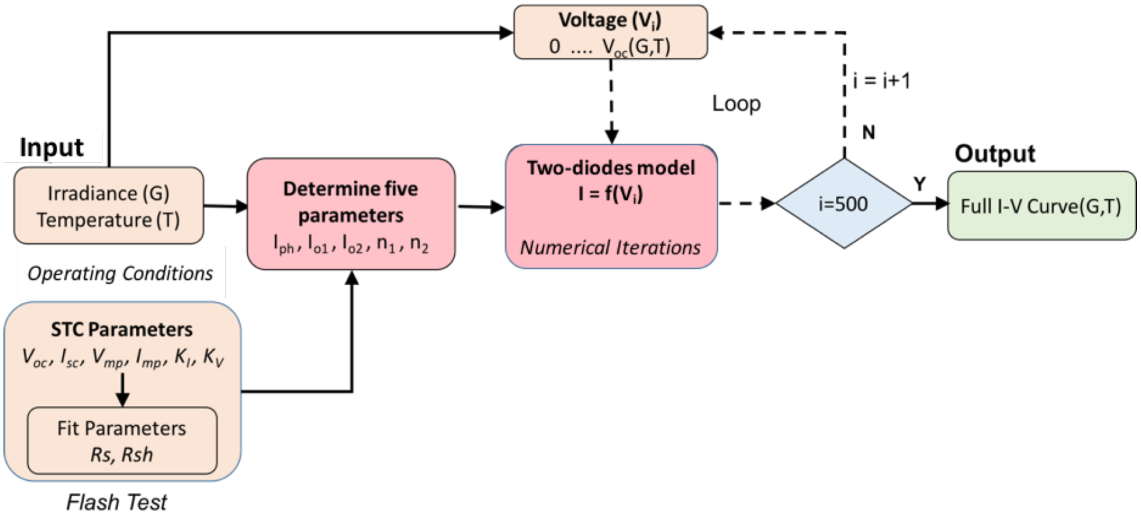

Figure 5.1: The algorithm developed in this thesis to solve the two-diode model equations. Note that the I-V curve can be fully created after 500 times calculation steps.

Cell to Module I-V curve

The previous equations are originally assigned for a single solar cell. However, this also scalable to a higher granularity level, for instance, to a substring level[2], module level, or even PV array scale. The hierarchical of this multi-level solar cell architecture is visually presented in figure 5.2. In order to get a correct electrical response of a certain PV system level with N_s cells in series and N_p cells in parallel, scaling factors needs to be applied for the corresponding parameters as described in the following equations (5.13-5.16) [62].

$$I_{system} = N_{parallel} \cdot I_{cell} \tag{5.13}$$

[2] a group of cell that shares the same bypass diodes connection in the module. Also see figure 5.2 for the illustration.

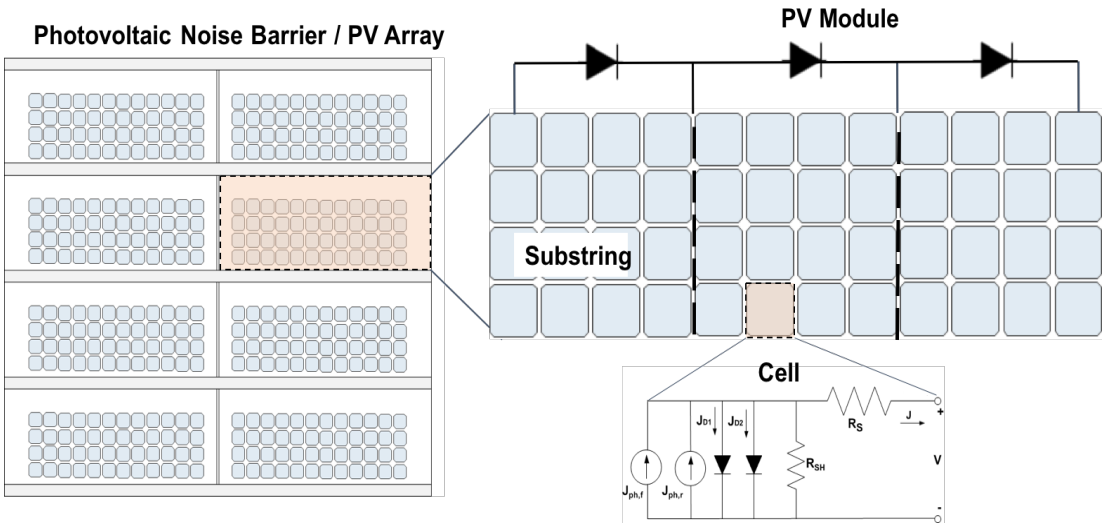

Figure 5.2: PV module layout breakdown from array level to cell level. In this example, 48 cells are connected in series forming a string in the module. The PV module has three bypass diodes protection in which group of 16 cells (substring) are connected to one bypass diode.

$$V_{system} = N_{series} \cdot V_{cell} \tag{5.14}$$

$$R_{s.system} = \frac{N_{series}}{N_{parallel}} \cdot R_s \tag{5.15}$$

$$R_{sh.system} = \frac{N_{series}}{N_{parallel}} \cdot R_{sh} \tag{5.16}$$

To obtain the module I-V curve, the substring division procedure as introduced in [63] is deployed in this thesis. This procedure proposed by first escalate the cell IV curve into substring level by using scalability concept in equation (5.13 - 5.16). This based on the approximation that the current output of a substring in the module is limited by the lowest current cell (in other words that receive the lowest irradiance). While the voltage across the substring is equal to the addition of cell voltage which shares the same bypass diode. Instead of constructing the module IV curve from individual cell IV curve, this procedure is found to be more efficient and greatly enhance the speed of computation.

To ensure the alignment of optical, thermal and electrical models, this concept was adapted in the python scripts by first calculating the total irradiance distribution on each cell (the sum of front side and rear side) using the procedure explained in chapter 3. Then, the sorting process to determine the cell that received the lowest irradiance in each substring is performed. Afterward, the cell temperature is calculated on a substring level by using the representative substring irradiance. These irradiance and temperature pairs then become the input for substring I-V creation. Note that by using this procedure, various bypass diodes configurations can be efficiently modeled by firstly grouping the cells in the same bypass diodes interconnection, which is reasonably faster than creates the I-V curves per each cell.

Finally, the module I-V curve is acquired by summing up individual substrings voltages that correspond to their current output. To exemplify, the construction of this procedure is illustrated in figure 5.4. In this figure, the example of module I-V curve that consists of three substrings is presented. It can be noticed that each substrings has different current output level which represents the uniformity irradiance distribution in the module. In real life, this condition most of the case happened due to the partial shade in the module. In the end, the DC output can

be determined from the maximum power point in the module I-V curve for the given time step simulation.

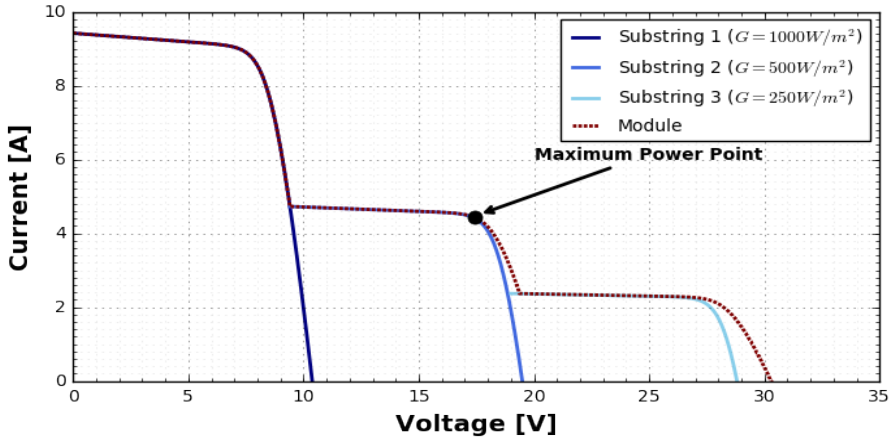

Figure 5.3: Module IV curve constructed from three substrings under different illumination levels that assumed as the effective irradiance reaching both front and rear surface of the module. The temperature is assumed to be 25^{o}C. The parameters used in this IV curve is using the bifacial module in the SONOB project that will be explained later in section 5.2.2.

5.1.3 Electrical performance under different substring configuration

As emphasized in section 1.4, this thesis has put a strong interest in mitigating self-shading condition that unavoidably occur in bifacial noise barrier integration. One way to do this is by designing different substring layout in the module, for instance, by connecting them vertically or horizontally depending on the most frequent shading pattern that fell on the module. Additionally, the better electrical performance is expected when the number of bypass diodes within the module is increased. Figure 5.4 shows six different bypass diodes layout interconnection scenarios opted for mitigation strategies study in section 6.3. Besides the vertical and horizontal layout, a smart module interconnection which denotes as "L-shaped" scenario is also analyzed. The L-shaped configuration was derived based on the similar shading pattern that found in the PVNB application (see figure 3.16).

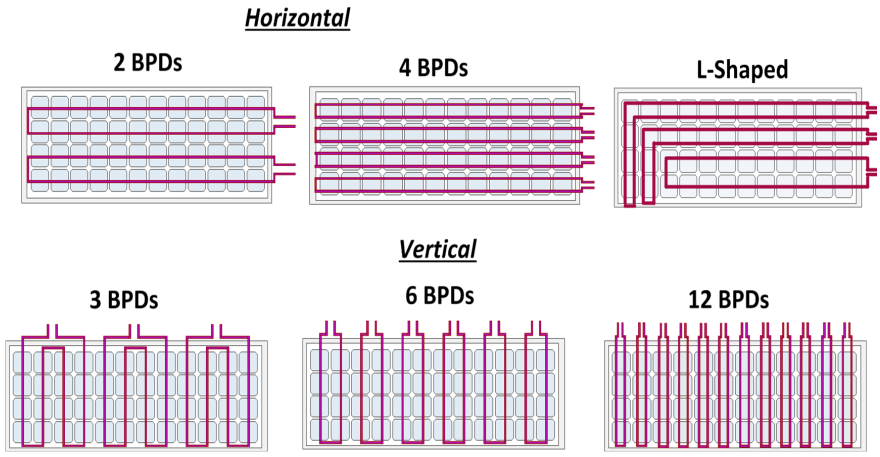

Figure 5.4: Different substring layout scenarios opted in shading mitigation study in section 6.3. The electrical response for each six bypass diodes configurations can be modeled by using the approach explained in section 5.1.2.

Nevertheless, the benefit for these approaches cannot be predicted intuitively just by looking at one partial shade condition. Merely with a complete yield simulation over annual period

the representative potential benefit can be evaluated. The application of this concept will be explained as one of the simulation scenario in the section 6.3.

5.1.4 Key Performance Indicators

The performance evaluation in the following chapter 6 is primarily based on annual energy calculation yields by the individual module (E_{DC}^{annual}). This can be determined by integrating the DC output power (P_{DC}) over the interest period, in this case on an annual basis.

$$E_{DC}^{annual} = \int_{annual} P_{DC}(t)\, dt \tag{5.17}$$

In general, the performance of a PV module or a system (E_{yield}) needs to be normalized either using its surface photo-active surface area (kWh/m^2) or using its rated power (kWh/kWp). In this thesis, the second term is used as the main indicator comparison.

$$E_{yield} = E_{DC}^{annual}/E_{DC\,rated}^{annual} \tag{5.18}$$

Lastly, the quantification of shading losses (SL) can be defined in percentage using equation 5.19. This means the yield simulation needs to be performed in both unshaded and shaded scenarios.

$$SL = (E_{yield}^{unshaded} - E_{yield}^{shaded})/E_{yield}^{unshaded} \tag{5.19}$$

5.2 Model Validation with outdoor measurement

The validation was conducted by comparing the simulation result with data measured in the SONOB project test, the Netherlands [11]. The so-called SONOB (Solar Noise Barriers) living lab was located on Randweg Den Bosch, the Netherlands (51.69^{o}N, 5.30^{o}E). The validation of the model will be examined by using the west facing module in which the self-shading cast by the rear side structure happened (see figure 2.4).

5.2.1 Module used in the experiment

In this field test, 48 bifacial n-type silicon solar cells from NSP [64] are connected in series to form a module in each noise barrier. The module is divided into six vertical substrings (8 cells each) that represents the six bypass diodes inclusion in the module.

Electrical parameters for the evaluated bifacial PV module were extracted from the I-V curve measurement for each front and rear sides under the standard testing condition as shown in table 5.1. Whereas, the procedure explained in section 5.1 was used to derive the resistances values. The bifaciality of the module found to be 93% from the ratio of $I_{SC\,r}/I_{SC\,f}$. The comparison illustration of modeled I-V curve with I-V flash data measurement (STC condition) is given in figure 5.5.

In figure 5.5, the noisy I-V curves which can be observed from the measurement data are probably occurred due to the measurement technique problem that used by the module manufacturer. Despite the slight fluctuation of the I-V curve, the most important parameters have been accurately predicted by the electrical model. For instance, and the most important parameter, is the maximum power point which is shown by the orange dots in the figure.

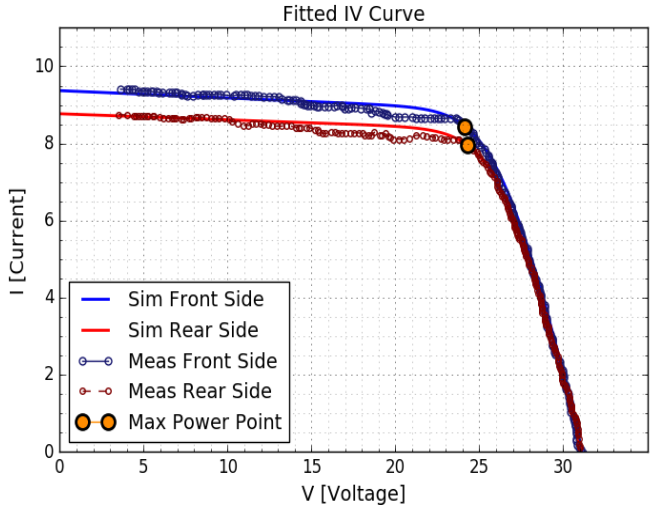

Figure 5.5: Fitted I-V curve of the PV module. The measurement data were reproduced from flash data.

5.2.2 Experimental Setup

The SONOB living lab was equipped with a sufficient set of measurement instruments that enable the performance analysis of the installed PV modules. The plane of array irradiance (G_{POA}) for two sides direction of barriers were measured using EKO MS-802 secondary standard pyranometer which mounted on top of the barriers [65]. Another pyranometer was installed above the container to measure the global horizontal irradiance (GHI). This GHI measurement is primarily used to calculate the clearness index on the site which can be derived from the ratio of the horizontal global irradiance (GHI) to the extraterrestrial irradiance (G_O). In addition, a dedicated weather station was installed to record the ambient temperature and wind speed in the location.

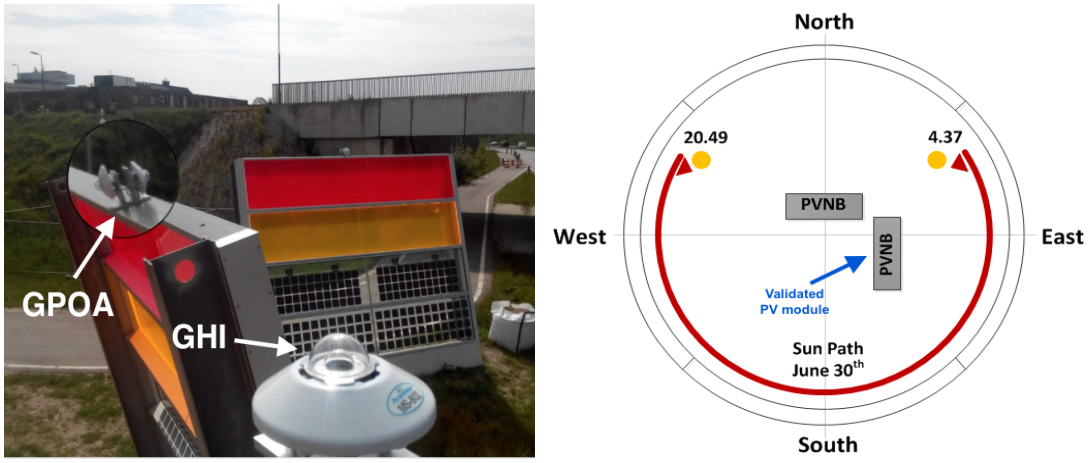

(a) Experiment setup in SONOB living lab

(b) Sun path illustration

Figure 5.6: Figure (a) shows the closer look to the location of pyranometer installation. Figure (b) gives an illustration of typical sun path in the Netherlands during summer time.

Eko instrument MP-160-IV Curve Tracer was installed to measure the I-V response of the evaluated modules. A 4-wire measurement[3] setup was implemented in the connection between the PV modules and I-V tracer to minimize the error caused by the lead resistance. However, the

[3]By using separate pairs of current voltage-sensing electrode.

IV-tracing device still has 0.5% level of uncertainty for both voltage and current measurement [66]. Furthermore, this I-V tracer also logged another the data on the measurement including the data from pyranometer. Whereas the weather station was plug into a separate computer. The data acquisition was performed every two minutes which can be considered as high-resolution data for PV system performance analysis.

5.2.3 Model setup

The yield model that has been explained in section 5.1 was used to estimate the DC power output of bifacial module. The module temperature calculation was done by means of the model explained in chapter 4.1, using the ambient temperature and windspeed data collected by the weather station data on-site. Whereas, the global horizontal irradiance data measured on-site was used as input for the Reindl-2 separation model [67]. This model is able to uncouple the direct irradiance and diffuse irradiance[4] from the measured plane of array irradiance that reaches both front side (west) and rear side (east). Then the reduction of direct irradiance part due to self-shading can be corrected by using the shading model explained in section 3.2.

(a) **(b)**

Figure 5.7: Comparison of SONOB Living Lab used for validation (a) Real condition [21] (b) Rendering of 3-D Drawing made in Sketchup. All the components and dimensions used in the 3-D model are exactly followed the real aspect given in the original technical drawing.

To perform the shading calculation, the 3D model is "realistically" drawn within the SketchUp environment. The comparison between the drawing and real condition is depicted in figure 5.7. Although only the east-west facing noise barrier that will be used for the validation, the north-south facing barrier need to be modeled accurately as well. This is due to the observation that the north-south barrier cast a shadow to the front surface of east-west facing barrier hence a partial shading condition have to be taken into account in the model.

5.2.4 Validation Results

DC yield validation

Figure 5.8 shows the comparison between the output DC power predicted by the model in blue line and the measured data that is represented in red line. The model had been compared in three different weather conditions in order to analyze the accuracy in the corresponding situations. The monthly validation is also showed to further justify the accuracy of the model as given in figure 5.9.

[4] This includes the ground diffuse irradiance or known as reflected irradiance

In overall, as shown in figure 5.8, the output power predicted by the model are remarkably aligned with the measured data as the blue line correctly overlay the red line throughout the day. The average deviation is very small with 1.4% and 3.5% during the overcast and partly cloudy day respectively.

Table 5.1: Comparison between modeled and measured data

Condition	*Daily DC Yield Meas*	*Daily DC Yield Sim*	*Error*
Overcast	296.3 Wh	300.59 Wh	-1.4%
Partly Cloudy	1098.1 Wh	1137.4 Wh	-3.5%
Sunny	1486.7 Wh	1485.1 Wh	0.1%

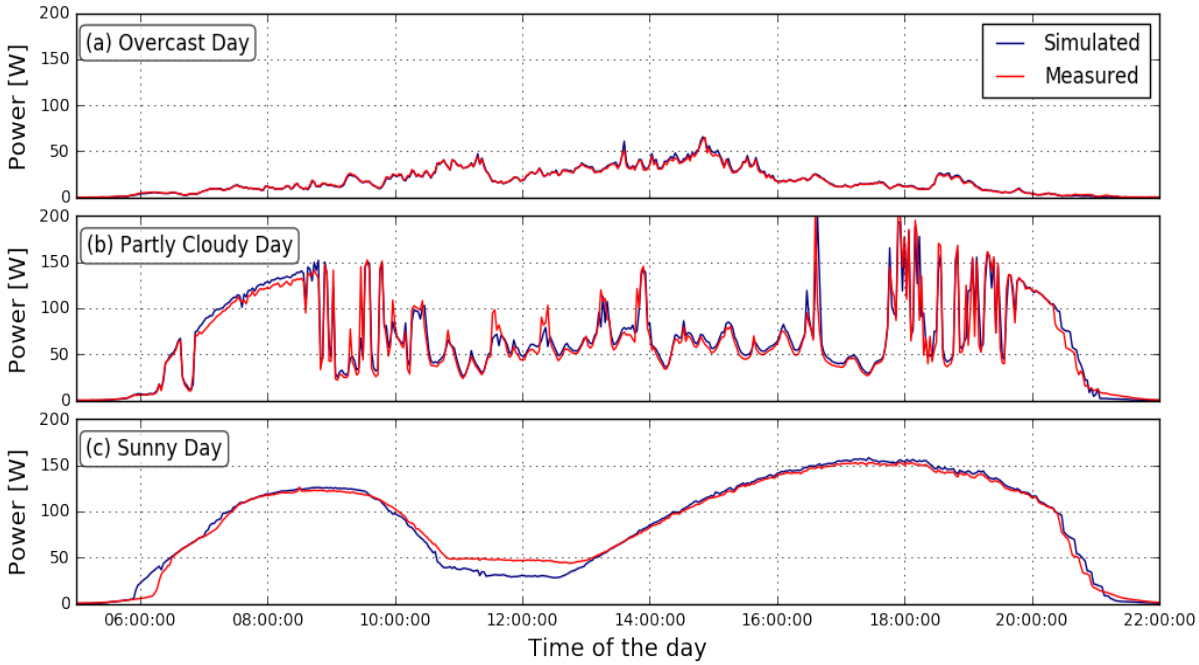

Figure 5.8: Results of yield model validation with SONOB measurement data. 3 representative days are selected (a), overcast day (June 2, 2015)(b), partial cloudy day (June 3, 2015) (c), sunny day (June 30, 2015).

During a sunny day, however, a large deviation can be noticed in early morning (6 AM) and during noon time (12 AM). Firstly, the slight shift in the early morning is due to the blocking of the irradiance by the bridge behind the observed noise barrier (see figure 5.6a). As can be seen in Figure 5.7b, the bridge was not incorporated in the model and hence will induce deviation. In the second condition during solar noon, a possible reason that caused the deviation was because of the cosine effect measurement[5] by the plane of array pyranometers. This measurement error typically ranging between 2% - 6% [68]. It should be noted that these pyranometers are facing weast-east and nearly vertical. Hence, during solar noon in the summer time, when the sun transits from south east to south west, the incident angle between the sun and pyranometers was close to 90^o. Nevertheless, these two effects are less noticeable during cloudy condition.

To further measure the accuracy of the model, the result of one month full simulation result was performed as shown in figure 5.9. A linear relation is obtained by the monthly model validation

[5]Synonymous to Lambertian cosine law that implies the reduction of radiation intensity as the cosine angle between the light source and receiver increases to 90^o .

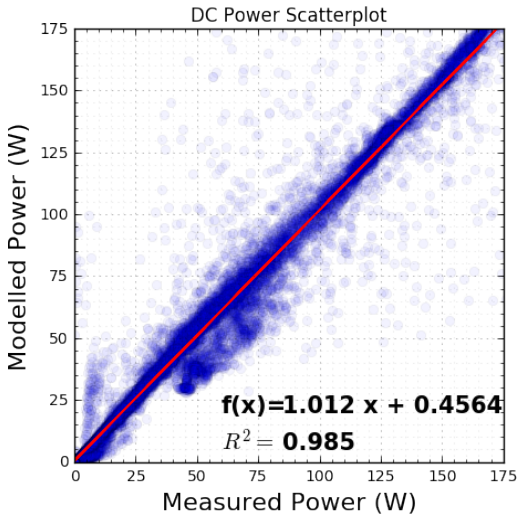

Figure 5.9: Monthly validation result of model against the measured data.

with fit function $f(x)$ nearly as one. The artifact data[6] in the graph accounts a fairly small percentage with only 0.62% from total monthly data. The reason is because of the delay of the I-V tracer in reading the irradiance and I-V curves of the bifacial module and generates large deviation when instantaneous change in irradiance is happened. This happened due to the technical condition that the irradiance sensors were inputted in the first five channels of I-V tracers while the I-V curves measurement of bifacial module were connected in the few last channels in the I-V tracers. It took almost one minute for I-V tracer to log all the data from the first channel into the last channel.

IV Curve under partial shading validation

To be able to see the accuracy of the I-V curve model in responding the partial shade condition, the result of I-V curve is compared with the site measurement. The validation was done by comparing two different instantaneous times on a sunny day (June 30, 2015) which is similar with the sunny day that has been compared in figure 5.8. The shading patterns with the corresponding I-V curve results of these comparisons are shown in figure 5.10. It can be seen that the comparison was done by looking into the performance under vertical and horizontal shading on the rear side of the module. To prove the influence of bypass diode configuration (denotes as bpds), aside from the 6 bypass diodes configuration that represented the real condition of the compared module, the simulation under unshaded condition and 3 bypass diodes configuration were added in dashed lines as references.

In overall, the good agreement are shown between simulation results and the measurement in both conditions shown by the matching shape between the blue solid line (simulation) and red solid line (measurement). Looking at the first condition in figure 5.10c, the importance of the implementation of bypass diodes configuration is noticeable from the failure of green dashed line in predicting the I-V curve measurement. In this case, due to the different of cells in one substring (3 bypass diodes = 16 cells), the voltage drop was higher than in 6 bypass diodes case (6 bypass diodes = 8 cells) and hence predicting a lower yield with respect to the measured power.

In the second graph (figure 5.10d), again, the model is able to predict the power output in other partial shading shape condition. In this part, the sun position is relatively high already and as

[6]Data point that has deviation more than 100%. Note that no filtering data was applied in this comparison.

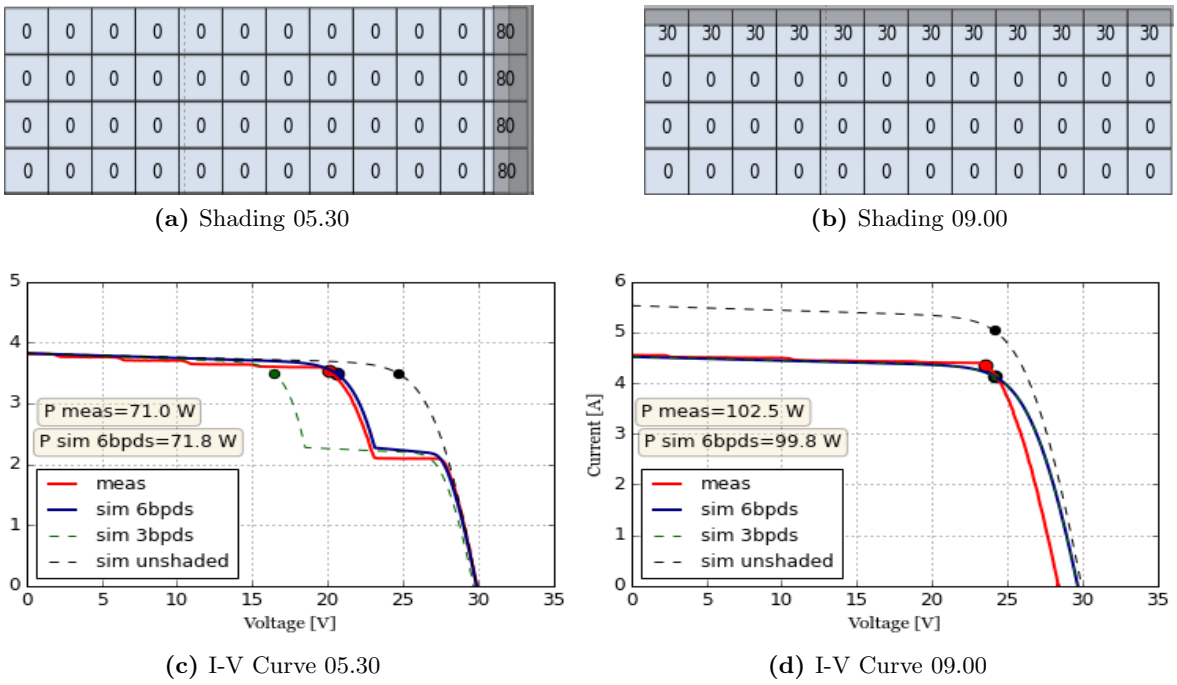

(a) Shading 05.30

(b) Shading 09.00

(c) I-V Curve 05.30

(d) I-V Curve 09.00

Figure 5.10: Figure (a) and (b) show the simulated shading pattern produced on a sunny day(June 30, 2015) at 5.30 AM and 09.00 AM respectively. While figure (c) and (d) represent the I-V curve validation of each corresponding time. Note that the actual module configuration is consisted of 6 bypass diodes (bpds) connected in vertical layout. The unshaded condition and 3 bypass diodes configuration are also simulated and given in the figure to show the accuracy of the model by using a correct configuration.

a result, the shade cast by the top structure forms a horizontal shape shadow. Consequently, reduction of current was found in each substring and can be obviously seen by the proportional current shift from about 5.5 A (unshaded condition) to 4.5 A (partial shade condition). Though the power output is predicted very well by the model, there is a slight misalignment in the I-V curve as can be noticed from the voltage value near V_{OC}. This is most likely caused by the voltage drop due to the activation of 6 bypass diodes which is not incorporated in the model. This effect is not obvious for the first case, since only one bypass diode that was triggered to be activated. A second possible reason is due to the lower temperature predicted by the thermal modeled compared to the real condition, resulting the mismatch in V_{OC}. Unfortunately, the actual temperature was not measured and hence very difficult to do further justification.

Conclusion of electrical model

The development of electrical model based on physical approach of bifacial solar cell was presented in this chapter. The model was built upon the two diodes model that has two current sources that represent the contribution of front and rear illumination. The model was fully created in python programming environment that offers flexibility to simulate the electrical response under different bypass diodes configurations. This feature is very important for shade mitigation study in this thesis.

The accuracy of the model was validated against the measurement data from SONOB living lab project. It was shown that the model is able to accurately predict the output power of bifacial modules under different weather conditions. A linear relation between modeled and measured data was also shown in monthly comparison. Furthermore, the I-V curves validation result proved the importance of coupling the shading model with a proper bypass diodes configuration in the electrical model. It was shown that the deviation can be as high as 28.5% if the shading is not incorporated into the irradiance model. The observation from the I-V curve validation step also suggested a possible model improvement to include the forward voltage drop caused by the activation of bypass diodes during partial shading condition.

In overall, these validation results demonstrate that the developed model can successfully met the goal of this chapter to develop an accurate model that can predict the electrical response of bifacial PV module under partial shading condition. This justify the reliability of the model and gives the confidence to be implemented for further analysis of yield simulation of bifacial PVNB under different scenarios in the following chapter.

CHAPTER 6

Results

In this chapter, the models that have been previously developed and validated are used as tools to perform yield simulation of bifacial PVNB. The goal of this chapter is to answer the research questions in section 1.4, in which to investigate the yield performance of bifacial PVNB under different parameters, that can eventually be used as a guideline in designing bifacial PVNB.

Table 6.1 lists the conditions that are used as the reference parameters of simulation study. The PVNB design defined in section 2.2 is used as the study case reference. The performance of eight different PVNB orientations, as listed in table 6.1, are considered in every simulation when other parameters are being varied.

Table 6.1: Reference simulation parameters

Parameters	**Reference condition**
Tilt Angle	75^o
Albedo	0.2
Bypass diodes	3
Cell Positioning	Standard
Location	Den Bosch, the Netherlands
Orientations	North, South, East, West, NE, NW, SE, SW

The other optimization scenarios used in this simulation are listed in Table 6.2. The simulations are performed by varying one parameter condition while keep the other parameters in table 6.1 constant. The obtained results will be shown in the subsequent chapter and will be followed by result discussion in section 6.6.

Table 6.2: Simulation Scenarios

Parameters	**Other scenarios**
Tilt Angle	80^o, 85^o, 90^o
Albedo	0.35, 0.5
Bypass diodes	2(H), 4(H), 6(V), 12(V), 3(L-shaped)
Cell Positioning	Broad, Narrow
Location*	Reykjavik, Dubai, Jakarta, Melbourne

*Perform in 4 different tilt angle scenarios.

Simulation conventions

Before going any further it is important to understand the naming conventions used throughout all the simulations. First of all, it should be emphasized here that all orientation notation represents the azimuth of the front side of the bifacial module. It should be remembered that the rear side is always in the opposite direction of the front side module. This is very important since most of the analysis of the shading and shadow ground phenomena are related to the rear side of the bifacial module.

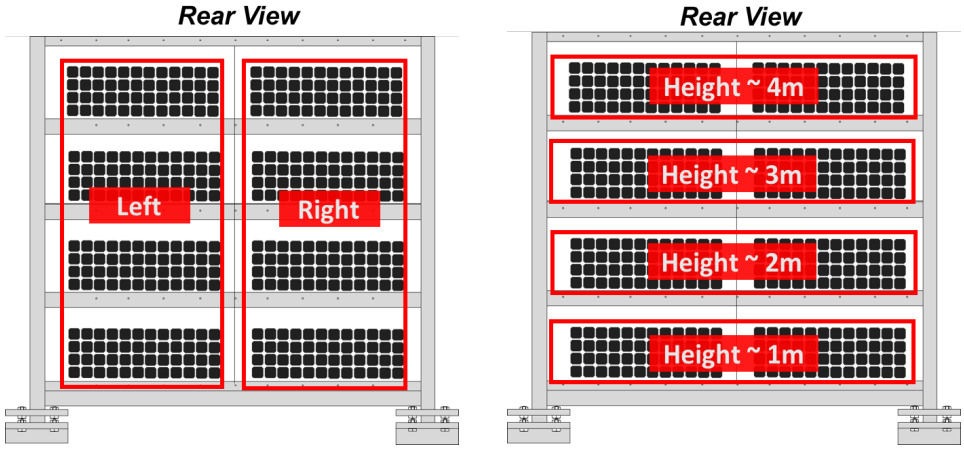

(a) (b)

Figure 6.1: Figure (a) illustrates a group of four modules in the same column : left and right. Figure (b) shows a group of two modules in the same row.

The simulations are performed simultaneously for eight bifacial modules in noise barrier. However, the result of each panel is not presented separately but rather by the averaged value over a group of module as illustrated in figure 6.1. In section 6.1 and 6.3, the results of annual yield performance is presented as the average of 4 modules in each left and right modules (See figure 6.1a). In section 6.2, averaged value of each row in the same module elevation (2 modules each) is considered (See figure 6.1b). Whereas, the results in section 6.4 and 6.5 use the average over eight modules in the studied PVNB. The results of simulations are mainly revealed through annual specific energy yield (kWh/kWp) and shading loss percentage (%) as explained in section 5.1.4.

Irradiance and shading data

The input of weather and irradiance data are retrieved from Meteonorm database software for each location as was mentioned in Section 3.1. According to IEA PVPS Task 13, PV performance analysis should be performed every 5 to 15 minutes because a longer resolution may hamper the performance analysis of the system [69]. In this work, 10-minutes time step simulation was selected for the overall yield simulation. Figure 6.2 shows the typical annual irradiance profile in Den Bosch that was retrieved from the software.

The shading table for each cell in the eight modules are created prior to the simulation. In this work, the said shading tables were only simulated for the west orientation. The result of other orientations can be obtained by reshaping the data in shading lookup tables according to the desired orientation. To give an example, the overall simulated shading fraction of the left module for three different orientations are illustrated in Figure 6.3. Note that this method can only be applied if the shading objects are the same for each orientation (in this case only PVNB structures).

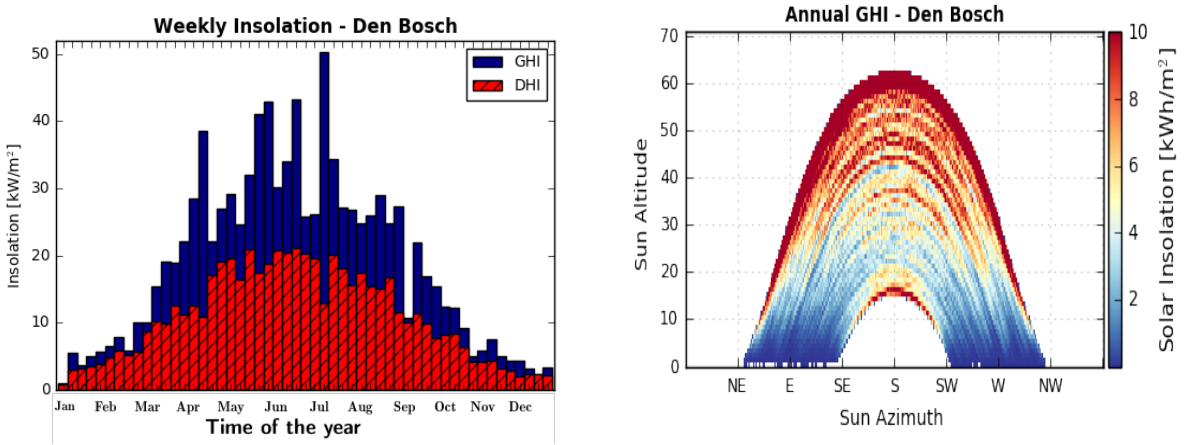

(a) (b)

Figure 6.2: Figure (a) shows weekly solar insolation profile in Den Bosch. Figure (b) depicts a histogram of GHI distribution over a year as a function of solar position. Note the irradiance variation between the summer and winter time.

In figure 6.3, the simulated shading values for each azimuth and altitude pair of one module can be identified by the black color (Shading fraction = 1) that represent the fully shaded condition and white color for the fully unshaded condition (Shading fraction = 0). The superimposed sun path diagram that shown by the orange lines in the graph gives very important information. For example, it can be seen in Figure 6.3a that the module will experience partial shade in early morning at 5 AM and then free from shade until it gets partially shaded again at 9 AM.

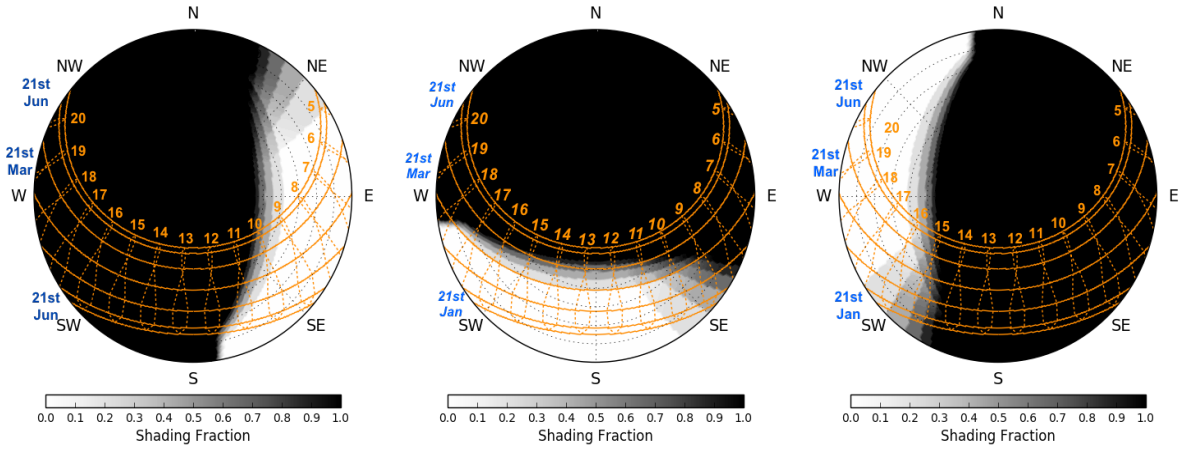

(a) (b) (c)

Figure 6.3: Simulated Shading mask of rear side west facing module (a) in studied PVNB. Where (b) the rear side of the north and (c) east can be obtained by rotating the value of the initial result in figure (a). Orange lines represent position of the sun throughout the year in Den Bosch, the Netherlands. While the numbers in blue show the corresponding diurnal time. Note that the shading fraction values is in module level. Partial shading condition can be identified by the gray area in this graph.

6.1 Different tilt angle

This section investigates the yield performance sensitivity of bifacial PVNB under 4 different tilt angles : 75^o, 80^o, 85^o, 90^o. The simulation is performed for eight different orientation and hence there are 32 combinations in total. The other parameters follow the reference condition as listed in table 6.1. The analysis of daily performance of each orientations will initially be shown.

Daily yield performance

Figure 6.4 illustrates the analysis of daily power output for all module orientations during a sunny summer day of 75^o tilt angle configuration. To improve readability, the information is divided into two graphs. Each figure is assisted with the corresponding shading fraction of the rear surface module.

By looking at figure 6.4a first, it can be seen that the south facing module has similar pattern as the monofacial module that reaches its peak production at solar noon. For bifacial module, additional output power is expected in the early morning and late afternoon as the contribution of direct irradiance reaching the rear side of the module when the sun position in the north east and north west (see figure 6.2). However, the structure blocks the direct irradiance component (see the corresponding shading fraction values of south orientation) and hence the extra output is not significant. Inversely for the north orientation, two bumps are clearly visible in figure 6.4a in the morning and the afternoon when the direct irradiance reaching the front surface (no partial shading occurs on the front side). Furthermore, severe shading losses are experienced by the north orientation which limits the power output most of the day (see corresponding shading factor value and figure A.1). This is because the sun position is rather high during summertime and hence the shadow is casted by the top structures to the rear surface throughout the day.

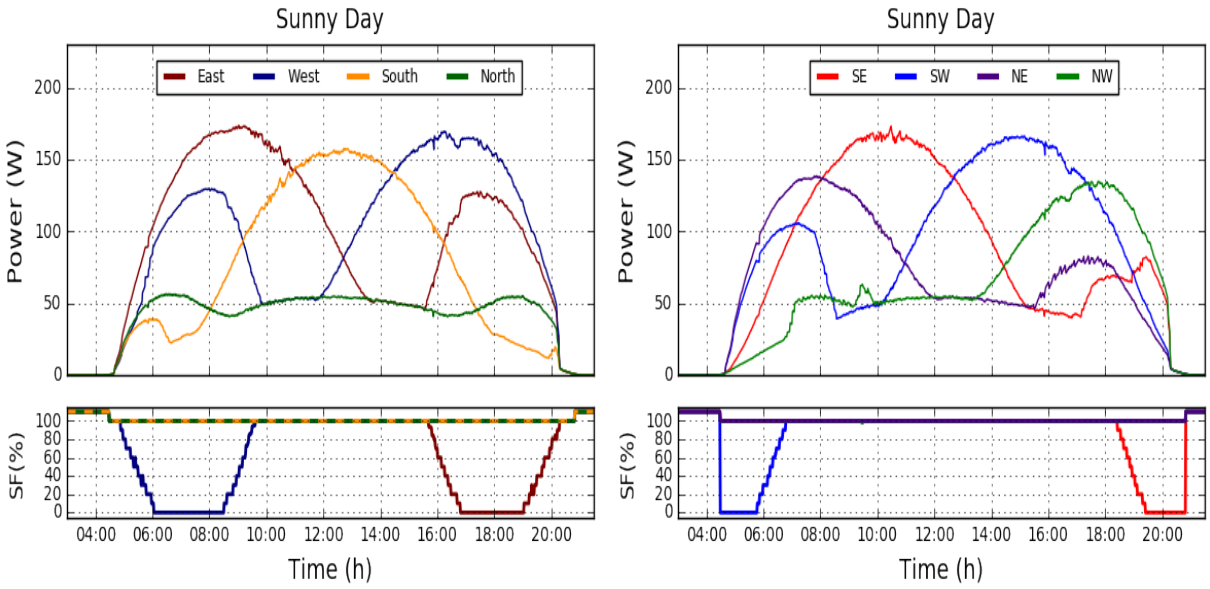

(a) **(b)**

Figure 6.4: Daily power output profile during a sunny day of a 75^o tilt bifacial PVNB (Top figures). Shading factor (SF) values of the rear surface of corresponding orientations are given in the graph beneath it. SF values above 110% indicate the condition when the sun is below the horizon.

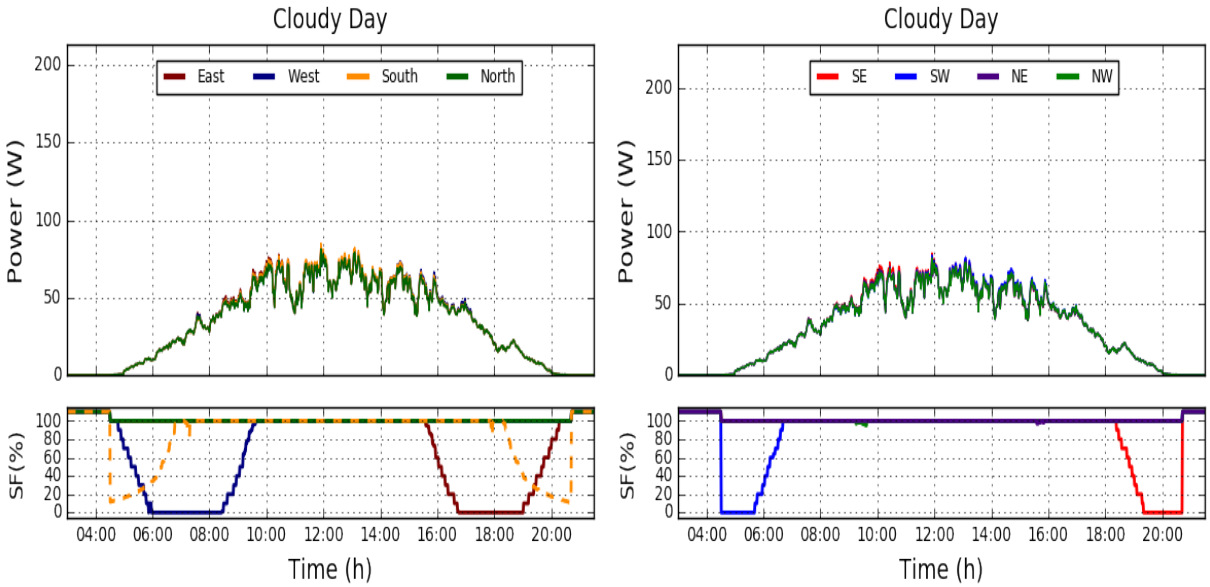

Figure 6.5: Daily power output profile during a cloudy day of a 75^o tilt bifacial PVNB. Note that the power output for all orientations is very similar and shading has no influence at all due to zero direct irradiance during this condition.

Whereas, from the same graph in figure 6.4a, due to its position towards the sun, the west and east facing modules produce peak power in the morning and afternoon respectively. Moreover, the daily profile of power generation by these two orientation are quite symmetrically opposed to each other. In these configurations, partial shade conditions can be observed when the sun position directly faces the rear side of the module. For example, the west facing module suffers the partial shading condition in the early morning and starts completely shaded at 10 AM till the sun is exactly located in the south at midday, and vice versa for east facing modules (Refer to figure A.1 for the illustration).

The typical daily power output profile of four other orientations are given in figure 6.4b. It can be seen that northeast orientation produces more power in the morning, even though it is not as high as the east orientation. Surprisingly, the yield of south west and south east orientation surpass the performance of south facing module. A longer insolation time of the front surface of the module to the sun and relatively lees shading (see the corresponding shading factor) on their rear surface are the possible reasons for this condition.

Finally, the power output profiles during a cloudy condition are given in figure 6.5. The difference of power output between each orientation is very hard to distinguish. This is because only diffuse irradiance available and therefore the shading fraction has no effect on the power output profiles. It implies that the shading loss is highly dependent on the clearness index. Therefore in the case of the Netherlands, a higher shading loss is expected in summer season because more available sunny day compared to the winter season.

Seasonal yield performance

The examination of seasonal performances of the aforementioned PVNB configurations are revealed in figure 6.6. The knowledge of how bifacial PVNB performs throughout the year is very crucial for the full PV system design. In figure 6.6 each block represents the corresponding orientation and the monthly energy yield. The color bar provides the information of the mag-

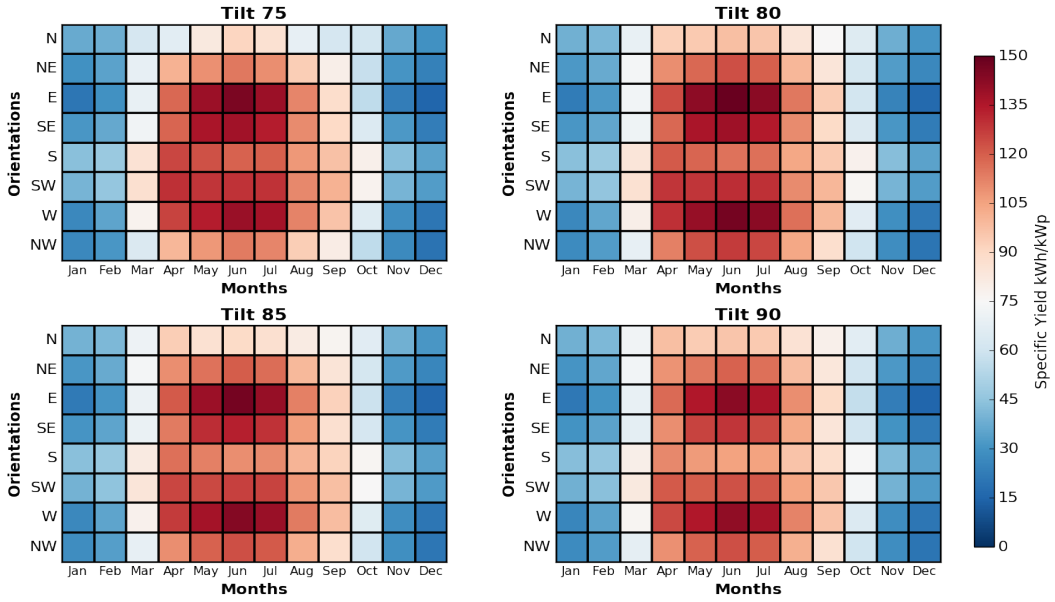

Figure 6.6: Monthly energy yield profiles for all studied scenarios in the case of Den Bosch

nitude of the energy yield in kWh/kWp. Generally, the sunny period can be easily identified by the red color between April up to September while the rest of the months are shown in blue color that reflects the cloudy period.

One key insight that can be obtained from figure 6.6 is that the seasonal performance of PVNB is greatly influenced by the module orientation, while it is less sensitive to the influence of the tilt angle. By looking in more detail to the each orientation result, it can be observed that west and east orientations yield the highest energy during summer time but the least energy during winter with the difference between these two seasons is about 73%. This can be explained by the fact that in summer, the east and west configuration are able to utilize the direct irradiance in the morning and afternoon. whereas during winter, the sun rises in southeast and sets in southwest and thus less direct irradiance reaching the module surface. On top of that, the seasonal performance results presented in this sections are consistent with the findings of SONOB project in which the west facing module performs better on the summer period but worst in winter period compared to the south oriented module [70].

Annual yield performance of different tilt configurations

Finally, the annual energy yield of 32 combinations of tilt angle and orientation are revealed in figure 6.7. The annual yield performance of each left module (Figure 6.7a) and right side module (Figure 6.7b) of the PVNB is presented separately to show the discrepancy effect of the shading losses to the yield performance. Where figure 6.7c and 6.7d represents the frameless[1] situation that can be a performance reference when no shading is present. The accompanying shading losses results for each configurations are given in figure 6.8, where the orange bars represent the relative DC yield (start from 80%) and black bars indicate the shading losses. Furthermore, it should be re-mentioned that the yield value that is presented here is the average of 4 modules of each corresponding side (see figure 6.1a).

The results given in figure 6.7 are quite revealing in several ways. First, figure 6.7a and figure 6.7b show that the south, southeast and southwest orientations at 75^o tilt angle offer the highest

[1]This is based on assumption that the PVNB has no metal structures and therefore the rear surface of the bifacial module is fully free from shading. This condition may not applicable in real condition.

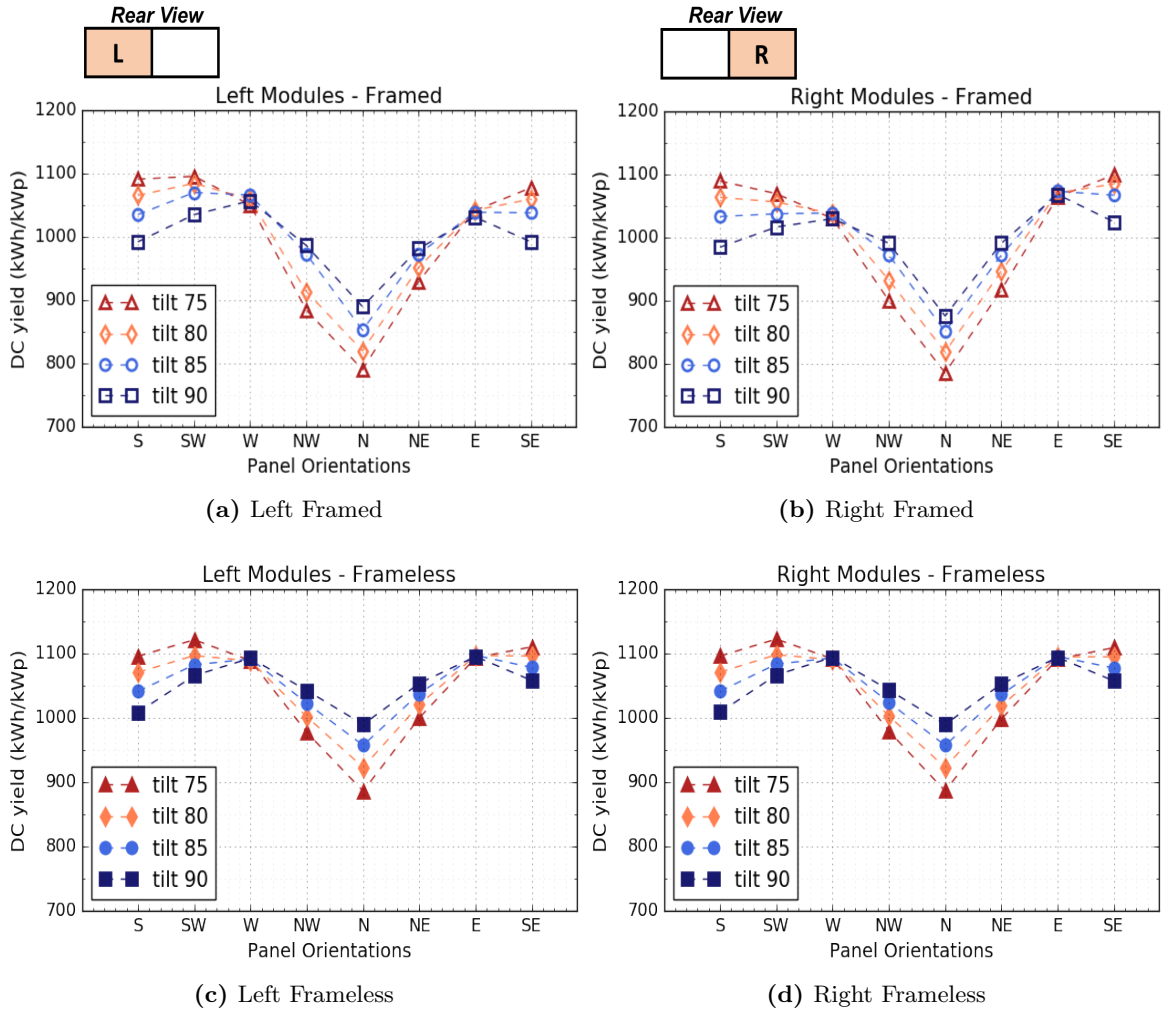

(a) Left Framed **(b)** Right Framed

(c) Left Frameless **(d)** Right Frameless

Figure 6.7: Results of yield performance analysis of PVNB under various tilt and orientation in Den Bosch, the Netherlands. Figure (a) and (b) represent the result of the studied PVNB with accounting shading losses in the model. Figure (c) and (d) show the annual yield result of the ideal frameless PVNB. Small box above figure (a) and (b) indicate the position of the module from rear side point of view (see figure 6.1a).

yield among the other configurations. Whereas, the north facing module at tilt 75^o gives the least energy production with 27.7% less than south orientations at the same tilt angle. Second, regarding the strictly vertical installation (tilt angle 90^o), west and east facing modules outperform other orientations. Unlike the south facing modules, the results of east and west facing modules show the effectiveness of these configurations that are able to maximize the energy production from the morning and afternoon irradiance. It should be pointed out that the result of south and west configuration from this simulation is strongly similar to the real annual measurement result reported in SONOB project with 1051 kWh/kWp and 1005 kWh/kWp for south and west orientation respectively[2][70].

In terms of the influence of the tilt angle to the yield performance, there is a tendency for southward orientations[3] to generate less energy when the tilt angle is increased. Inversely, the increments of annual energy yield of northward orientations are shown when the tilt angle is higher. The reason for this behavior lies in a higher contribution of the south facing rear side in generating power due to higher direct irradiation reaching the surface when the tilt angle

[2]The results lower for the field test due to additional shading experienced by the front panel of both panels
[3]South, southeast, and southwest direction

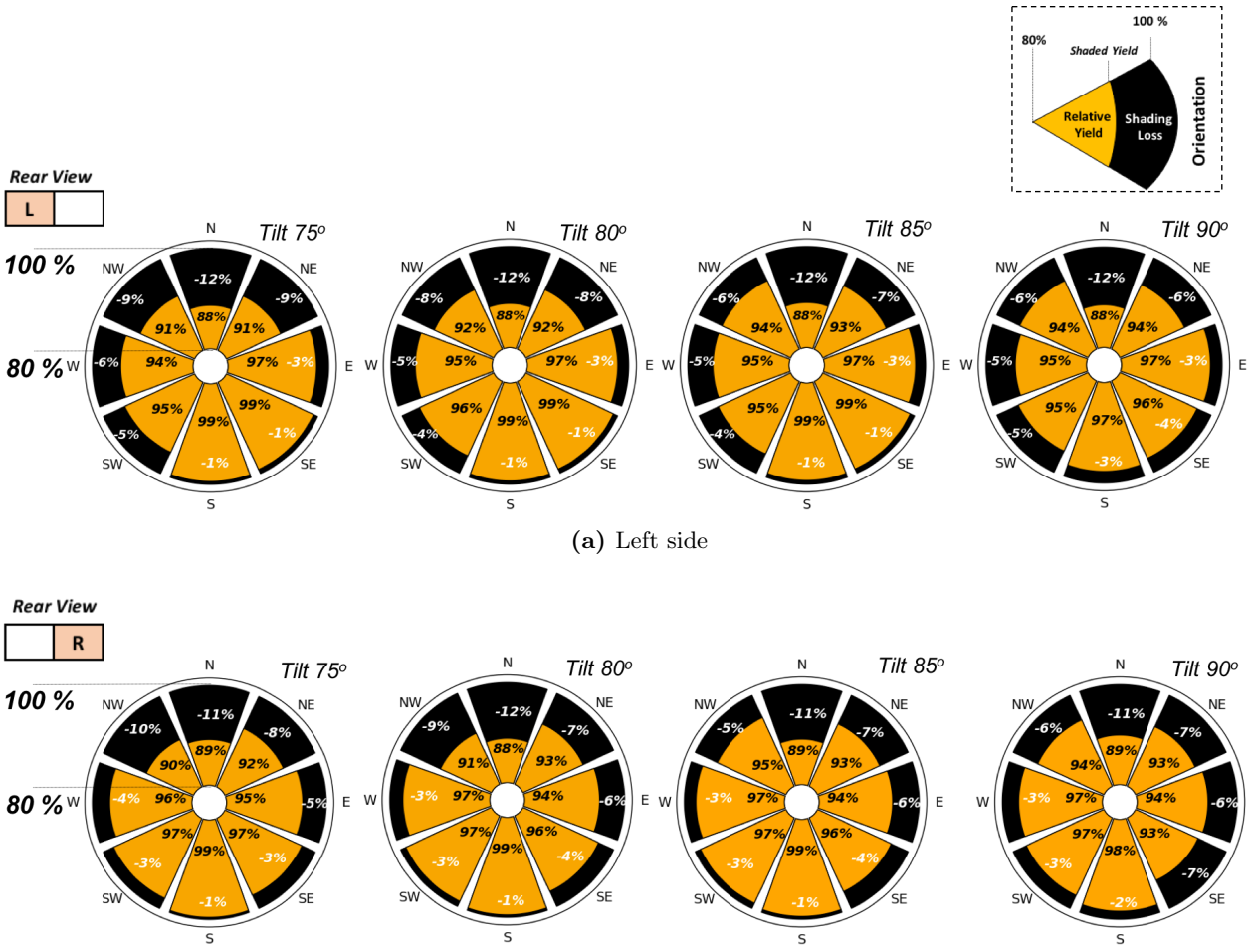

(a) Left side

(b) Right side

Figure 6.8: The quantification Shading losses for left modules (a) and right modules (b) for every orientations and tilt angle scenarios. Note that the relative DC yield in orange bars start from 80% to improve the readability. Small box above figure (a) and (b) indicate the position of the module from rear side point of view (see figure 6.1a). Refer to the picture on the top right corner for the legend.

is increased. Surprisingly, the east and west facing modules are less sensitive to the tilt angle variation as the annual yield results are almost constant for every tilt angle parameters.

Next, the annual yield difference between the left module (6.7a) and the right module (6.7b) of east and west orientations are visible. The disparity of the shading losses between the left side and right side of west facing module is responsible for these conditions. With 3% losses for the left modules in figure 6.8a and 10% losses for the right modules in figure 6.8b. The trend is opposed to the east configuration, where left side experiences more shading losses than the right side. This behavior lies to the fact the each module on the left and right experience different partial shading condition as shown in Appendix A. This aligns with the observation of frameless panel in figure 6.7c and 6.7d where the left and right modules generate the same amount of energy if the back side of the modules are completely free from shading.

Also, as expected, severe shading losses are found in the northern orientations with 12% for left modules and 11% for the right modules. In contrast, the yield losses due to shading for south facing modules are extremely small, with shading losses index less than 2%. The small losses is mostly due to the orientation of the rear side of the module, which is facing north and hence only receive the diffuse irradiance most of the time.

6.2 Different module elevations

The yield performance of bifacial module in different elevation from the ground is observed in this section. This is done to assess whether the energy boost effect by placing bifacial module in higher elevation, that happens in a low tilted south facing bifacial module (0^o - 40^0), is relevant for such vertical PVNB application. Four different module elevation scenarios, from 1 m to 4 m, are compared (see figure 6.1b). Besides the variation of module elevations, albedo values are varied from 0.2 to 0.35 and 0.5. While other parameters in table 6.1 are kept constant. Furthermore, only result of south, north, west, and east presented in this section.

Inhomogeneous irradiance on rear surface

Upon the energy yield performance analysis, it is good to have the knowledge in how the shaded ground influences irradiance distribution on rear surface of the PVNB modules for each orientation. As was mentioned before in section 2.3.2, according to the view factor concept,

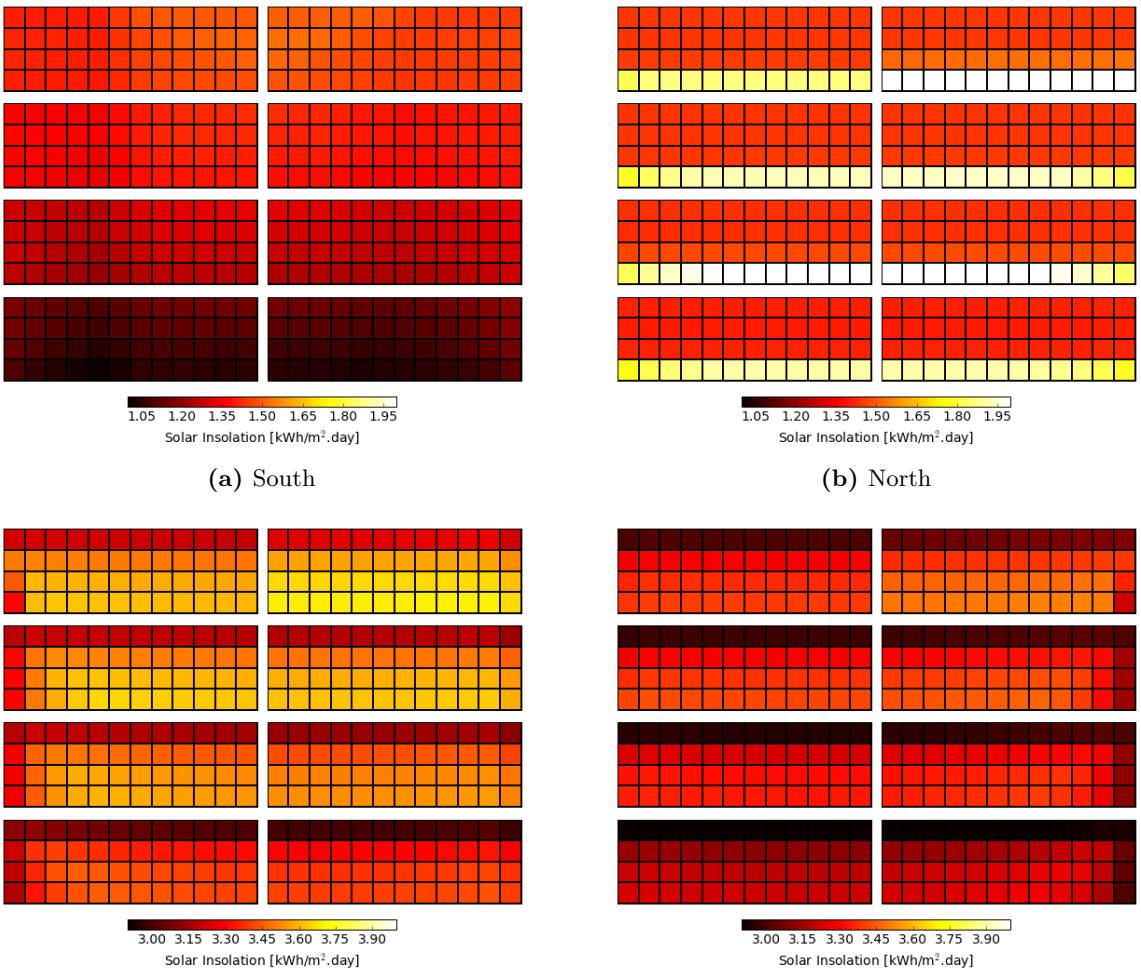

(a) South **(b)** North

(c) West **(d)** East

Figure 6.9: Daily solar insolation distribution of eight back sides bifacial module in studied PVNB during the summer solstice (sunny day). The black solid line indicates the partition of the module area that consists of 48 cells. The inhomogeneity distributions are shown by the gradation of the color on each cell. Despite the different color bar scale in each figure (a) (b) (c) and (d), the range are chosen to be the same for 1 kWh/m^2.day to properly show the comparison of the non-uniformity of irradiance.

the amount of irradiance received by the rear surface is highly dependent on the shadow area on the ground. Due to panel structure and its orientation, the shape and the position of the shadow on the ground is continuously changing and resulting to the inhomogeneity of irradiance distribution on the rear surface.

Figure 6.9 illustrates the simulated rear surface daily cumulative irradiance distribution that received by each cell in full (eight modules) PVNB system. A sunny day in summer solstice was selected as the comparison day as the impact of the shaded ground is more pronounced than in cloudy conditions, as was proven by experimental validation in section 3.4.3. In figure 6.9, the reduction of reflected irradiance by the shaded ground is not the only variable that is responsible for the non-uniformity of irradiance distribution, but also by the impact of the self-shading by the metal structure. For example, in figure 6.9c, the darker regions are similar to the shading patterns that are shown in figure A.1 and vice versa for east configuration in figure 6.9d. Also, for the north orientation in figure 6.9b, the darker regions in the top three rows indicate the influence of self-shading throughout the day (see figure A.1).

Again by looking at figure 6.9, it can be clearly seen that the amount of irradiance reaching the rear surface gradually increases from bottom to the top of south (Figure 6.9a), west (Figure 6.9c) and east orientation (Figure 6.9d). The distance from the cell to the shadow plays an important role and due to its position further away from the ground, the module in the higher position will receive more reflected irradiance. By closer look into each orientation, as expected, the influence of shaded ground is more pronounced for south facing modules in figure 6.9a while the difference between the bottom modules and top modules is hardly visible. This is due to the rear surface, that facing north, always sees the shadow. The impact is also visible for east and west facing modules in figure 6.9c and 6.9d. Contrary, as can bee seen in figure 6.9b, the effect is less prominent for north configuration. This can be explained by the fact that shadow on the ground merely exists in south direction and therefore more uniform irradiance for each level elevation is expected.

Annual yield performance for different module elevations

Figure 6.10 illustrates the annual energy yield of the bifacial modules as a function of module elevation for three different ground albedo values. While Table 6.2 is served as a companion of figure 6.10 to quantify the yield gain of each module in higher elevation in respect to the lowest module (equation 6.1). The results from each elevation are the average of left and right side of each row as illustrated in figure 6.1b. It should be noted that the magnitude order of annual yield is mostly related to the orientation of the module.

Looking at figure 6.10a first, as expected, the influence of reflected irradiance reduction is hardly be noticed for north facing module. The gain quantification in table 6.2 also shows that there is no increment of yield when modules are located in a higher position for north orientation. Whereas, the differences are more noticeable for east, west, and south orientations in the same figure. This can be explained by the fact that the larger amount of irradiance received by rear surface the module in higher elevation (as shown in figure 6.9a, 6.9c, 6.9d) and thus resulting a higher power output. Nevertheless, the yield gains are relatively modest with only about 0.5% - 1% for 0.2 albedo value.

Furthermore, by comparing figure 6.10a with 6.10b and 6.10c, it is evident that as the albedo increases, the increment of annual energy yield from the lower elevation to the higher elevation is more significant. This effect is shown by the steeper gradient of blue, red, and green line on figure 6.10c and figure 6.10b compared to figure 6.10a. The gain for the south facing modules in the highest elevation can reach as high as 3.6% for 0.5 albedo value compared to the bottom

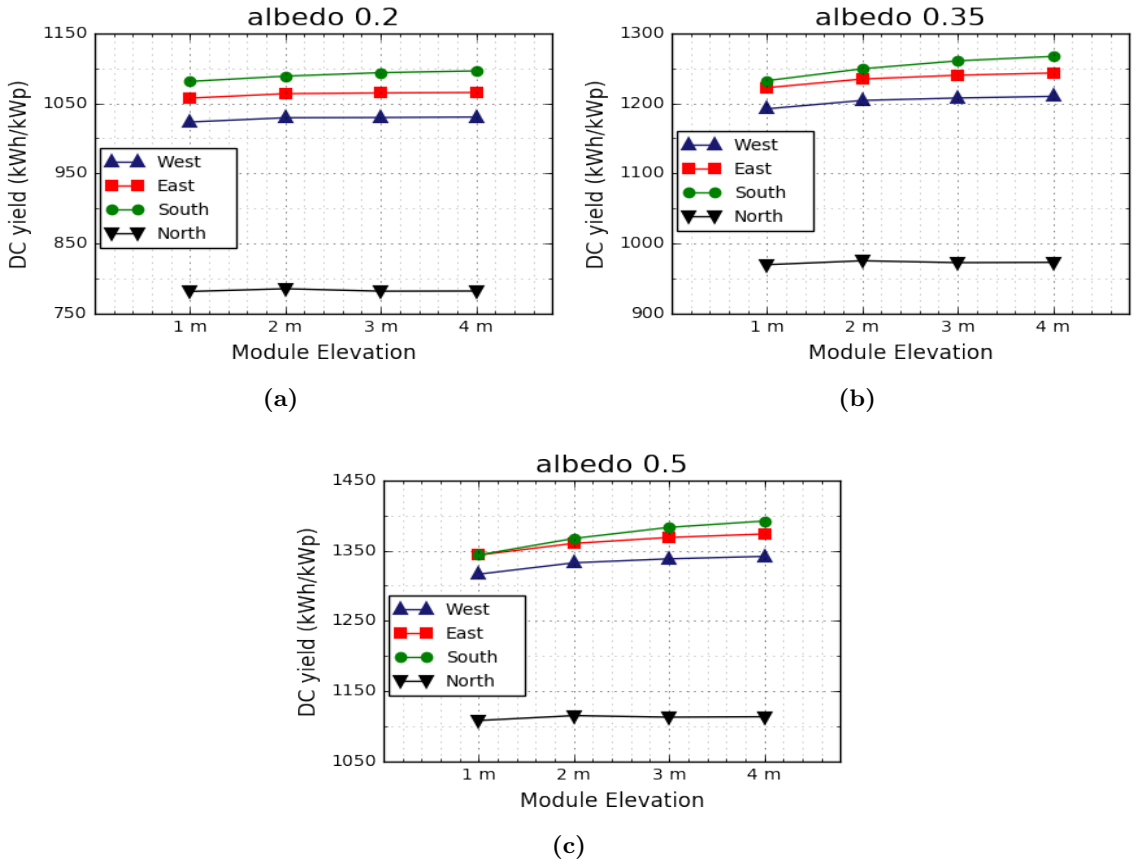

Figure 6.10: Annual energy yield of bifacial module as the function of elevation from the ground. Figure (a), (b), and (c) show the result for 0.2, 0.35 and 0.5 ground albedo values respectively. See figure 6.1b for the illustration of module elevation classification.

one. However, again it is not the case for the north oriented module as the similarity of the annual yield shown for each module elevation even when the albedo value is increased. On top of that, a positive linear relationship between albedo and irradiance is shown by the gradual increase of annual yield from albedo value of 0.15 to albedo value of 0.5.

$$Gain = \frac{E_{yield\,n.meter} - E_{yield\,1.meter}}{E_{yield\,1.meter}} \tag{6.1}$$

Table 6.3: Annual yield gain of different module elevations

	Yield Gain (Albedo 0.2)				Albedo 0.35				Albedo 0.5			
	1m	2m	3m	4m	1m	2m	3m	4m	1m	2m	3m	4m
South	-	0.6%	1.1%	1.3%	-	1.3%	2.2%	2.8%	-	1.7%	2.9%	3.6%
West	-	0.5%	0.6%	0.7%	-	1.0%	1.2%	1.4%	-	1.2%	1.6%	1.9%
East	-	0.6%	0.7%	0.7%	-	1.0%	1.4%	1.7%	-	1.2%	1.8%	2.1%
North	-	0.1%	0.1%	0.1%	-	0.3%	0.3%	0.3%	-	0.4%	0.4%	0.4%

6.3 Variation of bypass diodes layout

The objective of this section is to tackle partial shading problem by optimizing the bypass diodes configuration within the bifacial PV module. This is done by comparing the annual energy yield performance of bifacial PV module under different bypass diodes number and layout interconnection. Thanks to the flexibility and great accuracy of the developed model that has been validated in section 5.2, it is possible to say that the results of this particular shading mitigation study are reliable.

Seven different scenarios are analyzed, including without bypass diode condition in the module as the reference. While the other six configurations are mentioned in table 6.2 and illustrated in figure 5.4. Again, to avoid repetition, only the results of north, south, east and west orientations that will be shown. The results of the other four orientations can be found in appendix C.

Shading response performance of each bypass diodes configuration

Figure 6.11 gives the shading tolerant performance of each bypass diodes configuration in this study. Figure 6.11a and 6.11c illustrate the direction of the artificial horizontal and vertical shading respectively. While figure 6.11b and 6.11d show the simulated relative output power as a function of corresponding horizontal and vertical shading.

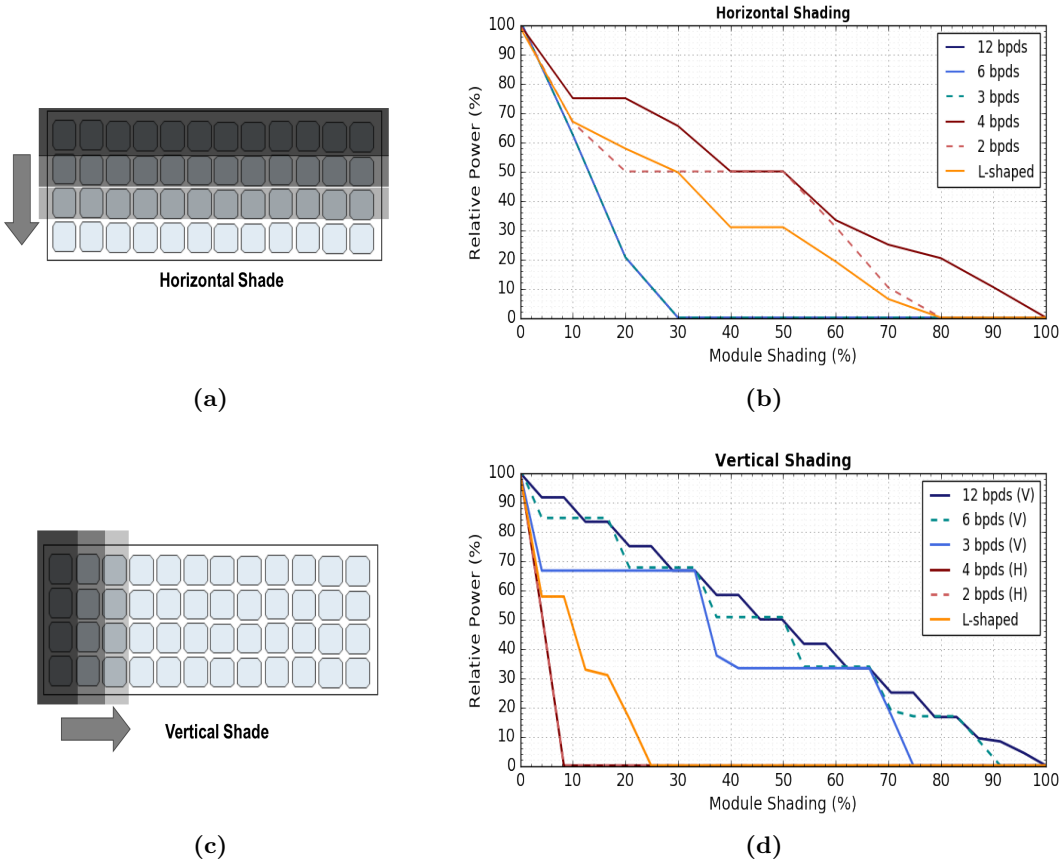

Figure 6.11: Simulated relative power losses as the function of shaded area in horizontal (a) and vertical (b) direction for each electrical bypass diodes interconnection in the scenarios. In this case, it assumed that there is no illumination contribution from the front side and no diffuse irradiance reaches the cell when it is fully shaded. See figure 5.4 for the design layout illustrations.

For horizontal shading case, it can be observed in figure 6.11b that the power output of vertical layout scenarios (3(v), 6(v), and 12(v)) deteriorate very quickly when the module starts to get shaded horizontally. This leads to a total power loss when the 12 cells in the first row are totally shaded. Whereas, the horizontal layout configuration (2(h), 4(h)) only suffer partial power loss that relative to the area of horizontal shading in the module. Inversely, in figure 6.11d, the vertical layout configurations are performed better than the horizontal layout. It should be noted from these two graphs that the module is more shading tolerant if the number of bypass diodes is increased, and therefore a higher energy yield is expected. In addition, it is fair to say that performance of L-shaped configuration (in orange line) is moderate for both vertical and horizontal shading. The effectiveness of this tailored electrical layout will be judged by the result in the following paragraphs.

Annual Yield comparison in different bypass diodes configuration

Figure 6.12 illustrates the simulation result of the said mitigation scenarios. Here, only north, east and west orientations will be shown graphically. Refer to appendices C for the other orientation results. The result shown in figure 6.12 is very telling, with orange bars represent the specific yield in a scale to the unshaded condition in black bars. Green bars with the yellow numbers next to it illustrate the potential benefit that can obtained for the corresponding electrical design scenarios.

For the north orientations results in Figure 6.12a and 6.12b, vertical substring configurations perform significantly better in terms of mitigating the partial shading losses compared to horizontal interconnection. This is due to the shading pattern that is mostly coming from the left or right side of the module in a vertical shape (Figure A.2 and A.3). This can also be explained by looking at figure 6.11 in which a stronger tolerance to vertical shape shading are shown by the vertical substring layout design. Moreover, the remaining large portion of shading losses is likely due to condition when all cells in the module are completely shaded, particularly throughout summer period (see figure A.1). In the case of west and east orientations, the side that gets heavier shaded losses (left side for west and right side for east) tend to perform better when vertical layout designs are applied. On the other hand, due to the shading shape that coming horizontally from the top, (see figure A.1) the horizontal substring layout is more effective in mitigating the shading for the modules on the other side. The non-uniformity of shading shape cast on the left and right side, as shown in figure A.1, A.2 A.3, is the main reason for this behavior.

In addition to that, it is also clearly visible from figure 6.12 that there is a tendency of higher potential yield by increasing the number of bypass diodes either in the vertical or the horizontal substring layout. This is due to the more current that is bypassed during partial shading condition when the number of bypass diodes is increased. Nevertheless, it is also worth mentioning that the L-shaped configuration performs relatively consistent on every side of each orientation. Although the performance in mitigating the shading losses is slightly lower than 12 bypass diodes layout in west and east configuration, the L-shaped layout outperforms the vertical layout for the same number of bypass diodes (3 bypass diodes) in north orientations (Figure 6.12a and 6.12b). This shows the effectiveness of tailoring the electrical layout in accordance with the shading pattern that falls on the PV module surfaces.

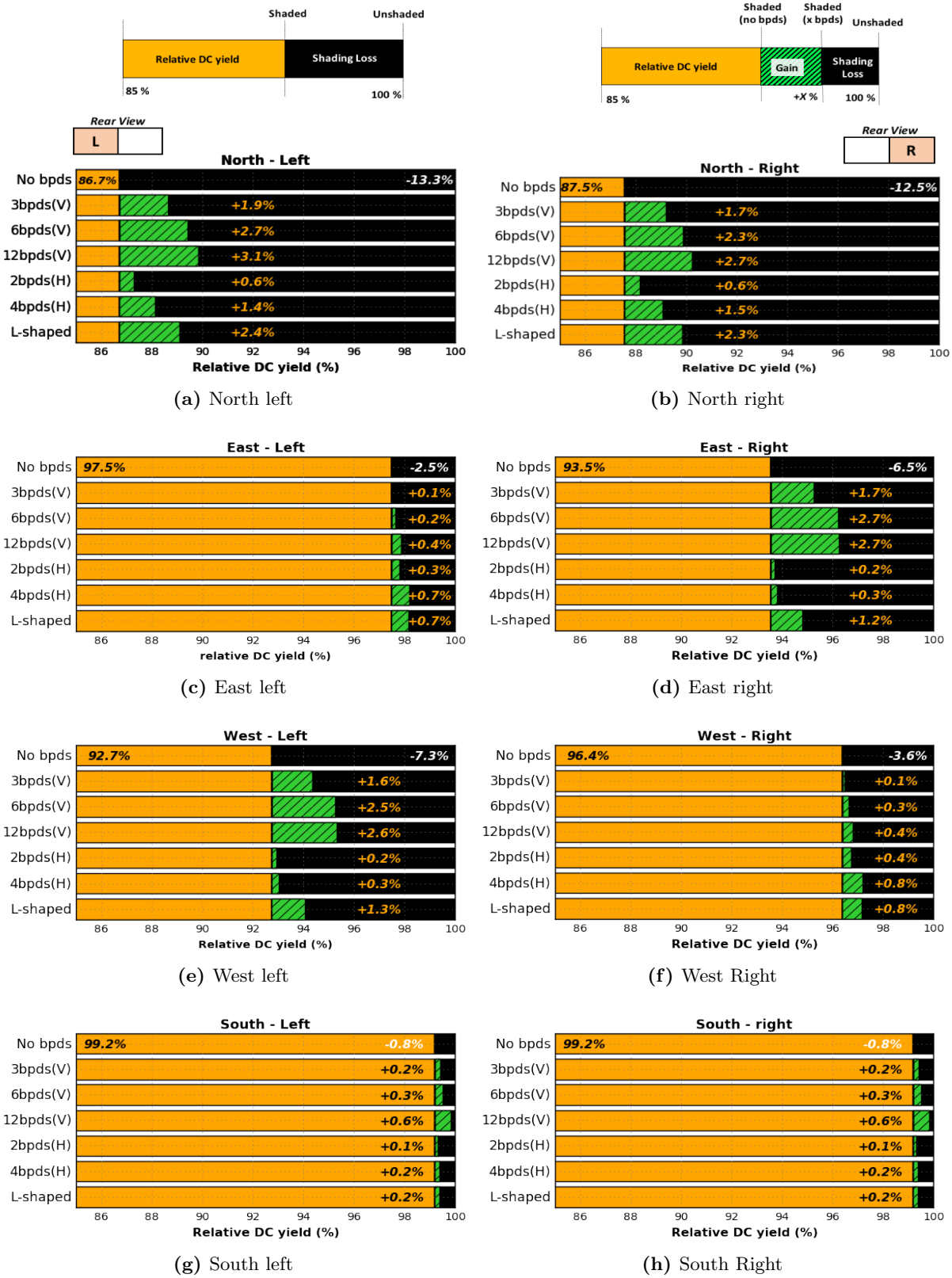

(a) North left **(b)** North right

(c) East left **(d)** East right

(e) West left **(f)** West Right

(g) South left **(h)** South Right

Figure 6.12: Shading mitigation results by using different bypass diodes layout interconnections for four different orientations: 1) North - Figure (a) and (b). 2) East - Figure (c) and (d). 3) West - Figure (e) and (f). 4) South - Figure (g) and (h). Note that the DC relative yields in orange bars are scaled which start from 85%. Green bars with the number next to it, represent the recoverable shading loss when the corresponding electrical module design is implemented. See figure 5.4 for the design layout illustrations.

6.4 Different cells positioning

The cells position in the glass section is the parameter that is varied in this section. Other parameters including the tilt angle, bypass diode layout, and albedo are kept constant as given in table 6.1.

Figure 6.13 depicts the illustration of 3 different cell positioning scenarios in the glass section of PVNB. The standard cells positioning that used in other simulation in this chapter are used as the reference. Whereas, two other conditions are selected to represent the extreme conditions: The Broad scenarios where the cells are evenly distributed throughout the glass section and the Narrow scenarios where all the cells are placed further away from the both side structures and top structures. The shading tables were created for these two new scenarios prior to the yield simulations[4].

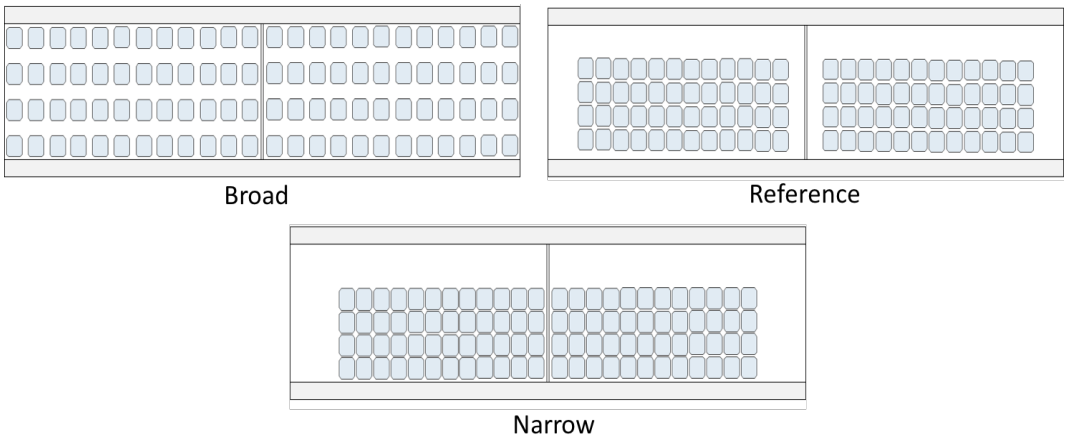

Figure 6.13: Illustration of the three different cells positioning scenarios.

Annual yield performance of different cells positioning scenarios

Figure 6.14 demonstrates the annual yield simulation results for eight different orientations. The frameless yield results are illustrated in the same graph in gray bar and hence the shading losses for each scenarios can be approximated. As expected, the broad cell positioning scenario experiences heavier shading losses compared to others two cells positioning scenarios. This happened for the most orientation except the south orientation where the shading losses are already fairly small. The reason is that for broad scenarios, the closer the outermost cells to the structures, the faster they get shaded and induces power drop in a longer period compared to the two other scenarios. Whereas the transition from the reference scenario to narrow scenario is not significant as the increment of the yield is relatively modest. For example, in the case of northwest orientation, the annual energy yield is increased by 110 kWh/kWp from broad scenario to the reference scenario but only rises by 30 kWh/kWp when the narrow scenario is implemented. These results confirm that the shading losses can be effectively reduced by placing the cells away from the side structures and therefore increase the energy yield production of bifacial PVNB modules.

[4]It is assumed there is no change in PV module series resistance although the length of metal contact is varied for each positioning scenario.

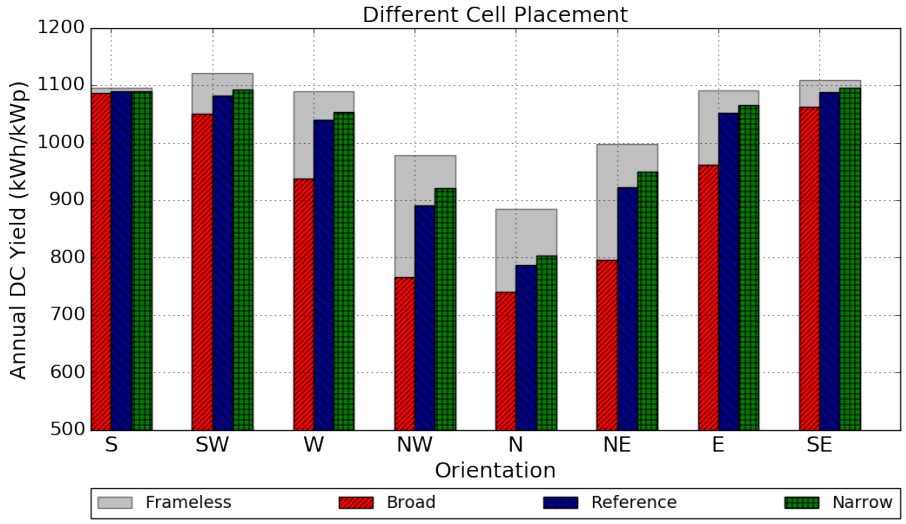

Figure 6.14: Annual yield result of three different cell positioning scenarios for every orientations at 75^o tilt angle configuration. The frameless results are plotted for unshaded condition reference.

6.5 Different geographical locations

As was mentioned in the research questions, another aim of this thesis is to examine the energy yield performance characteristic of bifacial PVNB in other locations on the earth. Four locations are selected to represent different climate and geographical locations. These are Reykjavik, Dubai, Jakarta, and Melbourne. Also, the potential of motorways in the city is another reason to choose these cities as the scenarios. The information regarding the location scenarios are shown in table 6.4.

Table 6.4: Information of the chosen location scenarios

City	*Country*	*Latitude*	*Longitude*	*Geography*
Reykjavik	Iceland	64.12	21.81	Arctic pole
Dubai	Uni Emirates Arab	25.2	55.2	Desert
Jakarta	Indonesia	-6.17	106.82	Equator
Melbourne	Australia	-37.81	144.96	Southern hemisphere

To avoid repetition, the results show in this section are the average of total eight modules in bifacial PVNB. The big pictures of annual yield performance of each location is depicted in figure 6.15. The seasonal performance results for each locations are given in appendix C.1.

Reykjavik As can be seen in figure 6.15a, the results of the annual specific yield of bifacial PVNB in Reykjavik are considerably lower than Den Bosch (see figure 6.7) with the maximum yield is only about 900 kWh/kWp. Once again, the south facing module with 75^o tilt angle is found as the best configuration in generating energy. However, besides the northward orientations, less variation of yield performance can be clearly observed when the tilt angle increases from 75^o to 90^o. Also, remarkable similarities in terms of annual yield are shown for all orientations in the vertical installations. These results most likely happen due the fact that the proportion of diffuse irradiance is higher than direct irradiance for this location and therefore resulting a lower shading losses.

Dubai Figure 6.15b demonstrates the result of the typical annual yield for Dubai location. As

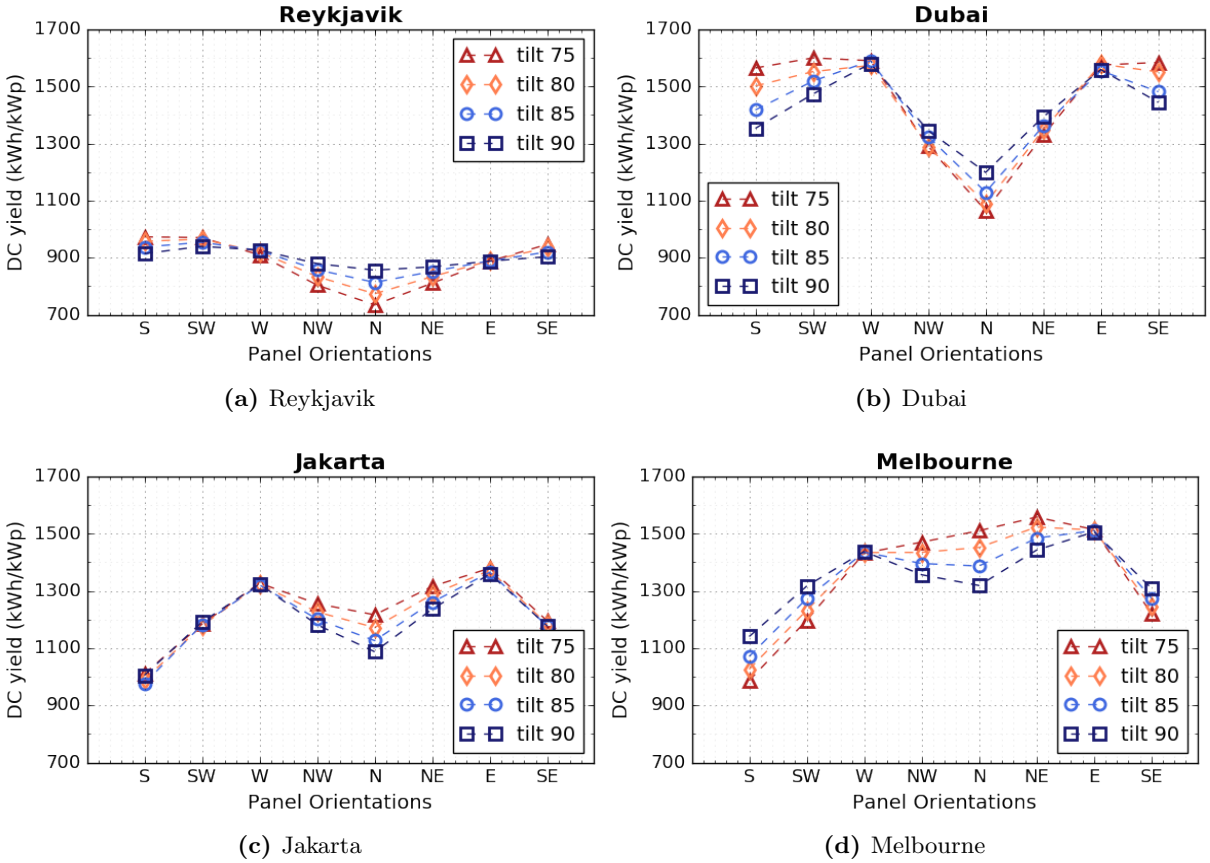

(a) Reykjavik **(b)** Dubai

(c) Jakarta **(d)** Melbourne

Figure 6.15: Annual yield result of PVNB in four different locations. (a) Reykjavik (b) Dubai (c) Jakarta (d) Melbourne. The results presented in these graphs are the average of total eight modules in the noise barrier.

shown in the figure that the yield results of Dubai are notably higher than those shown for Den Bosch in figure 6.7 with the highest annual yield can be as high as 1600 kWh/kWp that shown by southwest facing modules. Interestingly, even the least annual energy yields by the north facing module with 75 levels the best yield performance of bifacial PVNB in Den Bosch with about 1100 kWh/kWp. Also, it is worth mentioning that the result in Dubai as the function of tilt angle have similar variation trends with the result in Den Bosch. This can be explained by the fact that both locations are above the equator line that means the sun is mostly in the south. Regarding the shading losses, due to high availability of direct irradiance in this location, the bifacial PVNB system will suffer partial shading condition in more frequent basis.

Jakarta The results of annual energy yield in the case of Jakarta are reported in figure 6.15c. Unlike the aforementioned location cases, the east and west orientations surpass the yield for the other orientation cases. These highlight results can be explained by the fact that the sun consistently rises in the east and sets in the west throughout the year and therefore utilization of irradiance from these direction are maximized. Also, since the location is just slightly below the equator line, the yield performance due to the change of inclination is more sensitive for northern orientations. In contrast, the yield under different tilt angle for other orientations are more or less similar.

Melbourne The annual yield results of Melbourne case give a strong different pattern compared to the other locations. As it shown in figure 6.15d, due to its location in southern hemisphere, the northern facing module is favourable to be installed slightly inclined backwards in order to enhance the utilization of direct irradiance from the sun that located in the north.

These trends are inversed to the result shown for Den Bosch and Dubai. Surprisingly, the overall yield performance is significantly higher compared to Den Bosch, Reykjavik, and Jakarta. The relatively low shading losses and higher insolation radiation in Melbourne are the reason for the said results.

6.6 Discussions and implications of the obtained results

Yield performance under different inclinations
The typical annual DC yield values of the eight studied bifacial modules in the Netherlands are found in the range of 800 kWh/kWp and 1100 kWh/kWp for north facing and south facing module with 75 ^{o} respectively. By comparing these values to the typical annual DC yield of the monofacial module, the relative yield gain can be as high as 27% for south orientation and about 40% for west and east orientations [70]. These outcomes are shown as a promising prospect for bifacial PV module when being vertically installed in such PVNB application.

The optimum tilt angle for each orientation has been identified as presented in figure 6.7. The prominent characteristic of the bifacial module is shown by the northward orientation in which 12.5% yield increases by letting the PVNB stands vertically. From the shading losses perspective, about 11% loss caused by shading was found in north orientation and only less than 1% for south orientation. In the case of west and east orientation, the absolute shading losses are ranging form 3% to 7% and for about 2% - 3% shading losses difference between left and right modules was discovered. This condition was eventually responsible for the unequal energy yield generate by the modules in the same column and able to add more complex electrical mismatch condition when being connected in array configuration. In this condition, the energy yield loss by the shading is likely to be higher as the results of maximum power point tracking (MPPT) in finding the real maximum power point value in array I-V curves.

Yield gain for different module elevations
Although the energy yield gain is relatively modest, placing module at higher elevation for this specific vertical PVNB cannot be withdrawn from design consideration. This recommendation would be beneficial when there is a budget constraint and only a few PV modules can be installed in one panel noise barrier. Furthermore, remarkable energy yield boost are observed when albedo value of the ground is increased. According to this observation, the trade-off would be very noticeable if white paint or white crushed stone can be artificially made behind or around the PVNB module.

Shading mitigation strategies
The shading mitigation strategies within module design level were also analyzed in this chapter. In terms of bypass diodes design in the module, generally in the Netherlands the vertical layout has better performance in mitigating the partial shading effect. The low altitude of the sun on this location accountable for the vertical shade patterns cast by the side structures that makes the vertical layout substring is more suitable for this condition. It was reported that 23% shading loss mitigation is achieved by applying 12 bypass diodes in vertical layout interconnection in the case of north oriented panel. whereas, regarding the cell positioning strategies, for about 10% shading losses can be tackled by properly placing the cells away from the shade object.

Potential of PVNB in different locations
The yield performance of bifacial PVNB have been studied for four other locations in the world. These were, Reykjavik, Dubai, Jakarta, and Melbourne. The yield performance in Reykjavik showed less variation when the tilt angle is varied. The same behavior was found from the results in Jakarta where the tilt angle variation only plays a role in the yield performance of northward

orientations. Whereas, the yield performance in Dubai is very sensitive to the orientation. One strong similarity that was found in all locations is the yield performance of the west and east oriented bifacial modules are almost constant for every tilt angle scenarios.

Finally, it is worth mentioning that the goal of this chapter in providing a design guideline for bifacial PVNB in the Netherlands was achieved. The guideline design presented here can be a starting point to bring down the cost of electricity produced by bifacial PVNB by maximizing the energy yield. In real project, once the orientation of the PVNB is determined, the design optimization can be done by subsequently adapting the following suggestions: first adjusting tilt angle, then applying the suitable bypass diodes design and placing cells away from the structure. The electronic power conversion system has to be selected carefully as well. In terms of type of the inverter, one should consider the use of power optimizer or micro inverter for north orientation and other configuration that suffer relatively high shading losses. Contrary, in the case of south facing module, these advanced power conversion device seems unnecessary due to the fact that the shading losses is already fairly small.

CHAPTER 7

Conclusions and Recommendations

7.1 Conclusions

The aim of this thesis was to provide a guideline in designing bifacial photovoltaic noise barriers (PVNB). To accomplish this objective, a comprehensive model was required and eventually has been developed. High-resolution and flexibility are the main strong points of the developed model. The model consists of three main sub-models: (i) optical model, (ii) thermal model, and (iii) electrical model.

Bifacial solar module has a great potential when vertically installed and being integrated with the noise barriers. Due to the nature of the noise barrier design, the carrying support structures induce an unavoidable shading to the rear surface of the installed bifacial modules. Moreover, the shadow on the ground cast by the PVNB itself affects the amount of irradiance that reflected back by the ground. These conditions cause inhomogeneous irradiance distribution on the rear surface of the module and therefore substantially reduce the power generation due to the mismatch electrical loss.

The *Modulair geluisscherm* (MGS) standard design published by the Dutch government was selected as a baseline design of the representative bifacial PVNB used in this study [35]. The barrier dimensions and inclination range, from 75^o to 90^o are in compliance with regulation to activate their functionality in reducing polluted noise by 15 dB. The barrier comprises of eight bifacial PV modules (207 Wp) where each of them consist of 48 NSP n-type mono-crystalline bifacial solar cells connected in series with 93% bifaciality factor.

The shading fraction of each cell within the modules was calculated for a full sky hemisphere prior to the irradiance calculation. These were done by translating the 3D Cartesian coordinates of each object and utilizing vector algebra approach to simulate the shade projection on the cell surface and eventually calculate the shading within 10 x 10 grid resolutions.

The incident irradiance reaching the front and rear surface were calculated separately. Besides the shading fraction, the optical losses due to reflections from the module was also accounted in the simulation using the ASHRAE model. The perez model was implemented in sky diffuse irradiance calculation. Due to the presence of the embedded barrier structures, the sky view factor was altered by the ratio of integral of visible sky to total area of hemisphere using the same method as shading simulation. Whereas, for the ground albedo calculation of the rear surface, the influence of shadow on the ground was adjusted by computing the view factor of each cell to the shaded ground. A very good validation result of the irradiance was shown by several means. By comparing the result with Sketchup, ray tracing approach, and field

experiment.

Nevertheless, ray tracing approach with combining sensitivity maps and sky maps in Light-Tools software has also been tested and extended as part of this work. Some suggestions were formulated which can be a future work from this thesis.

The finite element method was adapted for calculating the module temperature. The model works by solving thermal energy balance of each element, the front glass, the rear glass, and the bifacial modules. The proposed thermal model is expected to be more accurate compared to NOCT model especially when the wind speed in the location is high .

In terms of the electrical model, a physically-based energy yield modeling framework was developed. I-V curves construction with specific bypass diodes layout interconnection was considered in the model to match the granularity level of the shading and irradiance model. The input irradiance reaching the rear side of the bifacial cells was adjusted with the bifaciality factor and then applied into the two-diodes equations. This electrical model offers an outstanding precision in I-V curve level which has been validated with the field measurement data. By having the complete yield model validated, the simulation study of bifacial PVNB under different scenarios was performed.

Photovoltaic Noise barrier has a nature to be adjacent to the road and therefore forces the PV module to not facing the optimal direction which, in the case of the northern hemisphere, is facing south. Therefore several optimization scenarios that include the performance under different tilt angles, module elevations, bypass diodes configurations and cell positioning were performed using the developed model. Furthermore, the simulations to investigate potential of bifacial PVNB in different locations were conducted. However, the simulation studies were narrowed down only for the overall performance under different inclination angles. One can follow a similar procedure used in the case of the Netherlands if there is an intention to perform a thorough study in other specific location in the world.

In the case of the Netherlands, it was reported that the southward PVNB orientation with 15^o backward inclination from vertical outperformed the other configuration scenarios. It is important to mention that the result is in good alignment with a recent field test result study of bifacial PVNB in the Netherlands [70]. Interestingly, the yield performance result for west and east facing modules are consistent for every tilt angle variations. Regarding the performance in different module height from the ground, the energy boost for module in higher elevation was not as dramatic as a south facing module with a low tilt angle (15^o - 40^o) as reported in the literature [23]. Furthermore, the quantification of shading losses for each configuration scenarios was also reported with the losses percentage in the range of 1% - 12%. It was shown that the northward configurations suffered the heaviest shading losses compared to other orientation. Interestingly, the shading losses between each side of the module may vary as was shown from the west and east configurations.

Two shading mitigation studies within the module level design were performed. Recalling the knowledge of shading pattern, the need to tailoring bypass diodes layout to the specific shape casted on the individual module is clearly visible. In the Netherlands, the vertical bypass diodes layout was found to be more suitable for the most orientations. Secondly, the shading losses can be significantly reduced by placing the cells away from the side structures. The second strategy might be the simplest and the cheapest strategy that should be strongly considered in the initial phase in designing PVNB. It should be emphasized here that the module in PVNB is customizable and therefore the said modification of electrical layout interconnection and cells positioning are practical.

Furthermore, a study to explore the potential of such bifacial PVNB in four different places in the world was performed. Generally, Dubai and Melbourne are the most prospective locations to install the bifacial PVNB in which the prediction of annual yield can be as high as 1500 kWh/kWp which is almost 50% higher than Den Bosch. One remarkable similarity was found from the result in five different locations, the west and east orientations are less sensitive to tilt angle variation and always generate the highest annual energy yield in vertical installation in every location.

Finally, it can be said that one of the main goals to develop an accurate and advanced model with high-resolution for bifacial PV system in the built environment was achieved. The developed modeling framework is also applicable for more complex shading environment and other PV technologies with only small adjustment required. The information about yield performance of bifacial module integration with noise barrier was explored in the simulation study and provided the answer to the main research question in this study. This information derives a design guideline that is generally applicable for a future bifacial PVNB project.

7.2 Recommendations

There is still room for further research work in this field. First, since this thesis has a focal point in researching the performance of bifacial PVNB system, the next step is to conduct a further research of bifacial PV module application in general. From residential roof system to the utility-scale of bifacial PV plant. Also, it would be very interesting to study the performance of floating bifacial PV application in how they maximize the irradiance reflection by the water. Note that the yield modeling framework in this thesis is versatile and depends on the complexity of the geometry and environment, both numerical geometry model or ray tracing model can be easily integrated.

Regarding the developed yield model, one could improve the accuracy of the electrical model by implementing the voltage drop and leakage current due to the activation of bypass diodes under partial shading condition. Further improvement of the thermal model can be done by taking into account the electro-thermal effects due to hot spots caused by the partial shading condition. In addition, the thermal model can also be improved by considering unsteady state condition (accounts for the specific heat of the material)if smaller time-step calculation is considered.

Another exciting topic that might be performed in the future is to couple the shading model in this thesis with a Lidar approach that has been previously developed in TU Delft [71]. The developed lidar model is able to generate a horizon image with a very good accuracy. However, this model has a drawback which unable to simulate a partial shading condition. It should be pointed out that the fundamental algorithm of both models are rather similar by using the XYZ Cartesian coordinates of the objects and therefore the combination is workable. The integration of these two model along with the high-resolution electrical model in this thesis can be a powerful PV system simulation tool that is fast yet accurate for any BIPV application in the Netherlands.

For the bifacial PVNB case, the utilization of ray tracing approach shall be done to analyze the complex optical behavior within the glass-glass module. How much is the contribution of internal reflection inside the glass to the power output of bifacial module? Is there any benefit on the reflected irradiance received by the rear module by varying the packing density of the bifacial module? These questions can be a starting point for future bifacial simulation work.

Nevertheless, this thesis provides a solid foundation for further feasibility study of a large-scale

bifacial PVNB plant that accounts the full economic analysis including the return of investment (ROI) and levelized cost of electricity ($LCOE$). Moreover, performing a dynamic power exchange simulation study could deliver a valuable input for determining the most optimum design for the balance of the system (BOS). The results of the power exchange study along with the design recommendation from this thesis undoubtedly will make the bifacial PVNB more viable when it comes to realization.

Appendices

APPENDIX A

Shading Patterns

Additional information of the shading patterns for three different seasons are given in this section. The figures contain useful information for shading analysis in chapter 6.

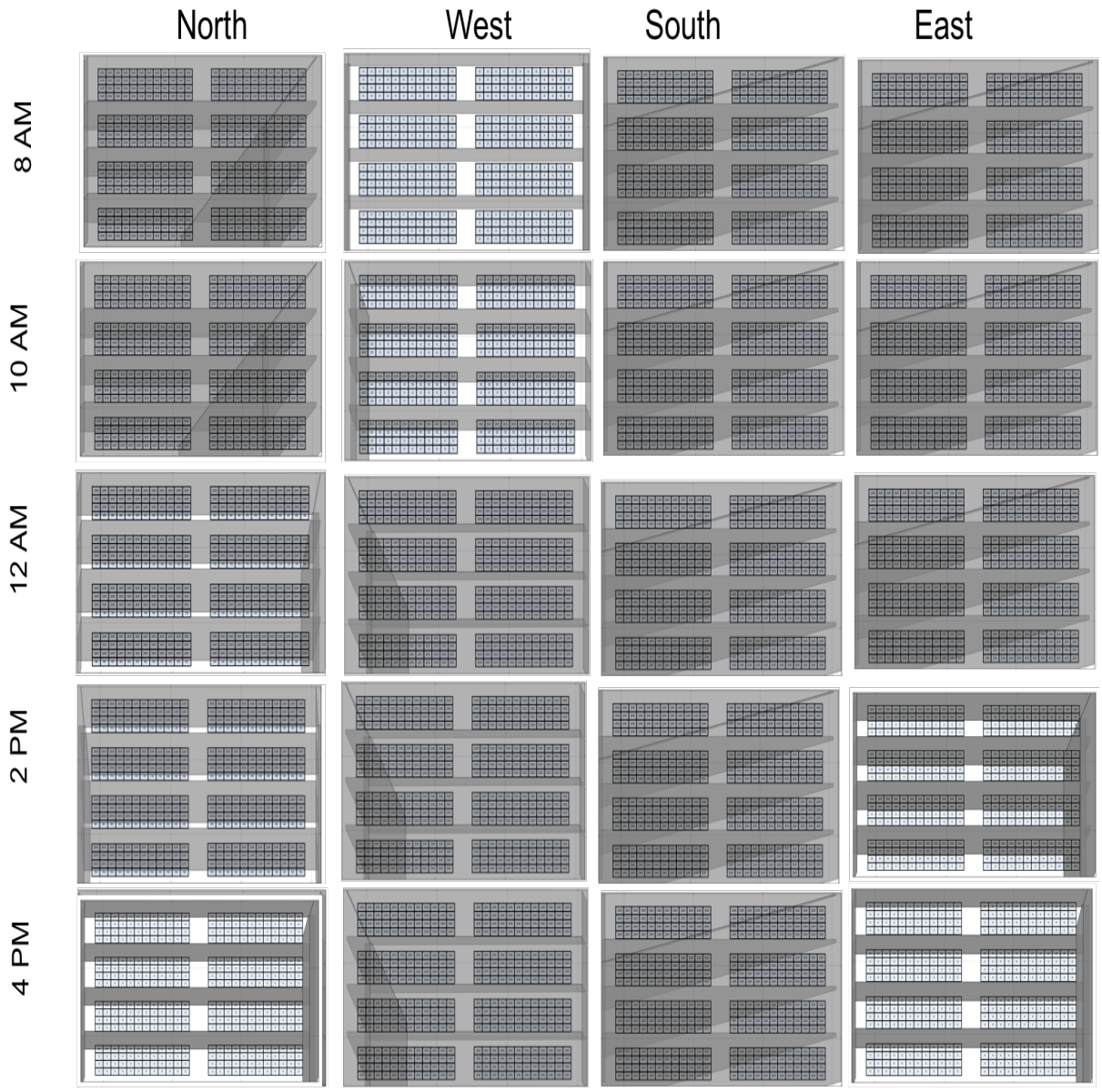

Figure A.1: Shading patterns for summer (21^{st} June)

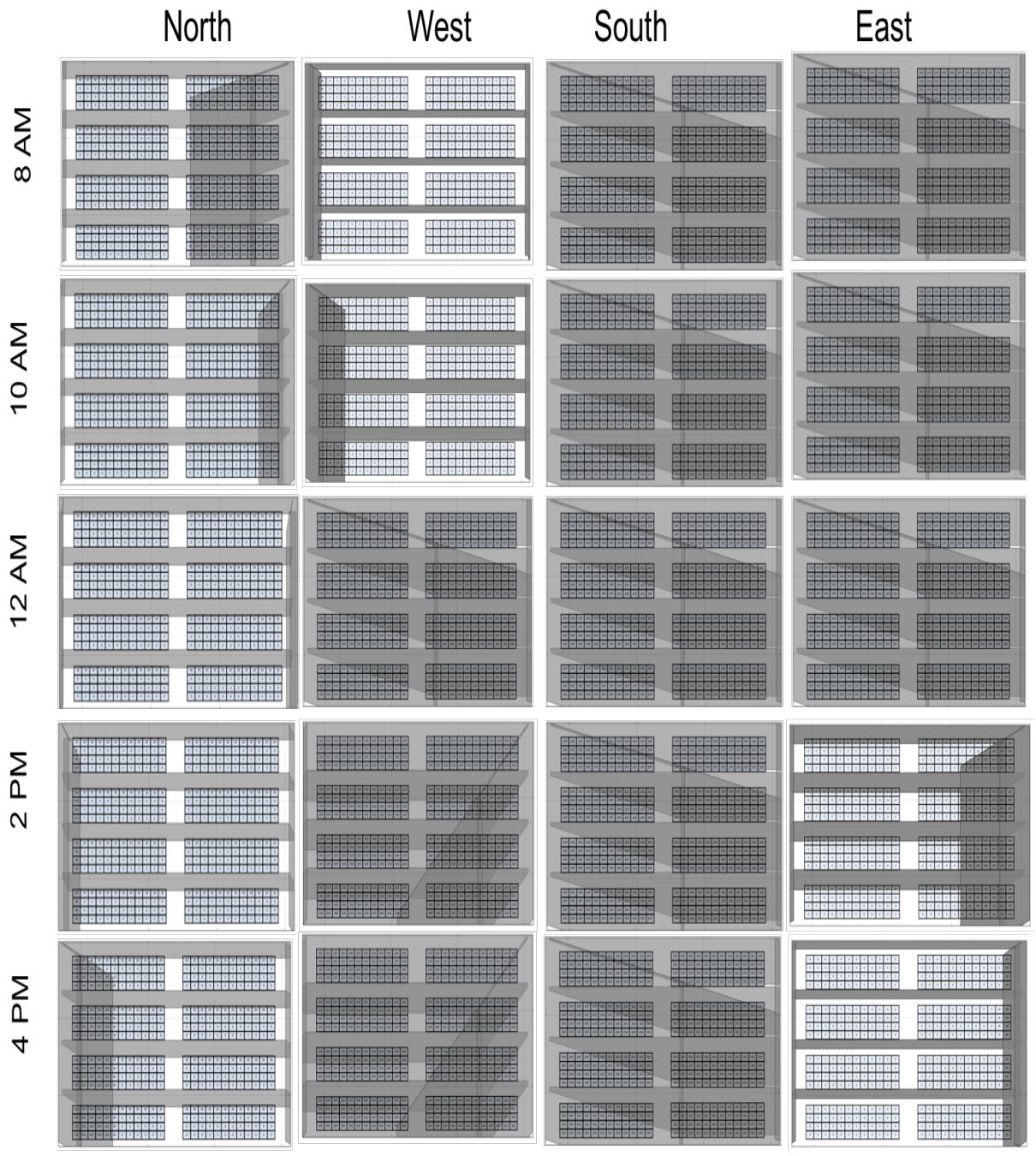

Figure A.2: Shading patterns for summer (21^{st} October)

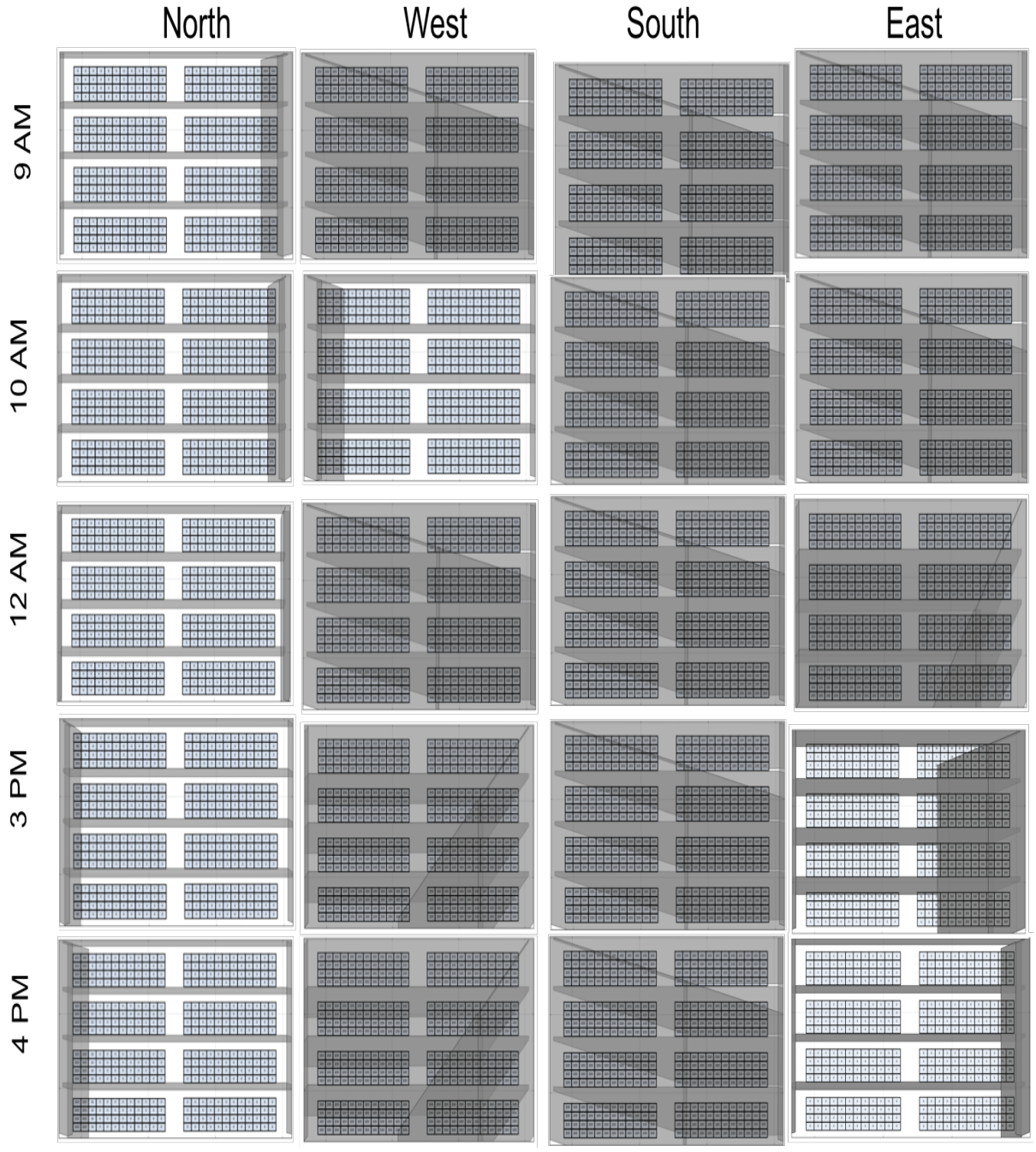

Figure A.3: Shading patterns for summer (21^{st} January)

APPENDIX B

Shading mitigation results of other orientations

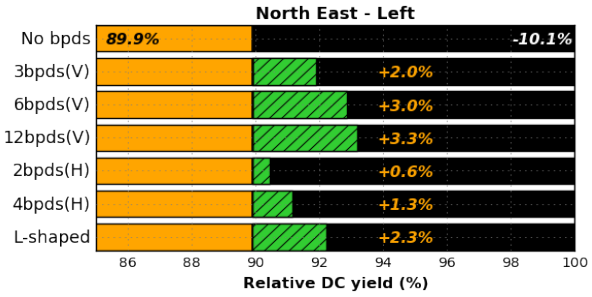

(a) North east - left

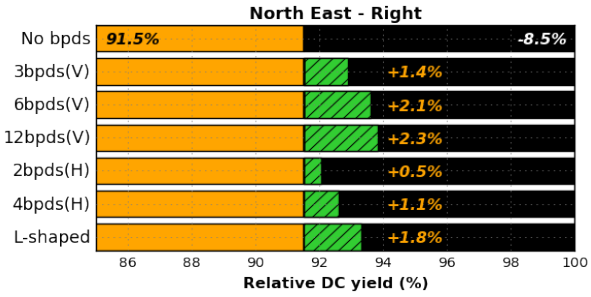

(b) North east - right

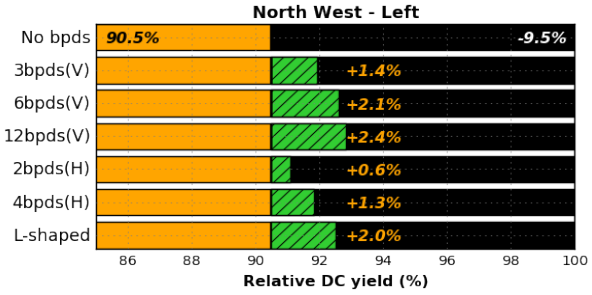

(c) North west left

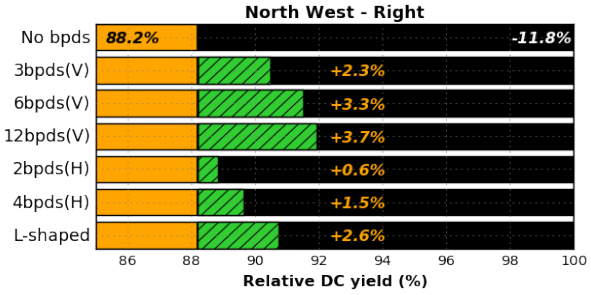

(d) North west right

Figure B.1: Shading mitigation results of north east and north west orientation.

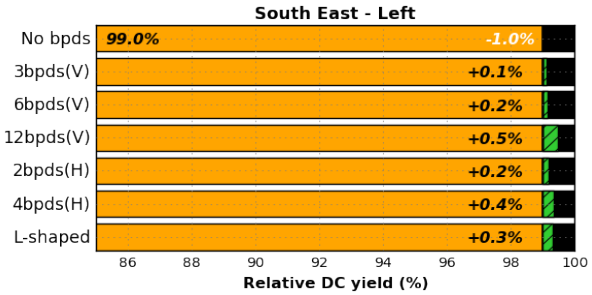

(a) South east left

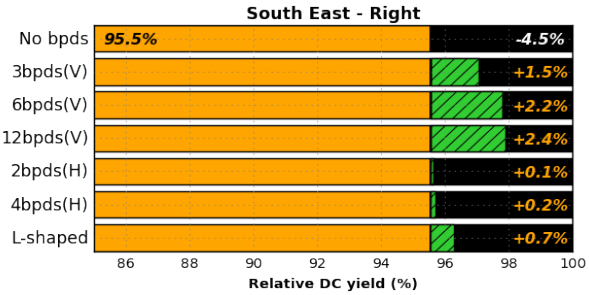

(b) South east right

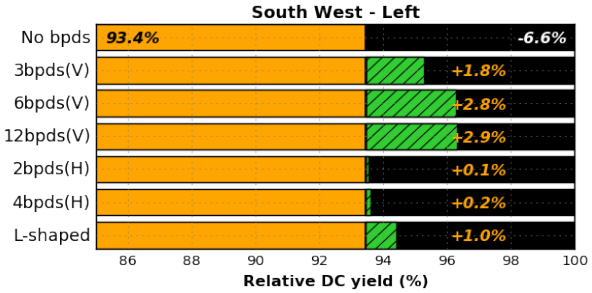

(c) South west left

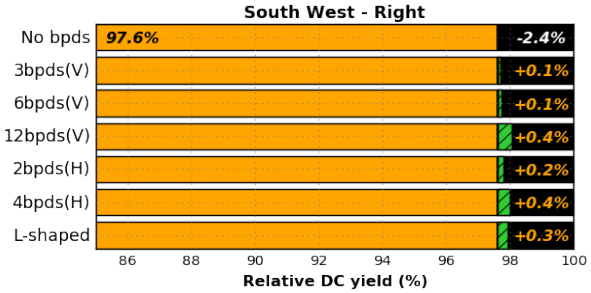

(d) South west right

Figure B.2: Shading mitigation results of south east and south west orientation.

APPENDIX C

Seasonal performance resuts for different locations

As was mentioned in section 6.5, the result of seasonal energy yield performance of different locations are given in this appendix.

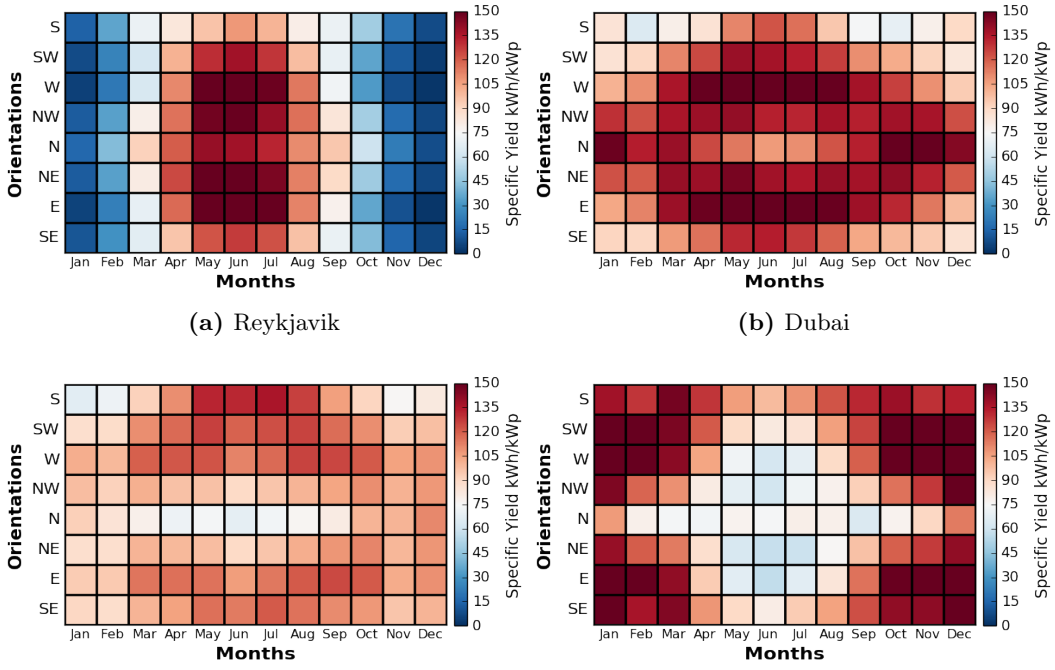

(a) Reykjavik **(b)** Dubai

(c) Jakarta **(d)** Melbourne

Figure C.1: Monthly energy yield results of PVNB at four different locations. (a) Reykjavik (b) Dubai (c) Jakarta (d) Melbourne. Note that the climate of each location is clearly visible by the distribution of irradiance throughout the year.

Bibliography

[1] European Union, "The European Union leading in renewables," *Cop21*, 2014.

[2] N. Planning and C. Secretariat, *Statistical Pocketbook*. 2014.

[3] European Commission, "Renewable energy progress report," 2015.

[4] REN21, *Renewables 2015-Global Status Report*. 2015.

[5] N. Kasahara, K. Yoshioka, and T. Saitoh, "Performance evaluation of bifacial photovoltaic modules for urban application," *3rd World Conference onPhotovoltaic Energy Conversion, 2003. Proceedings of*, vol. 3, 2003.

[6] A. Goetzberger, G. Kleiss, T. Nordmann, A. Froelich, G. Hille, C. Reise, E. Wiemken, V. van Dijk, and J. Betcke, "The Potential of PV-noise barrier technology in Europe," *16th European Photovoltaic Energy Conference and Exhibition*, 2000.

[7] T. Nordmann and A. Goetzberger, "Motorway sound barriers: recent results and new concepts for advancement of technology," *IEEE - Photovoltaic Energy Conversion*, vol. 1, 1994.

[8] J. Knight, E. Rudkin, and H. Gilbert, "Photovoltaic building integration concepts," *Proceedings of the IEA PVPS Task VII Workshop*, 2000.

[9] C. Bern, "Monitoring PV Noise barrier in Münsingen," 2013.

[10] T. Nordmann, T. Vontobel, and L. Clavadetscher, "15 years of experience in construction and operation of two bifacial photovoltaic systems on Swiss roads and railways Land in Germany," 2012.

[11] M. D. Jong, M. van den Donker, and W. Folkerts, "Self-shading in bifacial photovoltaic noise barriers," *Solar Energy*, 2016.

[12] R. Guerrero-Lemus, R. Vega, T. Kim, A. Kimm, and L. E. Shephard, "Bifacial solar photovoltaics - A technology review," *Renewable and Sustainable Energy Reviews*, vol. 60, 2016.

[13] J. Johnson, D. Yoon, and Y. Baghzouz, "Modeling and analysis of a bifacial grid-connected photovoltaic system," in *IEEE Power and Energy Society General Meeting*, 2012.

[14] L. Kreinin, N. Bordin, A. Karsenty, A. Drori, D. Grobgeld, and N. Eisenberg, "PV Module Power Gain Due to Bifacial Design, Preliminary Experimental and Simulation Data.," 2010.

[15] U. Alper, T. Hun, T. Markus, A. Halm, J. Koduvelikulathu, C. Comparotto, R. Kopecek, and H. Kurz, "Simulation of energy production by bifacial modules with revision of ground reflection," *Energy Procedia*, vol. 55, 2014.

[16] V. Aken and B. B, "Relating indoor and outdoor performance of bifacial modules," in *2014 IEEE 40th Photovoltaic Specialist Conference, PVSC 2014*, 2014.

[17] C. Hansen, "Irradiance Modeling for Bifacial PV modules," 2016.

[18] I. Shoukry, J. Libal, R. Kopecek, E. Wefringhaus, and J. Werner, "Modelling of Bifacial Gain for Stand-alone and in-field Installed Bifacial PV Modules," *Energy Procedia*, vol. 92, pp. 600–608, 2016.

[19] C. K. Lo, Y. S. Lim, and F. A. Rahman, "New integrated simulation tool for the optimum design of bifacial solar panel with reflectors on a specificsite," *Renewable Energy*, vol. 81, 2015.

[20] C. Deline, S. Macalpine, B. Marion, and J. S. Stein, "Evaluation and Field Assessment of Bifacial Photovoltaic Module Power Rating Methodologies," *IEEE Photovoltaic Specialists Conference*, 2016.

[21] C. Reise and A. Schmid, "Realistic Yield Expectations for Bifacial PV Systems," 2015.

[22] A. H. Smets, K. Jäger, O. Isabella, R. A. van Swaaij, and M. Zeman, *Solar Energy*. Cambridge: UIT Cambridge Ltd, 2016.

[23] U. A. Yusufoglu, T. M. Pletzer, and L. J. Koduvelikulathu, "Analysis of the Annual Performance of Bifacial Modules and Optimization Methods," vol. 5, 2015.

[24] H. Nussbaumer, F. Baumgartner, T. Baumann, and D. Schar, "New Opportunities for a better power distribution by the use of bifacial modules in future PV systems," *IEEE Journal of Photovoltaics*, 2014.

[25] J. P. Singh, A. G. Aberle, and T. M. Walsh, "Electrical characterization method for bifacial photovoltaic modules," *Solar Energy Materials and Solar Cells*, vol. 127, 2014.

[26] K. Ishaque, Z. Salam, and H. Taheri, "Simple, fast and accurate two-diode model for photovoltaic modules," *Solar Energy Materials and Solar Cells*, vol. 95, 2011.

[27] D. Clugston and P. Basore, "PC1D version 5: 32-bit solar cell modeling on personal computers," in *IEEE Photovoltaic Specialists Conference*, 1997.

[28] C. Duran, H. Deuser, R. Harney, and T. Buck, "Approaches to an improved IV and QE characterization of bifacial silicon solar cells and the prediction of their module performance," in *Energy Procedia*, 2011.

[29] A. Edler, "Development of bifacial n-type solar cells for industrial application," 2014.

[30] S. W. Glunz and A. Cuevas, "Bifacial Silicon Solar Cells – An Overview," *Solar Energy*, 2012.

[31] V. d'Alessandro, F. Di Napoli, P. Guerriero, and S. Daliento, "An automated high-granularity tool for a fast evaluation of the yield of PV plants accounting for shading effects," *Renewable Energy*, 2015.

[32] C. Rojas, S. Kouro, and D. Cardemil, "Modelling Monofacial and Bifacial Solar Modules," 2015.

[33] S. Suckow, T. M. Pletzer, and H. Kurz, "Fast and reliable calculation of the two-diode model without simplification," *IEEE Journal of Photovoltaics*, vol. 15, 2007.

[34] C. Duran, "Bifacial Solar Cells : High Efficiency Design, Characterization, Modules and Applications," 2012.

[35] Rijkswaterstraat, "Modulaire Geluidsschermen (Modular Glass Screen Noise Barrier)," 2006.

[36] Federal Highway Administration, *Noise Barrier Design Handbook*. 2011.

[37] D. May, "The optimum weight of highway noise barriers," *Journal of Sound and Vibration*, vol. 68(1).

[38] H. Bendtsen, "Noise Barrier Design: Danish and Some European Examples," 2010.

[39] G. J. M. Janssen, B. B. V. Aken, A. J. Carr, and A. A. Mewe, "Outdoor performance of bifacial modules by measurements and modelling," *Energy Procedia*, vol. 77, 2015.

[40] U. Yusufoglu, T. Lee, T. Pletzer, and H. Kurz, "Modeling and simulation of annual energy yields of bifacial modules at different climate zones," 2014.

[41] S. N. Laboratories, "PV Performance modeling collaborative.".

[42] Y. A. Cengel, *Heat and Mass Transfer: A Practical Approach*. 2006.

[43] J. Remund, S. Müller, and S. Kunz, "Meteonorm Handbook Part I : Software," 2015.

[44] R. A. Muneer. and T., "Sun position for daylight models: Precise algorithms for determination.," *Lighting Research and Technology 25*.

[45] W. De Soto, S. A. Klein, and W. A. Beckman, "Improvement and validation of a model for photovoltaic array performance," *Solar Energy*, vol. 80, 2006.

[46] C. A. Gueymard, "From Global Horizontal To Global Tilted Irradiance: How Accurate Are Solar Energy Engineering Predictions in Practice?," 2008.

[47] R. Perez, R. Seals, and A. Zelenka, "Climatic Evaluation of Models that Prdict Hourly Direct Irradiance From Hourly Global Irradiance," 1990.

[48] PVSyst, "Albedo Values," tech. rep., http://files.pvsyst.com/help/albedo.htm, Date Accessed : 2016-11-01.

[49] S. Duluk and H. Nelson, "Comparison of solar evaluation tools: from learning to practice,"

[50] K. Sinapsis, C. Tzikas, G. Litjens, M. v. d. Donker, W. Folkerts, W. v. Sark, and A. Smets, "Yield Modelling For Micro Inverter, Power Optimizer And String Inverter Under Clear and Partially Shaded Conditions," *IEEE*, 2015.

[51] V. Quaschning and R. Hanitsch, "Shade Calculations in Photovoltaic Systems," *ISES Solar World Conference*, pp. 1–5, 1995.

[52] Sketchup, "Point Gadget."

[53] M. L. Boas, *Mathematical Methods in The Physical Sciences*. John Wiley & Sons, Inc., third edit ed., 2006.

[54] R. L. Graham, "An efficient algorith for determining the convex hull of a finite planar set," 1972.

[55] J. R. Shewchuk, "Applied Computational Geometry Towards Geometric Engineering," *Triangle: Engineering a 2D Quality Mesh Generator and Delaunay Triangulator*, 1996.

[56] R. Santbergen, V. A. Muthukumar, R. Valckenborg, W. V. D. Wall, A. Smets, and M. Zeman, "Calculation of irradiance distribution on PV modules by combining sky and sensitivity maps," *Solar Energy 150*, 2017.

[57] R. M. J. Perez, R; Seals, "Modeling Skylight Angular Luminance Distribution from Routine Irradiance Measurements," 1993.

[58] M. K. Fuentes, "A Simplified Thermal Model for Flat-Plate Photovoltaic Arrays," *Sandia Report*, 1987.

[59] G. Notton, C. Cristofari, M. Mattei, and P. Poggi, "Modelling of a double-glass photovoltaic module using finite differences," vol. 25, 2005.

[60] J. Bronkhorst, "Optical and electrical simulations of undulated PV modules," 2016.

[61] M. Villalva, J. Gazoli, and E. Filho, "Comprehensive Approach to Modeling and Simulation of Photovoltaic Arrays," *IEEE Transactions on Power Electronics*, vol. 24, 2009.

[62] F. Adamo, F. Attivissimo, A. Di Nisio, and M. Spadavecchia, "Characterization and testing of a tool for photovoltaic panel modeling," *IEEE Transactions on Instrumentation and Measurement*, vol. 60, 2011.

[63] K. Sinapis, G. Litjens, M. v. d. Donker, and W. Folkerts, "Outdoor Characterization of three pv architectures under clear and shaded conditions," *Eupvsec*, 2014.

[64] NSP, "Datasheet of NSP_ 1405 BiFi NS6MB," 2015.

[65] E. Instruments, "Instruction Manual EKO Pyranometer MS-802," tech. rep., EKO, 2015.

[66] E. Instruments, "Instruction Manual EKO IV-Tracer MP-160," 2015.

[67] D. T. Reindl, W. A. Beckman, and J. A. Duffle, "Diffuse fraction correlations," 1990.

[68] M. A. Martínez, J. M. Andújar, and J. M. Enrique, "A new and inexpensive pyranometer for the visible spectral range," *Sensors (Switzerland)*, vol. 9, 2009.

[69] A. Woyte, M. Richter, D. Moser, M. Green, S. Mau, and H. G. Beyer, *Analytical Monitoring of Grid-connected Photovoltaic Systems*, vol. 13. 2014.

[70] L. Slooff, M. D. Jong, C. Tzikas, M. Debije, S. Verkuilen, T. Reijnaerts, M. Kanellis, and W. Folkerts, "SONOB Final Report," 2017.

[71] R. Caroprese, "Use of LIDAR Data in Photovoltaic Energy Yield Estimation,"